

Fluidic and Polymeric Integration and Functionalization of Optical Microresonators

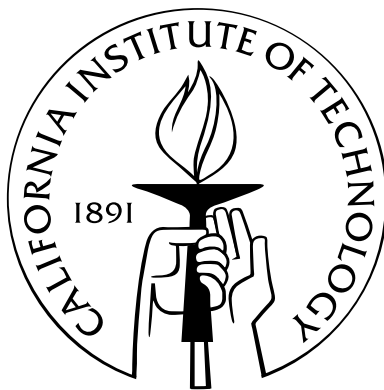
Thesis by

Brett Maune

In Partial Fulfillment of the Requirements

for the Degree of

Doctor of Philosophy



California Institute of Technology

Pasadena, California

2005

(Defended November 17, 2005)

© 2005

Brett Maune

All Rights Reserved

To my parents,
Michael and Joette.

Acknowledgements

I would like to thank Professor Axel Scherer for providing an environment within which I could pursue my varied intellectual interests while simultaneously guiding and supporting me during the Ph.D. adventure. I have really enjoyed my time at Caltech. Caltech is truly a unique and remarkable place.

I would also like to thank Jeremy Witzens. Not only did he assist me with many aspects of my research over the years, but he has also been a good friend. I enjoyed our countless scientific discussions as well as our equally countless non-scientific ones.

I would like to thank Thomas Baehr-Jones for sharing his simulation software which was crucial for my research.

I would like to thank Michael Kolodrubetz for taking much of the photoaddressable polymer characterization data during a SURF project.

Throughout the years I was fortunate to participate in numerous collaborations with other research groups. I would like to thank Professor Psaltis, Professor Atwater, and the members of their groups who assisted me by sharing their equipment, knowledge, and experience.

I would also like to thank my numerous rock climbing, mountaineering, and adventure comrades for the many exciting (perhaps sometimes crazy) trips taken to escape the windowless labs. These memories will last a lifetime.

Last but not least, I would like to thank my parents, Michael and Joette Maune, for creating a nurturing and supportive environment that enabled me to freely pursue my intellectual and other interests. The person I am today is a direct result of the strong foundation they provided throughout my childhood and beyond.

Abstract

Optical resonators are structures that spatially confine and temporally store light. The use of such resonators continues to permeate throughout society as improvements in their design and fabrication qualify them to fulfill an ever-increasing array of technological and scientific applications. Traditionally, resonators have primarily been used in lasers and as filters, and more recently have been utilized in other areas including chemical sensing, spontaneous emission modulation, and quantum electrodynamics experiments. In many of these applications, the functionalities of the resonators are solely derived from the geometry and material composition of the resonators themselves. The central theme of this thesis is the investigation of further increasing a resonator's functionality through its integration with fluidic and polymeric materials.

The thesis begins with an investigation of integrating silicon ring resonators with electro-optic polymer and liquid crystal in an effort to tune the resonators' resonant wavelengths. Although the electro-optic polymer efforts are a failure, we are able to electrically tune the rings' resonances using electrodes and the reorientation of liquid crystal surrounding the resonators. We then take the knowledge and experience acquired from these experiments and pursue the functionalization of photonic crystal laser resonators, a relatively new class of microresonators constructed from a thin slab of InGaAsP quantum well material with a periodic array of holes etched through the slab. To this end, we first infiltrate the porous resonators with liquid crystal and construct liquid crystal cells around the devices. We are then able to tune the lasing wavelengths by reorienting the liquid crystal with a voltage applied across the cell. Next, we devise a new photonic crystal cavity designed to optimally interact with infiltrated birefringent materials, by supporting two orthogonally polarized high-Q

modes. Again, we infiltrate the cavity with liquid crystal, but this time optically control the liquid crystal orientation with a photoaddressable polymer film. By doing so we are able to realize a fundamentally new laser tuning method by reversibly Q-switching a resonator's lasing mode between the two cavity modes and thereby control the laser's emission wavelength and polarization. The successful fluidic and polymeric integration with optical resonators presented in this thesis demonstrates some of the possible synergies that can be obtained with such integration and suggests that further enhancements in resonator functionality is possible.

Contents

Acknowledgements	iv
Abstract	v
Glossary of Acronyms	xxxvii
1 Introduction	1
2 Tuning Ring Resonators	5
2.1 Electro-Optic Polymer	6
2.1.1 Applications	6
2.2 Liquid Crystal	7
2.2.1 Physical and Optical Properties	9
2.2.2 Liquid Crystal Alignment Methods/Freedericksz Transition . .	11
2.2.3 Applications	13
2.3 Polarization Interference Microscopy	14
2.4 Ring Resonators	18
2.4.1 Tuning Methodology	18
2.4.2 Device Geometry and Sample Fabrication	19
2.5 Ring Integration with EO Polymer	20
2.5.1 Electro-Optic Polymer Deposition and Poling	22
2.6 Ring Integration with LC	22
2.7 Experimental Characterization and Tuning Results	23
2.7.1 Polarization Interference Microscopy Analysis of LC Alignment	29
2.8 Discussion and Conclusions	30

3	Tuning Photonic Crystal Lasers	32
3.1	Photonic Crystals	32
3.2	Photonic Crystal Resonators	34
3.2.1	Motivation for LC Integration/Previous Tuning Efforts	36
3.2.2	Tuning Methodology	37
3.3	Photonic Crystal Cavity Design	37
3.3.1	Photonic Crystal and Cavity Parameters	39
3.3.2	Wafer Specifications and Sample Fabrication	42
3.4	Integration of PCs with LC	46
3.4.1	Liquid Crystal Parameters	46
3.4.2	Liquid Crystal Cell Fabrication	47
3.4.3	Liquid Crystal Domain Formation	47
3.4.4	Confined Geometry Effects	48
3.5	Electrical Tuning of LC Infiltrated PC Lasers	51
3.5.1	Experimental Setup and Procedures	51
3.5.2	Liquid Crystal Characterization	55
3.5.3	Polarization Interference Microscopy Analysis of LC	56
3.5.4	Electrical Tuning Results	59
3.5.5	Effect of LC Domain Orientation on PC Tuning Range	62
3.5.6	Effect of Surface Anchoring on PC Tuning Behavior	63
3.6	Discussion and Conclusion	66
4	Optically Triggered Q-Switched Photonic Crystal Lasers	68
4.1	Photoaddressable Polymer	69
4.1.1	Experimental Characterization	71
4.1.2	Applications	78
4.2	Motivation for Q-Switching	79
4.2.1	Q-Switching Methodology	79
4.3	Photonic Crystal Cavity Design	82
4.3.1	Photonic Crystal and Cavity Parameters	84
4.3.2	Cavity Q Tunability	87

4.3.3	Fourier Space Analysis of Cavities	88
4.3.4	Laser Fabrication and Wafer Specification	91
4.4	Integration of PCs with PAP and LC	91
4.4.1	Photoaddressable Polymer Film Fabrication	92
4.4.2	Liquid Crystal Parameter Considerations	94
4.4.3	Liquid Crystal Cell Fabrication	95
4.5	Q-Switching of the PC Laser	95
4.5.1	Experimental Setup and Laser Characterization	96
4.5.2	Photoaddressable Polymer Writing Procedure	98
4.5.3	Verification of PAP Aligning LC	100
4.5.4	Q-Switching Results	103
4.5.5	Q-Switching Regimes	107
4.6	Electrical Implementation of Q-Switching	112
4.7	Discussion and Conclusion	116

Bibliography	119
---------------------	------------

List of Figures

- 2.1 Schematic of EO polymer poling process. (a) Initially the polymer is randomly oriented. To produce a nonzero, second order nonlinear optical response, the material's centrosymmetry must be broken. To realize this, the polymer is heated in the presence of a strong electric field (b). The electric field aligns the polymer. (c) The alignment is stable when the sample is cooled. 6
- 2.2 Schematic of an EO polymer-based Mach-Zehnder modulator. (a) First, the EO polymer (red) in each interferometer arm is poled in opposite directions. (b) After poling, a modulation voltage applied across each arm causes the refractive index to change in opposite directions. (c) Light traveling in one arm experiences a negative phase shift, whereas light in the other arm experiences a positive phase shift as compared to the unbiased interferometer. Interference occurs when the light is recombined at the output port. The amount of transmitted light can be modulated by adjusting the accumulated phase difference between the arms with an applied voltage. 7
- 2.3 Schematic illustration of lyotropic LCs and phases. (a) Amphiphilic molecules (polar head with hydrocarbon tail) dissolved in water are an example of lyotropic LCs. (b) At certain concentrations the molecules self-organize into spherical micelles, which form to shield the hydrocarbon tails from the polar aqueous environment. Another stable configuration of amphiphilic molecules is the bilayer structure shown in (c). These structures are routinely found in biology, of which a cell wall is an example. 9

- 2.4 Schematic of three common LC phases. (a) Nematic phase exhibits orientational order but no positional order. (b) Smectic phase possesses additional positional order with the LC segregated into two-dimensional planes. (c) Cholesteric phases exist with numerous variations, but a defining characteristic is the LC organizes into spirals. 9
- 2.5 Physical structure of LC molecules. The molecules are ellipsoidal in shape with their so-called director defined as being parallel to the molecules' long axis. Light polarized parallel and orthogonal to the director experience a refractive index n_e and n_o , respectively. Light polarized at an angle θ to the director experiences a refractive index given by equation 2.1. 10
- 2.6 Illustration of homogeneous and homeotropic LC alignment. (a) Homogeneous (planar) LC alignment can be induced by rubbing grooves into a surface. (b) Homeotropic alignment can be induced by coating a surface with surfactant molecules. If the density of surfactant molecules is sufficiently low, then the LC molecules can fill the gaps in between them and cause the LC molecules to orient parallel to the surfactant molecules. 12
- 2.7 Illustration of Fredericksz transition in LC. (a) Initially the LC features homogeneous alignment. (b) When a voltage is applied across the LC cell that exceeds the threshold voltage, the LC undergoes a Fredericksz transition and aligns parallel to the field. Note the LC near the surfaces are anchored, which inhibits the realignment. 13

- 2.8 Illustration of a twisted nematic LC spatial light modulator. The two plates at the ends of the LC cell are rubbed in orthogonal directions. In the absence of an applied voltage (a), the rubbed plates induce a spiral orientation in the LC. Vertically polarized light enters the cell, and the polarization rotates along with the rotation of the LC. Horizontally polarized light exits the cell and passes through a horizontally oriented polarizer. (b) When a voltage is applied across the cell and triggers a Fredericksz transition, the polarization of the light traversing the cell no longer rotates. Now the light is blocked by the second polarizer. In effect, transmission of light through the cell can be modulated with an applied voltage. 14
- 2.9 Schematic of PIM technique. Polarized light impinges upon a birefringent material. While traversing the sample, the ordinary and extraordinary components experience different refractive indices and a phase difference is accumulated between the two waves. The two waves are combined and interfere at a second polarizer which is oriented orthogonal to the initial polarization axis. The resulting interference pattern provides information regarding the sample's birefringence, thickness, and orientation. Note our PIM configuration differs from the one shown. In our setup the light originates from above the sample, is reflected from the bottom of the sample, traverses the sample again, and finally exits at the top. 16
- 2.10 Michel-Levy chart showing the possible colors observed when using white-light illumination for PIM. The resulting color is not only a function of the sample's birefringence and thickness but is also dependent on the sample's orientation (orientational-dependent effective birefringence). For our purposes, we generally know the LC's birefringence and thickness that is being investigated, and so PIM primarily provides information regarding the LC's orientation. Consequently, PIM is useful in evaluating the effectiveness of the various LC alignment methods discussed in this thesis. 16

- 2.11 A beautiful PIM image showing point defects in nematic LC films [38]. The point defects are clearly identified by the “Maltese crosses.” The alignment of the LC around the defects and throughout the film can be inferred by the structure of the dark regions and by observing the movement of the black regions while rotating the sample under the polarizers. For a planar LC orientation, the dark regions are where the LC is aligned parallel to one of the two polarizers used in the PIM setup. 17
- 2.12 An illustration of a series of ring resonators serving as telecommunication filters. Each resonator is designed to be resonant with only one wavelength and drops that wavelength into a second waveguide. By concatenating a series of resonators with slightly different radii, many wavelengths can be simultaneously multiplexed on a chip. 19
- 2.13 Images showing ring geometry. (a) Optical microscopy image of representative ring resonator. The ring radius is 5 μm , waveguide widths are 500 nm, and waveguide-ring gap is 100 nm. The silicon rectangles surrounding the resonator exist for planarization purposes during chemical-mechanical polishing. (b) A scanning electron microscope (SEM) image taken after the oxide etch showing the exposed ring sidewalls. 20
- 2.14 An SEM image showing the uneven electrode surface caused by the silicon rectangles protruding from the surrounding oxide. Evaporating thick electrodes were required to guarantee they were contiguous, given the uneven surface on which the electrodes were deposited. 21
- 2.15 Optical microscopy images showing silicon breakdown during EO polymer poling. (a) In-plane electrodes were aligned to the resonator and evaporated. Electro-optic polymer was then spun on top of the rings and electrodes and was then ready to be poled. (b) The poling process requires strong electric fields ($\sim 100 \text{ V}/\mu\text{m}$) that exceed silicon’s breakdown potential ($\sim 30 \text{ V}/\mu\text{m}$). Consequently, the silicon in between the electrodes broke down during poling and completely destroyed the resonator. 23

2.16	Optical microscopy image of electrodes and the corresponding electrostatic simulation of their generated electric field pattern. (a) Optical image of first electrode design used for LC tuning of ring resonator experiments. The rings could not be tuned with LC using this electrode geometry. One possible explanation can be found in the electrostatic simulations (b). The electrostatic simulation is a plot of the angular difference of the field direction and the ring's radial axis. Blue corresponds to purely radial field (0°) and red is purely azimuthal (90°). The simulations reveal that the azimuthal (red) and radial (blue) field components are roughly balanced when integrated around the entire ring. For this unusual case, no tuning is expected due to LC aligning to the field, and so new electrode geometries were designed and used. The resonator shown in (a) is a double ring resonator, but the rings actually tested are the single rings with geometries mentioned earlier in the chapter. . . .	25
2.17	An SEM image of azimuthally-biased electrode configuration and the associated electrostatic field simulation. (a) Scanning electron micrograph of fabricated electrodes designed to maximize the azimuthal field component while minimizing the radial component. (b) Electrostatic simulations showing the electric field pattern produced by the electrode configuration. The angular difference of the field direction and the ring's radial axis is plotted. Blue corresponds to a purely radial field (0°) and red is purely azimuthal (90°).	25
2.18	An SEM image of radially-biased electrode configuration and the associated electrostatic field simulation. (a) Scanning electron micrograph of fabricated electrodes designed to maximize the radial field component while minimizing the azimuthal component. (b) Electrostatic simulations showing the electric field pattern produced by the electrode configuration. The angular difference of the field direction and the ring's radial axis is plotted. Blue corresponds to purely radial field (0°) and red is purely azimuthal (90°).	26

- 2.19 Experimental realization of LC-mediated ring resonator tuning. (a) Plot of collected transmitted power as a function of wavelength showing three resonances. (inset) Close-up of resonance B taken with 0 V, 10 V, and 20 V applied across the electrodes. (b) Resonance tuning as a function of voltage applied across the electrodes. All three resonances blue-shift approximately 0.20 nm at 20 V, and no threshold is observed in the tuning data, indicating the absence of a Freedericksz transition in the LC. 27
- 2.20 Plot of the resonance sensitivity to changes in the cladding refractive index. The resonance sensitivity increases with increasing cladding refractive index. This relationship is attributed to the fact that a larger fraction of the mode overlaps with the cladding as the cladding's refractive index increases. The black line corresponds to the cladding refractive index expected if the LC is randomly oriented around the ring. 28
- 2.21 Michel-Levy chart indicating the possible colors for the PIM imaging of the LC ring resonator cladding. Considering the LC layer is exceptionally thin (sub-micron), we are confined to the extreme lower left corner of the chart, denoted by a red triangle. This suggests we can only obtain gray scale variations in the PIM images due to LC realignment. 29
- 2.22 Polarization interference microscopy images of a ring with LC cladding. The images were taken with (a) 0 V and (b) 20 V applied across the electrodes. Although the precise LC orientation cannot be determined using the PIM images, it is clear the orientation lacks the symmetry of the simulated electric field. It appears the LC may be anchored to the ring surface and/or to defects around the ring. This can seriously impair the LC alignment and may explain the discrepancy between the expected and realized tuning of the resonators. 30

- 2.23 Demonstration of a ring resonator acting as a chemical sensor. Three scans, measuring the transmitted power past a resonator with an unpoled EO polymer cladding, were recorded over a period of approximately 20 minutes. Over the course of the scans the resonance was observed to blue-shift approximately 2 nm. The shift is attributed to a cladding refractive index change of $\sim 10^{-2}$ due to photochemical degradation of the polymer cladding. The detection of refractive index and absorption changes through the observation of resonance shifts can serve as the basis for using rings in chemical sensing applications. 31
- 3.1 Schematic of cladding light cones. Light possessing k-vectors which lie above the cladding's (refractive index n_1) light cone can radiate into the cladding and are not well confined in the PC slab. Light below the light cone remains guided by the high index PC slab and undergoes total internal reflection upon striking the slab/cladding interface. Minimizing the Fourier components comprising a cavity mode that lie above the light cone is a technique for maximizing a mode's Q [64, 74, 75]. Increasing the cladding refractive index from n_1 to n_2 , however, increases the portion of k-space which lies above the light cone. A mode's Fourier components that lie between the two light cones are *now* no longer well confined and contribute to additional losses, lowering the mode's Q. 38
- 3.2 Representative two-dimensional band diagrams showing first TE-like bandgaps for triangular (a) and square (b) lattices. The photonic crystal refractive index is 3.4 and hole radii are 0.33 (r/a). 40
- 3.3 Scanning electron micrograph of fabricated PC laser cavity. The PC lattice periodicity, a , is 500 nm; the normalized hole radii are 0.33 (r/a); the normalized defect hole radius is 0.2 (r/a); and the half-ellipses have a normalized minor axis length of ~ 0.13 (r/a). (inset) Close-up of defect cavity. 41

- 3.4 Simulated modal field profiles. Z (out-of-plane) component of magnetic field for high-Q Y dipole mode (a) and low-Q X dipole mode (b). (c) Electric field amplitude of Y dipole mode. (d) Cross-section view of electric field amplitude for Y dipole mode showing the evanescent fields extending into the cladding layers. The evanescent fields are important for tuning the cavity resonances because they enable tuning by changing the refractive index in the cladding regions. 41
- 3.5 Finite-difference time-domain simulation of Y dipole mode Q as a function of ambient refractive index. Although the Q is above 25,000 at an ambient refractive index of 1.0, the Q plummets to approximately 2,000 at an ambient refractive index of 1.5. The simulations in conjunction with previously published PC laser work [66] suggest lasing is possible with this cavity design after LC infiltration. 42
- 3.6 Simulation of dielectric band, air band, and Y dipole resonance as a function of the ambient refractive index. As the ambient refractive index increases, the bandgap narrows and the resonance red-shifts. For the lasers we use ($a = 500$ nm), the tuning rate of the resonance is approximately 210 nm per unit of ambient refractive index change. . . 43
- 3.7 Scanning electron micrographs showing wafer composition. (a) This cross-section image is taken after e-beam lithography processing, but before any etching steps. The various layers (including the 4 quantum wells) comprising the wafer can be discerned in the image. (b) This image is of a fully processed sample and shows the removal of the $1 \mu\text{m}$ InP layer (for optical isolation purposes) and the suspended thin InGaAs etch stop layer (the layer was penetrated during the HI dry etch step under the PC etch guides and enabled the undercutting of the layer during the HCl wet etch step (see figure 3.8)). 44

3.8	<p>Schematic of fabrication procedure for InGaAsP quantum well PC lasers. (a) The original wafer before any processing. (b) First, a 130 nm SiO₂ hard mask is deposited on the wafer using PECVD. (c) Next, PMMA is spun on the sample in preparation for the subsequent e-beam lithography steps. (d) The PMMA is exposed with the PC pattern and is completely transferred into the PMMA after developing the exposed resist. (e) Next, the pattern is transferred into the SiO₂ hard mask via a CHF₃ RIE etch. (f) The pattern is then transferred into the quantum well slab with a HI-based ICPRIE etch. Lastly, the slab is undercut by dissolving the InP sacrificial layer beneath the slab with a HCl wet etch.</p>	45
3.9	<p>Cross-section of LC cell constructed around PC lasers. The LC comprising the top cladding layer is estimated to be approximately 15 μm.</p>	47
3.10	<p>Schematic showing origin of domain wall formation. (a) With no voltage applied across a standard LC cell, the LC is aligned parallel to the plates. (b) When a voltage is applied across the cell that is above the threshold voltage, the LC reorients and aligns in the direction of the field. For voltages below saturation the LC is not perfectly aligned to the field and multiple orientation possibilities exist for the LC that are energetically equivalent. The interface between these different orientations forms a domain wall which separates the two regions. These domain walls can be seen using PIM and appear as bright lines in the images.</p>	48
3.11	<p>Polarization interference microscopy image of LC domains. The bright lines are the domain walls formed by LC aligning differently in response to an applied electric field as in figure 3.10</p>	49
3.12	<p>Schematic of three LC configurations commonly found in small cylindrical holes. Top and cross-section views are provided for (a) escaped radial with point defect, (b) planar-polar, and (c) parallel axial configurations.</p>	50

3.13	Schematic of μ PL setup used to characterize PC lasers. Light from an 830 nm laser diode was focused onto the PC sample with a 100x objective lens. Emitted (or reflected pump) laser light was collected by the same objective lens and was either sent to an OSA to record the spectra, into a CCD for imaging, or into an IR camera to view the modal profiles. A removable polarizer could be inserted in front of the OSA to measure the polarization of the light emitted by the PC laser. A computer running LabView was used to store the spectra recorded by the OSA and was integrated with a Super Nintendo TM controller which was used to trigger the spectra acquisitions. A picture of a slightly modified version of the setup can be seen in the next chapter in figure 4.18.	52
3.14	Emission spectrum from unprocessed InGaAsP material. The emission is a maximum at 1550 nm, the desired engineered maximum.	54
3.15	Experimental demonstration of PC laser tuning with liquid infiltration. Lasing wavelengths are recorded for several samples after infiltrating with index-matched fluids. The resonant wavelengths red-shift approximately 80 nm after being infiltrated with a 1.45 refractive index liquid. This shift is in good agreement with simulations which predict a shift of about 90 nm and is also roughly the resonance shift expected due to infiltrating the cavities with the LC.	54
3.16	L-L curve of laser infiltrated with LC. The lasers were pumped with 30 ns pulses and 3 μ s periodicity. The laser peak threshold power is estimated to be approximately 5 mW. The relatively high threshold is primarily attributed to the increased losses associated with the LC infiltration.	55
3.17	Michel-Levy chart showing the color region accessible given the LC's birefringence (~ 0.05) and thickness ($\sim 15.0 \mu\text{m}$), keeping in mind the PIM images are created by light traversing the LC cell twice.	56

- 3.18 Polarization interference microscopy images showing LC planar orientation and domain-like features. (a) By referring to the Michel-Levy chart in figure 3.17 we see the bulk LC is predominantly homogeneously aligned. The gradient in color is attributed to a gradient in cell thickness caused by the ITO top electrode plate not being parallel to the PC substrate. The cells are normally fabricated with the top plate parallel to the PC substrate. Scale bar is $500 \mu\text{m}$. (b) A close-up of part (a) denoted by the white box. In this image the domain-like structures are more clearly seen and the hexagonal PC samples can be seen as well. The LC forms well-aligned regions that are rotated with respect to each other, causing variations in the brightness of the image but not in color (the variations in color are due to variations in the degree of in-plane alignment). Scale bar is $250 \mu\text{m}$ 57
- 3.19 Sequence of PIM images showing LC undergoing Fredericksz transition. The voltage applied across the cell is slowly ramped from 0 V (a), through the threshold voltage (b) and (c), and up to 20 V (d). The threshold voltage is determined using this method and is approximately 4 V. As the voltage is increased toward saturation, the LC continues to align parallel to the electric field and causes the PIM image to become black. 58
- 3.20 Sequence of PIM images showing LC domain consolidation. All images are taken at voltages above the Fredericksz transition. Consolidation of domains is indicated by disappearing domain walls (bright lines). The red boxes in (a) highlight domain walls which are in the process of disappearing in the sequence of images (a)-(d). 59

3.21 Sequence of PIM images showing LC surface alignment memory. (a) This image shows the initial LC orientation with no voltage applied across the cell. (b) This image is taken as the voltage is ramped through the Fredericksz transition. (c)-(d) These images are taken when the LC is aligned vertically with 20 V applied across the cell. A domain wall can be seen moving across the PC samples. (e) This image is taken as the voltage is ramped down through the Fredericksz transition. (f) This image is taken with no voltage applied across the cell. The beginning and ending LC orientations appear to be identical. The LC at the surfaces is believed to be anchored and dictates the orientation of the bulk LC in the cell. 60

3.22 Finite element simulation of electric field around PC slab generated by the ITO electrodes. Electric field magnitudes are represented by a normalized color scale from 0 to 1, and arrow direction and length denote field direction and amplitude, respectively. (a) Cross-section of the PC membrane slab. The electric field is screened from the PC holes due to the doped semiconductor slab. (b) Close-up of field in central defect hole denoted by red box in part (a). The simulation suggests the electric field does not penetrate appreciably into the defect hole. The screening of the electric field may significantly impair the ability to tune the lasers by prohibiting the controlled alignment of the LC within the PC holes. 61

- 3.23 Demonstration of laser tuning via LC realignment. a) Laser spectra taken with an applied voltage ranging from 0-20 V across the LC cell. The threshold for tuning is approximately 4 V, coinciding with the measured LC threshold voltage using PIM (see figure 3.19). A maximum blue-shift of 1.2 nm is measured at 20 V. For clarity note lasing wavelength monotonically decreases with increasing voltage, with the 0 V trace being the far right and the 20 V trace being the far left. b) Lasing wavelength versus applied voltage for a voltage ramp cycle. Although the tuning rate lessens at higher voltage, the data suggest saturation is not even reached at 20 V and further tuning may be possible with stronger fields. The tuning is reversible but demonstrates a slight hysteresis at low fields which may be due to charging or impurity effects. The marker box height represents the upper bound of the uncertainty in the lasing wavelength obtained from the spectra. 62
- 3.24 Illustration of PC laser tuning dependence on LC domain orientation. (a) Close-up of Y dipole mode showing polarization structure with superimposed hypothetical LC molecule. b) Interference pattern captured using PIM showing the LC spontaneously forming domains above PC lasers (hexagons). The laser tuning ranges are partly dependent upon the zero-field LC orientation in the top cladding. Maximum tuning occurs when the LC is initially oriented such that its director is parallel to the mode's dominant polarization direction (shown in (a)). In this scenario the mode's top cladding refractive index modulation is essentially the maximum possible and ranges from n_e to n_o . As the LC zero-field orientation differs from the ideal case, the achievable tuning decreases and is a minimum when the LC's director is aligned orthogonal to the polarization axis. 63

- 3.25 Presumed LC orientation at three different field regimes. a) Below threshold, the LC is oriented homogeneously. b) Immediately above threshold the bulk LC aligns parallel to the field, but the LC near the PC surface remains anchored to the surface. c) As the voltage is increased, LC progressively closer to the PC membrane find it energetically favorable to reorient and align parallel to the field. Note LC in holes is drawn with a random orientation for convenience. The actual orientation within the holes is not known, but numerous possibilities exist and are discussed in the previous chapter. 65
- 4.1 Schematic of a typical PAP chemical structure. The longer molecule (a) is the mesogenic side group, whereas the shorter molecule (b) is the azo-chromophore. The chemical composition of the monomers can vary, but the monomers are typically present in roughly equal concentrations in the polymer. The side groups are attached via spacers to a methylmethacrylate backbone. The azo-chromophores absorb light and undergo *trans-cis-trans* isomerization cycles, the primary alignment mechanism in the polymer. The mesogenic groups follow the orientation of the chromophores and help reinforce it [91]). 70
- 4.2 Schematic of PAP aligning orthogonal to the polarization axis of incident light. (a) Initially the PAP is randomly oriented. (b) Upon illumination with visible light, the chromophore side groups undergo *trans-cis-trans* isomerization cycles, during which they are free to rotate. This process continues until the chromophore side groups are oriented orthogonally with respect to the actinic light's polarization axis. At this point the transition dipole moment is zero and the chromophore groups can no longer be excited, and so their orientation is frozen. The mesogenic side groups follow the orientation of the chromophores, and eventually the entire PAP becomes aligned orthogonal to the actinic light's polarization axis. 70

- 4.3 Photoaddressable polymer optical characterization setup. (top) Picture of setup. (inset) Picture of setup with Ar laser writing PAP. (bottom) Schematic of optical setup for characterizing the optical properties of the PAP. The PAP was written either with a 488 nm Ar ion laser or a 532 nm frequency-doubled Nd:YAG laser (not shown). The birefringence was measured using probe lasers at 670 nm and 1550 nm. The probe lasers were linearly polarized at a 45° angle with respect to the linearly polarized writing lasers. The birefringence was determined by measuring the polarization rotation of the probe lasers traversing the PAP with detectors arranged to measure the ratio of horizontally and vertically polarized light emanating from the sample. 72
- 4.4 Photoaddressable polymer birefringence versus writing time. The initial written birefringence is approximately 0.37 at 670 nm but quickly decays due to photobleaching to around 0.07. The slight oscillation in the maximum birefringence for each writing step is likely due to imbalanced writing intensities between the two different writing polarizations. . . . 74

- 4.5 Schematic illustrating PAP photobleaching process. (a) Initially the PAP is oriented along the X axis. Then, visible light polarized along the X axis illuminates the polymer. (b) The polymer now rotates until it is orthogonal to the polarization axis. This means the polymer can align itself anywhere along the Y-Z plane and not just along the Y axis. (c) Next, Y polarized light illuminates the polymer, and the polymer now aligns along the X-Y plane. So instead of returning to the X axis, the polymer now possesses some out-of-plane alignment and is oriented at an angle θ with respect to the X axis. A few comments regarding the photobleaching process are in order. Although the polymer can realign anywhere within a plane when illuminated with linearly polarized light, the polymer exhibits a strong bias to maintaining a planar orientation. This bias is attributed to two causes. First, probabilistically the polymer is most likely to realign completely in-plane. This can be seen by viewing the realignment as a rotational diffusion (i.e., random walk) process, and an in-plane realignment represents the shortest “rotational path” available to the polymer. Secondly and probably more importantly, the in-plane bias is also attributed to dipolar interpolymeric interactions which help to maintain a dominant in-plane orientation. Researchers have investigated the factors influencing the photobleaching rate and have even designed new PAP with particular structural characteristics to inhibit the photobleaching and thus increase the number of useful writing cycles available with the polymer. 75
- 4.6 Comparison of PAP birefringence at 670 nm to 1550 nm. The PAP’s birefringence measured at 1550 nm (the designed optimum operating wavelength for the PC lasers) is approximately two thirds the birefringence measured at 670 nm using the optical setup and procedure described earlier in the chapter. 76

- 4.7 Residual PAP birefringence versus annealing temperature. The PAP's birefringence was completely erased for annealing temperatures above 160°C, and the PAP became randomly oriented. The subsequent written birefringences were lower after annealing, indicating that the polymer initially possessed a degree of planar alignment due to the spinning process. The residual birefringences at annealing temperatures of 180°C and higher are primarily attributed to measurement error intrinsic to the optical setup. 77
- 4.8 Schematic illustration of Q-switching methodology. By rotating a birefringent material in the top cladding layer (e.g., LC), the effective refractive index experienced by orthogonally polarized cavity modes can be controlled. This, in turn, affects the relative modal Qs and is the basis for the implementation of the Q-switching technique presented in this chapter. 80
- 4.9 Schematic of Q-switching implementations utilizing LC as the control element. (a) and (b) Electrodes are used to generate electric fields to align the LC in the top cladding layer. By adjusting the potential across the two sets of electrodes, the LC can be aligned in any arbitrary direction in the plane of the PC. (c) and (d) A polarized laser, in conjunction with a film of PAP, is used to align the LC orthogonal to the writing laser's polarization axis. By controlling the polarization, the LC can be aligned in any arbitrary direction. 81
- 4.10 Schematic of idealized cavity design and real fabricated cavity. (a) Three dimensional rendered image showing idealized cavity. (b) Scanning electron micrograph of actual fabricated PC laser cavity. The square-like cavity geometry is designed to replicate the cavity experienced by the Y polarized mode for the X polarized mode without substantially decreasing the Y mode's Q. The periodicity of holes is 450 nm. The inset shows a close-up of the cavity geometry taken with a sample tilted 15°. Scale bar, 2 μm . Inset scale bar, 500 nm. 85

4.11	Photonic crystal cavity modes. Finite-difference time-domain simulation of Z component of magnetic field for (a), X polarized and (b), Y-polarized modes. The orthogonal nature of the modes' polarizations can be seen in the magnetic field patterns but are explicitly shown in figure 4.12.	86
4.12	Photonic crystal cavity modal polarization structures. Finite-difference time-domain simulation of the (a) X polarized and (b) Y polarized cavity modes.	86
4.13	Simulation of cavity mode Qs versus ambient refractive index. Although the modal Qs are significantly different at low ambient refractive indices, they converge at higher refractive indices, and both modes maintain a Q exceeding 4000 even at an ambient refractive index of 1.5. These high Qs are critical for achieving lasing with both modes after infiltrating the cavities with LC.	88
4.14	Simulation of cavity mode Qs versus ambient refractive index. The gray box marks the ambient refractive index range achievable by infiltrating the PC with the LC. This refractive index range in conjunction with the Q simulations provide an estimate of the Q tunability of our cavities. Note, however, the Q tunability estimate using these simulations likely underestimate the real tunability of the cavities because they assume an isotropic ambient refractive index, whereas in reality the cavities have anisotropic ambient refractive indices.	89

- 4.15 Simulation of k-space modal distributions and cladding light cones. Simulations of k-space distributions for (a) and (b) old Y polarized cavity mode, (c) and (d) new Y polarized cavity mode, and (e) and (f) new X polarized cavity mode. The simulations on the left column feature an ambient refractive index of 1.0, whereas the right column has an ambient refractive index of 1.5. The red circles represent the cladding light cones. Note how a significantly larger fraction of the mode in (b) is enclosed within the light cone than in (d) and (f). This is likely the reason for the superior Qs exhibited by the new cavity design after LC infiltration. The figures are plots of the absolute value of the Fourier transformed B_z field amplitudes. The field profiles are acquired from the middle of the PC slab. 90
- 4.16 Images showing poor PAP film quality. (a) PIM image taken after spinning a heavily diluted PAP solution onto a PC sample and enclosing the sample in a LC-filled cell. The bright areas denote the PC samples and indicate the PAP did not infiltrate the PC samples. (b) Close-up of some PC samples from (a). (c) An SEM image taken of partially collapsed PC membranes from the same sample as (a) and (b). The white areas are where there was no PAP. In other words, the PAP films *avoided* the PC samples. The formation of PAP films seems to be repelled by surface inhomogeneities and edges. The membranes likely collapsed during the spinning process. (d) An optical micrograph image of a concentrated PAP solution spun onto a glass coverslip. The film appears to be inhomogeneous, featuring radially directed striations. These striations may form in response to rapid solvent evaporation during the spinning process. 93
- 4.17 Schematic of LC cell constructed around PC lasers. Thickness of LC and PAP films were approximately $5\ \mu\text{m}$, and $31 \pm 1\ \text{nm}$, respectively. Top coverslip is not shown. 95

4.18	Photonic crystal laser μ PL setup. a) Picture of setup. b) Schematic of μ PL setup redesigned for Q-switching project. Light from an 830 nm laser diode was focused onto the PC sample with a 100x objective lens. Emitted laser light was collected by the same objective lens and either was sent to an OSA to record the spectra or into a CCD for imaging. A removable polarizer could be inserted in front of the OSA to interrogate the polarization of the light emitted by the PC laser. A 532 nm PAP writing laser was aligned to be coincident with the pump beam, and a dichroic mirror enabled the PAP writing and laser pumping/spectra recording to occur simultaneously. A polarizer in front of the PAP writing laser was used to control the orientation written into the polymer. Lastly, a removable polarizer could be inserted directly above the objective lens. This polarizer was used to prevent photobleaching of the polymer by the white light required for imaging and locating the sample. This polarizer was always oriented in the same direction to initialize the PAP for all samples equally.	97
4.19	Emission spectrum from unprocessed InGaAsP material. The emission drops quickly away from the maximum at 1550 nm.	98
4.20	L-L curves acquired for the same lasing resonance after infiltrating with several index-matched fluids. The lasing threshold starts at around 1 mW before infiltration and rises to nearly 6 mW as the ambient refractive index increases to 1.5.	99
4.21	Lasing wavelengths recorded for the Y polarized mode from three samples as a function of ambient refractive index. The tuning rate for all samples is approximately 200 nm per unit of ambient refractive index change.	99
4.22	Michel-Levy chart showing the possible colors accessible given the LC's birefringence (~ 0.11) and thickness ($\sim 5.0 \mu\text{m}$), keeping in mind the PIM images were created by light traversing the LC cell twice.	101

- 4.23 Polarization interference microscopy image of LC cell in contact with a PAP film. Due to the absorption of the PAP, red light was preferentially transmitted and distorted the coloration of the PIM image. Although this limited the usefulness of the image in determining the LC orientation, at the very least the interference pattern revealed the LC was not completely homeotropically aligned. The LC orientation in the center of the PIM image appears to be dominated by a disclination defect. 101
- 4.24 Polarization interference microscopy images of PAP films demonstrating photobleaching. (a)-(d) This sequence of images was taken while illuminating a PAP film comprising one side of a LC-filled cell with dim unpolarized white light. (a) Initially the LC exhibited some degree of planar orientation but oriented out-of-plane as the PAP photobleached (b)-(d). The black images indicate the LC was primarily oriented homeotropically, in the same direction as the PAP. The white arc in (c) and line in (d) connecting the two defects at the top and bottom is believed to be the interface between two LC domains. (e)-(f) These PIM images were taken with the same conditions as in (a)-(d), except now the unpolarized white light photobleaching the PAP was transmitted through a photomask. The patterns written are (e) the Caltech emblem and (f) a “smiley” face. 102
- 4.25 Polarization interference microscopy images of PAP films written using the PL setup. These images were taken by illuminating a PAP film comprising one side of a LC-filled cell with the 532 nm green laser in the PL setup shown in figure 4.18. (a) The writing laser was focused on one spot for several seconds and moved to another spot. The diffraction rings of the laser can clearly be seen in the PIM image. (b) The writing laser was quickly translated across the PAP film in the vicinity of PC lasers. Even though the exposure time was short ($\ll 1$ second), the PAP appeared to still have been written. 103

- 4.26 Schematic representation of the LC reorientation via PAP photoinduced alignment. The PAP oriented itself orthogonally (along X axis) with respect to the writing laser polarization direction (Y axis), which in turn induced a similar alignment in the LC. 104
- 4.27 L-L curves taken for cavity supporting two high-Q cavity modes after LC infiltration. The LC orientation was optimized for each cavity mode before that mode's curve was acquired. The pump position was chosen such that the two modes had roughly equal output powers when each was optimized and pumped at the power level at which the Q-switching experiments were conducted. This explains why the two modes' curves cross even though they have different thresholds. The specifically chosen pumping position results in different perceived differential quantum efficiencies (e.g., through different pumping, coupling, and collection efficiencies) for the two modes, which leads to the different slopes and the ultimate crossing of the curves. 105
- 4.28 Confirmation of orthogonally polarized lasing modes. (a) The laser spectra was taken with PAP/LC aligned with the Y axis, and the collected light was passed through a polarizer oriented at various angles. The collected power was maximized with the polarizer oriented at 0° (X axis) and minimized at 90° (Y axis), which indicated the resonance was the X polarized dipole mode. (b) The laser spectra taken with the same conditions as in (a) but with the PAP/LC aligned with the X axis. The collected power was maximized with the polarizer oriented at 90° (Y axis) and minimized at 0° (X axis), which indicated the resonance was the Y polarized dipole mode. For clarity, figure 4.12 is reproduced as insets to (a) and (b) and shows the simulated cavity mode polarization profiles. 106

- 4.29 Experimental realization of Q-switching. The laser spectra was taken after the PAP writing laser aligned the PAP/LC at several orientations. After writing at 0° (PAP writing laser polarized along X axis which caused PAP/LC to orient along Y axis), emission was maximized for the X polarized mode and minimized for the Y polarized mode. As the PAP writing laser polarization was rotated towards 90° , the cladding refractive index for the X mode increased, raising losses until the lasing was quenched and emission terminated. Meanwhile, the Y mode experienced a decreasing refractive index, which lowered cavity losses and drove the mode above threshold and lased. 107
- 4.30 Simulation of modal field overlap. Electric field magnitude for (a) X dipole and (b) Y dipole modes. The overlap of the two modes is visualized by plotting the product of the two field magnitudes (c). The modal overlap within the quantum well material is a source of the gain competition the two modes experience. 108
- 4.31 Schematic of Q-switching regimes. This figure shows the qualitative relationship between the Q-switching regime in which a cavity operates and the Qs of the two modes supported by the cavity. The labeling of the regimes are consistent with those discussed in the text and in table 4.2. The borders between the various regimes are drawn figuratively and are not meant to be taken literally. 109

- 4.32 Illustration of possible Q-switching hysteresis. For cavities operating in regime IV (see 4.31 and table 4.2), the onset of lasing in one mode coincides with the quenching of the other mode. Such cavities may exhibit hysteresis as shown in the above plot. For instance, let the cavity be initially optimized for the X mode (i.e., LC oriented along Y axis). The lasing output is originally due to the X mode but eventually switches to the Y mode as the cavity is smoothly modified and optimized for the Y mode (dotted curves). Now, as the cavity optimization is reversed (solid lines) the output switches back to the X mode, but the transition occurs at a different degree of optimization (i.e., LC orientation) than the previous transition. This proposed hysteresis is believed to be possible because of the gain competition between the modes. The lasing mode derives extra gain due to the field enhancement and so can remain lasing at higher loss levels than is required for it to initially lase. 110
- 4.33 Schematic showing how adjusting the pumping parameters for PC lasers influence the Q-switching regime in which the cavity operates. The red line indicates the control obtained by varying the pump power. The lasers' pump power affects the gain for both modes equally, and its effect is represented by artificially changing (increasing or decreasing) the cavity Qs. The blue line indicates the control obtained by the positioning of the pump beam. The pump position affects the coupling efficiency of the light emitted by the quantum well material into the cavity modes and is represented by artificially changing (increasing or decreasing) the cavity Qs. Although the pump position can be used to impact both modes equally, changing the pump position is most effective for favoring one mode over the other (which is why the blue line is drawn orthogonal to the red). Therefore, adjusting both the pump power and position in concert is an effective method of controlling a cavity's Q-switching regime. 111

- 4.34 Schematic illustrating electrode fabrication procedure with polyimide isolation layers. (a) The process begins with a fully fabricated PC sample. (b) The first polyimide dielectric layer is patterned around the PC lasers and cured. (c) Next, the first electrode mask pattern is transferred into photoresist (not shown) on top of the polyimide layer. Electrodes are then evaporated and the remaining photoresist dissolved using standard lift-off processing techniques. The first electrode mask contains the 2 electrodes required to make the first electrode pair. (d) Next, the second polyimide isolation layer is patterned and cured. (e) Lastly, the second electrode mask is then used with another lift-off process to create the second pair of electrodes. Note that two of the electrodes are wired together so both pairs share a common ground. The second polyimide layer serves to isolate the electrodes from the previous ones (where appropriate). The positive slope of the polyimide film means the electrodes can be evaporated on top of both cured polyimide layers simultaneously and remain contiguous (e). Consequently, the second pair of electrodes are evaporated onto the same level as the first around the PC, as required to generate the planar electric fields needed for the Q-switching implementation. By studying the polyimide and electrode masks shown in figure 4.35, one can see how the various layers fit together to create the electrode structure schematically shown in (e). 113

- 4.35 Schematic of masks for electrode fabrication. (a) The full mask plates with all the mask layers superimposed on each other. The PCs are in the middle of the masks and the electrode leads extend outward to the wirebonding pads around the perimeter. (b) A close-up showing the mask layers surrounding several PCs. (c) A close-up showing the detailed electrode structure around a single PC cavity. (d)-(g) This sequence of images shows the electrode and isolation layer progression around a single PC. The first mask (d) defines the initial polyimide layer used to isolate the electrodes from the PC semiconductor slab. The second mask (e) produces the first set of electrodes. The third mask (f) defines the second isolation layer that primarily isolates the two electrode layers from each other. The fourth mask (g) patterns the second set of electrodes around the PC. Note the two sets of electrodes have a common ground. 114
- 4.36 Scanning electron micrograph of a PC sample with redesigned etch guides. The modified etch guides are designed to make the sample more resilient to multiple spin processing steps as compared to original “peninsula design” (see figure 4.10). 116
- 4.37 Schematic and gain spectra for proposed interleaved quantum well structure. a) Schematic showing a PC constructed from a slab containing an interleaved quantum well structure with one set of quantum wells optimized for emission at 1450 nm and the other at 1550 nm. b) An illustrative plot of the proposed quantum well gain spectra. Each set of quantum wells contributes one peak to the gain spectra and the peaks are arbitrarily separated by 100 nm. Gaussian distributions are used to represent the individual gain spectra peaks and are chosen merely for illustrative purposes. 117

List of Tables

3.1	InGaAsP wafer specifications. The active region is comprised of 4 quantum wells optimized for emission at $1.55 \mu\text{m}$. The quantum wells are compressively strained to favor coupling to the PC cavity's TE modes and are centered within the 330 nm thick slab.	44
4.1	Detailed specification of Q-switched cavity design. Any cavity parameter which is not explicitly specified is to be taken as the unaltered crystal value.	87
4.2	Classification of various Q-switching regimes and their experimental signatures.	109

Glossary of Acronyms

DWDM Dense wavelength division multiplexing

EO Electro-optic

FDTD Finite-difference time-domain

ICP/RIE Inductively coupled plasma reactive ion etch

LC Liquid crystal

OSA Optical spectrum analyzer

PC Photonic crystal

PECVD Plasma enhanced chemical vapor deposition

PIM Polarization interference microscopy

PMMA Polymethylmethacrylate

Q Quality factor

RIE Reactive ion etch

SEM Scanning electron microscope

VCSEL Vertical cavity surface emitting laser

Chapter 1

Introduction

Optical resonators are the cornerstone of many of today's technologies, and their usage spans both scientific and commercial domains [1]. The extent to which resonators pervade society can be seen even by confining one's view to their use as the feedback mechanism in lasers [2]. Simply put, lasers are everywhere. They are critical elements in DVD-ROMS, supermarket scanners, modern telecommunication systems, laser guided weapons, printers, astronomy (atmospheric distortion correction), laser pointers, fusion research, laser cooling and trapping, etc. Generally speaking, in these and other applications the utility of a resonator is usually derived from its geometry, quality, and the material comprising the resonator. As widely used and as important as the standard resonators are, further improvement is possible by augmenting these resonators with new materials. The central theme of this thesis is the investigation and pursuit of increasing the functionality of optical resonators through their integration with polymeric and fluidic materials.

Resonators can broadly be classified into two categories with the discerning characteristic being how the light propagates within the resonators. Traveling-wave resonators are structures in which light propagates in cyclic orbits around the resonators. Examples of such resonators include micro-spheres [3], toroids [4], and rings [5, 6]. Such resonators have been used in lasers [7], chemical sensors [8, 9], and filters [10, 11]. A silicon ring resonator is the first resonator system investigated in this thesis. The second resonator classification is referred to as standing-wave resonators. In contrast to traveling-wave resonators, light propagating in standing-wave resonators does not travel in orbits but rather is reflected back upon itself, forming a standing optical

wave. These resonators have also been used in chemical sensors [12] and filters [13] but are most commonly used in lasers. Although a laser cavity can be constructed using either type of resonator, the standing-wave resonator is the dominant form for such a purpose. In its simplest incarnation, such a resonator can be assembled by placing two aligned mirrors opposite each other [2, 14, 15]. Light trapped with the resonator reflects off one mirror and propagates to the second where it is reflected back towards the first, enabling the process to begin anew. These “traditional” resonators have been used not only for the development of the earliest ruby lasers, but also in the later generations of lasers including the gas discharge, organic dye, excimer, and solid state lasers [2]. The semiconductor-based implementations of these resonators emerged in the 1970’s with the advent of dielectric stacks or “Bragg mirrors.” These carefully engineered semiconductor heterostructures were first used to create the mirrors in miniature, distributed feedback lasers [2] and later as vertical cavity surface emitting lasers (VCSELs) [16–18]. In some respects, the dielectric stacks, which rely on Bragg reflection to confine the light within the resonator, are one-dimensional photonic crystals (PCs) and are the precursor to the modern two-dimensional PC cavities, the second type of resonator system investigated in this thesis [13].

The thesis begins with an investigation of various materials for use with traveling-wave silicon ring resonators, which makes for the logical starting place for several reasons. First of all, the ring resonator system is easier to characterize than the other PC resonators. For example, unlike PC cavity resonances, a ring resonator’s resonances are well described by analytic expressions. Secondly, many of the principles and motivations behind integrating the rings with other materials carry over to the PC resonators. Third, since it is relatively difficult to design and fabricate sufficiently high-quality-factor (high-Q) PC resonators, we can use the ring resonators to perfect the material integration and then transplant the knowledge and experience to the PC cavity integration experiments.

In chapter 2 we discuss our efforts to integrate ring resonators with electro-optic (EO) polymer and liquid crystal (LC), with the goal of electrically tuning the resonators’ resonant wavelengths [19]. Our initial attempt for electrical tuning involves using EO polymer as the resonators’ cladding layer, but this method ultimately fails

due to the polymer's poling requirement. After encountering insurmountable difficulties with the EO polymer integration, we switch to using LC as the cladding material and tuning element. The LC integration is a success, and we are able to electrically tune the resonators by realigning the LC in the cladding.

Chapter 3 discusses efforts to electrically tune PC laser cavities, supporting a single high-Q mode, by infiltrating the porous structures with LC and constructing a LC cell around the lasers [20]. As with tuning of the rings, the PC cavities are tuned by realigning LC with electric fields. The existence of a Fredericksz transition in the LC is verified, and its onset is found to coincide with the onset of tuning. The observed laser tuning ranges are less than the range predicted by simulations. The laser tuning behavior is believed to be dominated by the LC anchoring to surfaces. In particular, the tuning range is decreased because the anchoring inhibits the LC from completely aligning to the field in both the cladding layers and within the PC holes.

In chapter 4, we apply the principles of electrically tuned PC lasers to create novel optically triggered Q-switched PC lasers [21]. The PC cavities enabling the Q-switching of the lasers possess *two* orthogonally polarized high-Q cavity modes. Due to the orthogonally polarized nature of the modes, the relative Qs of the modes can be controlled by rotating the infiltrated LC. The rotation of the LC is the underlying mechanism enabling the Q-switching of the lasers and selection of the lasing mode. The Q-switching enables control over both the wavelength and the polarization emission from the lasers. Unlike in the previous chapters, the LC orientation is not controlled electrically but rather it is optically controlled with a layer of photoaddressable polymer (PAP). The LC follows the orientation of the PAP which, in turn, can be controlled with a polarized green laser.

Some final comments regarding organization are in order. Since the same resonators, material systems, and experimental techniques are used in multiple experiments, they are introduced at the beginning of the chapter in which they first appear. For example, polarization interference microscopy (PIM) is used extensively in chapters 3 and 4 but is introduced in chapter 2. Lastly, five external movie files are referenced in the thesis. The movies are in QuickTime format and can be downloaded from Caltech's web site. A sequence of images taken from each movie is included as

figures in the thesis for essential clarity, but viewing the more informative movies is recommended.

Chapter 2

Tuning Ring Resonators

In this chapter we introduce the ring resonator as the first resonator system under investigation. Ring resonators are the appropriate starting point in this thesis due to their relative simplicity. In many ways the ring resonator is the most straightforward of the resonator systems, especially since many of the issues concerning polymeric and fluidic integration are also relevant to the PC resonators (as discussed later in the thesis). The experience, knowledge, and methodology acquired from the ring resonator tuning experiments are built upon in the later chapters. This chapter begins with an introduction into the materials used for integration with the rings. The first section briefly discusses the properties and fabrication procedures of EO polymer, the first of the two materials integrated with the rings. Liquid crystal, the second material integrated with the rings, is introduced in the next section with a discussion of its physical and optical properties including their alignment behavior. Various aspects of PIM, an experimental technique used in characterizing LC and birefringent materials in general, is then discussed. Polarization interference microscopy is an extremely useful tool for analyzing the behavior of our devices and resurfaces throughout the thesis. Section 4 introduces the basic properties of ring resonators, the methodology employed in tuning the resonators, and the device geometry used in the experiments. Section 5 discusses issues with integrating the rings with EO polymer and LC. Experimental tuning results are presented at the end and the chapter concludes with a discussion of future possible directions in the research.

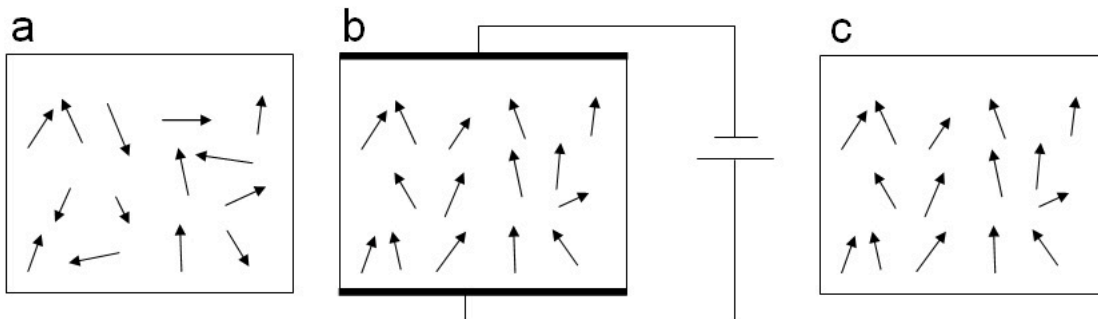


Figure 2.1: Schematic of EO polymer poling process. (a) Initially the polymer is randomly oriented. To produce a nonzero, second order nonlinear optical response, the material's centrosymmetry must be broken. To realize this, the polymer is heated in the presence of a strong electric field (b). The electric field aligns the polymer. (c) The alignment is stable when the sample is cooled.

2.1 Electro-Optic Polymer

Electro-optic polymer is polymer that exhibits second order optical nonlinearities. The polymer's refractive index can be changed upon application of an electric field. The optical nonlinearities are created by charge transfer of the π electrons [22] and so the response times of these polymers are thus extremely short (typically on picosecond time scales [23]). Recent improvements in the design of these polymers have significantly increased their electro-optic coefficients to 100 pm/V and beyond [24]. Considering electro-optic modulation is a second order nonlinear effect, noncentrosymmetry is required in the material to create an overall change in its refractive index [25]. To produce the required ordering in the polymer, the polymer is heated in the presence of a strong electric field ($\sim 100\text{V}/\mu\text{m}$) (see figure 2.1). This poling process aligns the polymer along the field, which breaks its centrosymmetry. The strong electric fields required for poling can be an obstacle for integrating the polymer with some materials. Another potential problem with EO polymer integration is the polymer's susceptibility to photochemical degradation. This problem can be largely surmounted by simply enclosing the polymer in an inert (oxygen deprived) atmosphere though [25].

2.1.1 Applications

The short response time for the refractive index modulation of the EO polymer makes it suitable to be used in modulators for telecommunication systems. Recently an EO

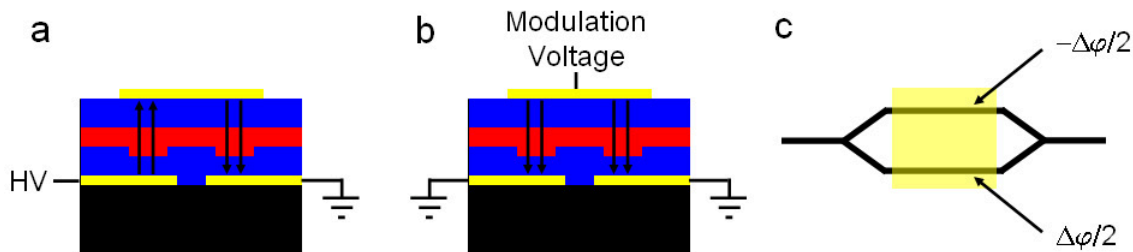


Figure 2.2: Schematic of an EO polymer-based Mach-Zehnder modulator. (a) First, the EO polymer (red) in each interferometer arm is poled in opposite directions. (b) After poling, a modulation voltage applied across each arm causes the refractive index to change in opposite directions. (c) Light traveling in one arm experiences a negative phase shift, whereas light in the other arm experiences a positive phase shift as compared to the unbiased interferometer. Interference occurs when the light is recombined at the output port. The amount of transmitted light can be modulated by adjusting the accumulated phase difference between the arms with an applied voltage.

polymer-based modulator has been reported which operates at voltages as low as 0.8 V [26]. There have been others which reportedly operate above 100 GHz [27]. The modulator features a push-pull Mach-Zehnder geometry where the arms are poled with electric fields of opposite polarity (see figure 2.2). The arms are then modulated with fields of the same polarity, which in turn increases the refractive index of one arm and decreases it in the other. This refractive index disparity causes a phase difference to accumulate for the light propagating down the two arms and, hence, causes interference when the light recombines at the output port. So, in effect the modulator output can be controlled by adjusting the phase difference between the two arms with a voltage applied across the arms.

2.2 Liquid Crystal

An enormous variety of materials exhibiting diverse physical properties and behavior are classified as LCs. Indeed, some have even gone so far as to label LCs the fourth state of matter. Although the distinction of being a separate state of matter has certainly lost a bit of prestige due to the ever increasing physical systems claiming that label (Bose-Einstein and fermionic condensates perhaps being the most recent [28–30]), LCs are indeed fascinating materials in their own right and present researchers with an extremely rich and interesting system for investigation. Generally speaking, LCs exhibit properties and characteristics which are intermediate between

solid crystalline materials and disordered liquids. A particular LC placed in appropriate environmental conditions can possess a high degree of positional and orientational order and resembles conventional crystals even in a liquid phase, whereas the same LC in slightly different environmental conditions can lose all crystallinity and transform into an isotropic liquid.

Liquid crystals often have complex phase diagrams where minor environmental changes induce transitions between substantially different (even multiple) phases. Liquid crystals can broadly be organized into two categories with the defining criteria being whether the LC's phase is *primarily* dependent upon ambient temperature (thermotropic) or the LC's concentration (lyotropic). Although this research solely utilizes the thermotropic LCs, a brief survey of the lyotropic variety is given for completeness.

Although lesser known than thermotropic LCs, lyotropic LCs were actually the first to be discovered and are commonly found in biology [31]. Solutions of biomolecules such as proteins, DNA, and even viruses can self-assemble and form ordered conglomerates. Amphiphilic molecules dissolved within an appropriate solvent comprise another class of lyotropic LCs. These molecules consist of a polar head and one or more hydrocarbon tails (soap dissolved in water is a common example). For a range of concentrations of soap molecules, the lowest free energy state is when the molecules organize themselves to shield the hydrocarbon tails from the polar aqueous environment (see figure 2.3). The formation of bilayer lipid cell walls in organisms is another example of amphiphilic molecules organizing into a well-defined phase.

Of the two classes of LCs, thermotropic LCs are the more commonly known. These LCs are usually rod-shaped molecules with their phase primarily determined by the ambient temperature. In general, as the temperature is decreased from the clearing point (temperature above which the LC is randomly oriented), the LC settles into phases exhibiting increasing levels of order. The nematic phase is the phase which possesses the least degree of order, exhibiting only orientational order and no long-range positional order (see figure 2.4 (a)). Most LC-based optical devices such as displays utilize nematic LCs.

The next phase with an increased degree of order is the smectic phase. This phase

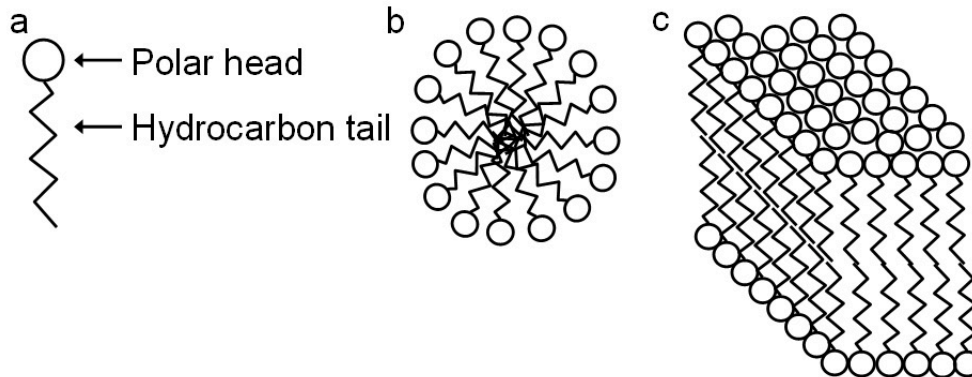


Figure 2.3: Schematic illustration of lyotropic LCs and phases. (a) Amphiphilic molecules (polar head with hydrocarbon tail) dissolved in water are an example of lyotropic LCs. (b) At certain concentrations the molecules self-organize into spherical micelles, which form to shield the hydrocarbon tails from the polar aqueous environment. Another stable configuration of amphiphilic molecules is the bilayer structure shown in (c). These structures are routinely found in biology, of which a cell wall is an example.

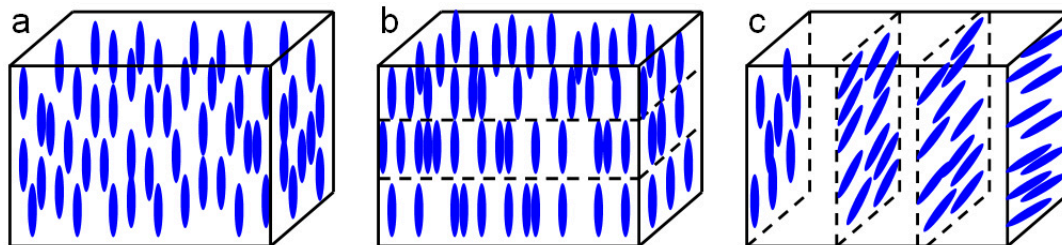


Figure 2.4: Schematic of three common LC phases. (a) Nematic phase exhibits orientational order but no positional order. (b) Smectic phase possesses additional positional order with the LC segregated into two-dimensional planes. (c) Cholesteric phases exist with numerous variations, but a defining characteristic is the LC organizes into spirals.

is characterized by LCs oriented in the same direction in addition to being organized into layers (see figure 2.4 (b)). This phase contains both positional and orientational order. The other phases exhibit steadily increasing levels of order until ultimately the LC closely resembles a crystal. A third phase found in thermotropic LCs is formed by “bownana” (bent) shaped molecules which can self-assemble into periodic spirals (see figure 2.4 (c)). This phase is referred to as the cholesteric phase, exists in nematic and smectic flavors, and has been studied for its PC properties.

2.2.1 Physical and Optical Properties

The LCs discussed in this thesis are all thermotropic, uniaxial, and are in the nematic phase at room temperature (all experiments are conducted at room tempera-

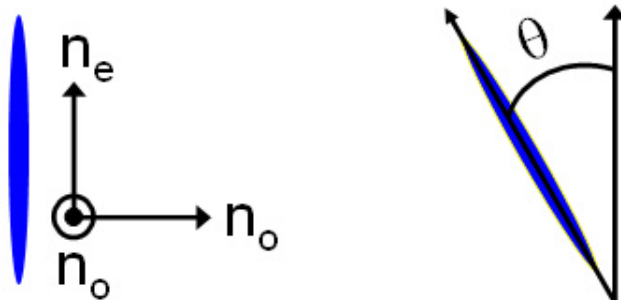


Figure 2.5: Physical structure of LC molecules. The molecules are ellipsoidal in shape with their so-called director defined as being parallel to the molecules' long axis. Light polarized parallel and orthogonal to the director experience a refractive index n_e and n_o , respectively. Light polarized at an angle θ to the director experiences a refractive index given by equation 2.1.

ture). These LCs are rod-like molecules and have a “director,” which is defined to be the direction parallel to the molecule’s long axis (see figure 2.5). Uniaxial LCs are described by two refractive indices, the extraordinary (n_e) and the ordinary (n_o) refractive index. Light propagating through the LC and polarized along the director and orthogonal to the director experience¹ a refractive index of n_e and n_o , respectively. For light polarized at an oblique angle θ to the director, the effective refractive index may be found by constructing the index ellipsoid and is given by

$$n(\theta) = \frac{n_o n_e}{\sqrt{n_o^2 \cos^2 \theta + n_e^2 \sin^2 \theta}} \quad (2.1)$$

Normal LC birefringences ($n_e - n_o$) typically range from approximately 0.05 to 0.3 at 589 nm and generally decrease with increasing wavelength. The birefringence of an LC is an important parameter for integration with optical resonators because it provides an upper bound for the optical-path-length-tuning we can expect to achieve.

Beyond birefringence, another important consideration when integrating LCs with optical resonators is the additional optical losses associated with the integration. This topic is discussed further elsewhere in the thesis, but for now we confine the analysis to the LC’s optical properties. Two parameters that can impact the Q of a resonator integrated with LC are absorption and scattering caused by the LC. Fortunately the absorption at the wavelengths of interest ($\sim 1.55 \mu\text{m}$) is believed to be minimal and

¹The LC we used was uniaxially birefringent and so can be viewed as being cylindrically symmetric about the molecule’s long axis (director).

so is not a concern. Scattering, however, may be an issue depending on the particular LC used. In our case, it can clearly be seen by looking at a milky white vial of LC that scattering is present in imperfectly aligned LC. The scattering is due to dielectric constant inhomogeneities, with the scattering intensity dependent upon both the magnitude of the dielectric (director) fluctuations and also the prevalence of the fluctuations [31]. Regardless of the scattering parameters (incident, final k-vectors, etc.), the scattering scales as the square of the LC's dielectric anisotropy ($\epsilon_{\parallel} - \epsilon_{\perp}$). The precise calculation of scattering expected by the LC is quite involved and particularly difficult considering the degree of LC alignment and orientation in the vicinity of the resonators are not accurately known. The resulting significant uncertainty surrounding the validity of any scattering calculation leads us to conclude they are too unreliable to be performed at this time. Scattering should not be completely ignored, however. At higher resonator Qs, further increases in these Qs are limited by correspondingly lower loss sources, and so scattering from random director fluctuations may eventually become the dominant loss mechanism for such resonators.

2.2.2 Liquid Crystal Alignment Methods/Freedericksz Transition

The ability to control an LC's orientation and, hence, its optical properties is the primary basis for the material's use in optical devices. Although numerous methods exist to align LC, only a few of the more common and relevant methods are discussed here. The two primary orientations LC can possess in the vicinity of a flat surface are referred to as homeotropic and homogeneous (or planar), with the directors oriented perpendicular and parallel to the surface, respectively (see figure 2.6).² In equilibrium, the orientation an LC exhibits coincides with the configuration that minimizes its free energy [32]. Homogeneous orientations are commonly induced by creating grooves along a surface by rubbing the surface with a material such as silk [33] (see figure 2.6 (a)). Homeotropic orientations can be induced by coating a surface with a surfactant [33] (see figure 2.6 (b)). In the first case, the orientation is largely determined by steric, or geometric, influences, whereas in the second, intermolecular interactions likely become more significant. These alignment methods describe static alignment

²Tilted LC orientations can also be induced by an angled surface.

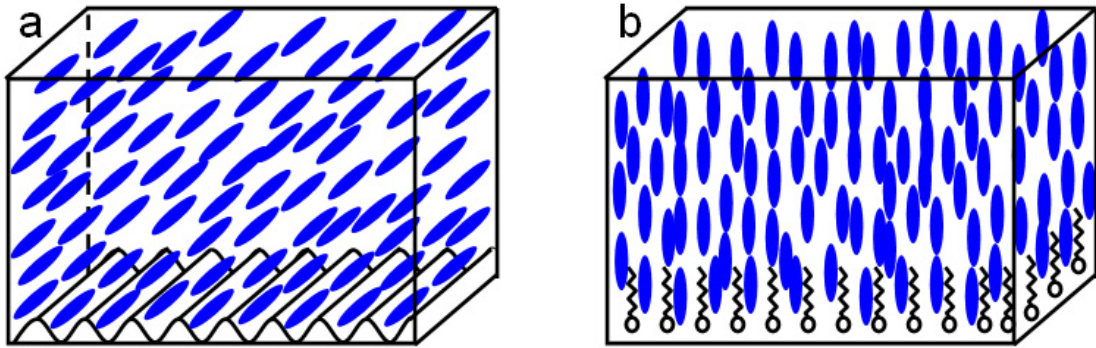


Figure 2.6: Illustration of homogeneous and homeotropic LC alignment. (a) Homogeneous (planar) LC alignment can be induced by rubbing grooves into a surface. (b) Homeotropic alignment can be induced by coating a surface with surfactant molecules. If the density of surfactant molecules is sufficiently low, then the LC molecules can fill the gaps in between them and cause the LC molecules to orient parallel to the surfactant molecules.

of LC, but some dynamic methods also exist.

The LC orientation can be easily and dynamically modulated by applying either electric or magnetic fields. Take for instance the case where LC exhibits homogeneous alignment when placed between two horizontal plates with an electric field oriented vertically (see figure 2.7 (a)). The LC's orientation is determined by the minimization of the free energy which now contains both the usual elastic energy contribution and now an electric field interaction energy term. By carrying through with the analysis and making various approximations which can be found in many standard LC textbooks [32], one discovers the threshold electric field marking the onset of LC alignment along the field (Fredericksz transition) is

$$E = \frac{\pi}{d} \sqrt{\frac{K_i}{\epsilon_o \Delta\epsilon}} \quad (2.2)$$

where d is the distance between the plates, K_i is the appropriate elastic constant for the specific LC/electric field configuration, ϵ_o is the permittivity of free space, and $\Delta\epsilon$ is the LC's dielectric anisotropy ($\epsilon_{\parallel} - \epsilon_{\perp}$). By looking at equation 2.2 one immediately sees the threshold field for the Fredericksz transition is inversely proportional to the distance. In other words, the threshold voltage is a constant, irrespective of the plate separation. As the voltage is increased beyond threshold, the bulk LC continues to align with the field but the LC near the plates remain anchored and do not align

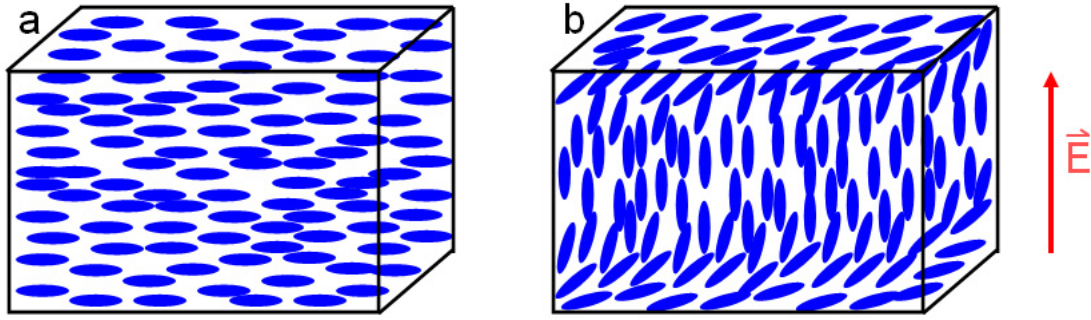


Figure 2.7: Illustration of Freedericksz transition in LC. (a) Initially the LC features homogeneous alignment. (b) When a voltage is applied across the LC cell that exceeds the threshold voltage, the LC undergoes a Freedericksz transition and aligns parallel to the field. Note the LC near the surfaces are anchored, which inhibits the realignment.

appreciably to the field [34, 35] (see figure 2.7 (b)). The distance from the plates through which the LC orientation is dominated by the surface anchoring is referred to as the characteristic length.

Two comments regarding the alignment of LC with electric fields are worth noting. One of the drawbacks of LC is that the realignment occurs relatively slowly. Since large molecules are being rotated, the timescales that govern the process are understandably relatively long. For this reason, LC-based devices are normally operated in the kilohertz regime. The second point concerns the existence of a Freedericksz transition. The previous analysis featured an electric field orthogonal to the initial director orientation. For such configurations Freedericksz transitions do occur. If the field and directors are not initially orthogonal, then a Freedericksz transition may not exist. In this case, the LC will smoothly and progressively rotate towards the field direction as the voltage is increased [36].

2.2.3 Applications

Liquid crystals are commonly used in spatial light modulators for display applications. This application illustrates many of the operational principles common to other LC-based devices and serves as a canonical example. One implementation of the modulator utilizes a twisted nematic LC geometry, and its operation is shown in figure 2.8. Incident light initially passes through the polarizer and is polarized in the vertical direction. With no voltage applied across the cell, the light's polarization ro-

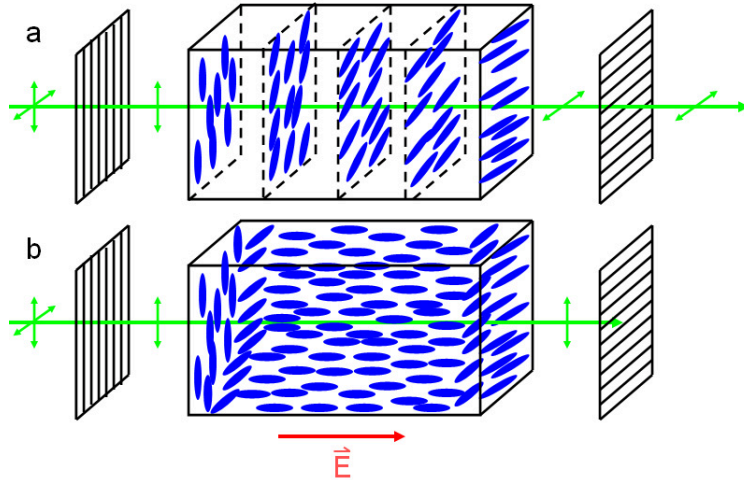


Figure 2.8: Illustration of a twisted nematic LC spatial light modulator. The two plates at the ends of the LC cell are rubbed in orthogonal directions. In the absence of an applied voltage (a), the rubbed plates induce a spiral orientation in the LC. Vertically polarized light enters the cell, and the polarization rotates along with the rotation of the LC. Horizontally polarized light exits the cell and passes through a horizontally oriented polarizer. (b) When a voltage is applied across the cell and triggers a Freedericksz transition, the polarization of the light traversing the cell no longer rotates. Now the light is blocked by the second polarizer. In effect, transmission of light through the cell can be modulated with an applied voltage.

tates while traversing the cell, following the rotation of the LC directors [14, 36].³ The polarization is rotated by 90° and is transmitted through a second polarizer which is oriented horizontally. When a voltage is applied across the cell, the LC aligns with the field and the polarization of the light traversing the cell no longer rotates because the polarization axis is now perpendicular to the LC's director and therefore is blocked by the second polarizer. Consequently, the transmission of light through the cell can be modulated by the voltage applied across the cell.

2.3 Polarization Interference Microscopy

Polarization interference microscopy is an experimental technique useful for characterizing birefringent materials. Polarized white light is shone onto a sample, the reflected (or transmitted) light is passed through a second polarizer oriented perpendicular to the first, and the result is imaged (see figure 2.9) [37]. Upon striking a uniaxial birefringent sample, the white light can be perceived to be split into two

³The spiraling LC pitch must be sufficiently long for the polarization of the light to rotate along with the rotation of the LC. In other words, the LC cell needs to be operating in the Mauguin waveguiding regime.

components, one propagating with a refractive index n_o and the other $n(\theta)$ (given by equation 2.1). As the light traverses the sample, a phase difference accumulates between the two components which is given by

$$\delta = 2\pi(n_o - n(\theta))\frac{d}{\lambda} \quad (2.3)$$

where δ is the phase delay, d is the sample thickness, and λ is the wavelength of the light. Interference between the two components occurs when the light is recombined with the second polarizer (analyzer). The resulting colorful image can be used to infer the sample thickness, birefringence, or sample orientation with the aid of a Michel-Levy chart (see figure 2.10) [37]. In our case, we know the LC's birefringence and usually accurately know the sample thickness as well. Polarization interference microscopy therefore becomes a method to obtain information regarding the LC's orientation. As an example, we show a picture provided by Professor Oleg Lavrentovich of the Liquid Crystal Institute at Kent State University [38]. The picture was taken using PIM and shows a disclination defect in a nematic LC film (see figure 2.11). The black spiral patterns are known as "Maltese crosses" and suggest the LC is oriented radially, azimuthally, or a combination of the two around point defects. The four black spirals emanating from the point defects indicate the regions where the LC is oriented such that one of its optical axes is parallel to the incident light's polarization axis. When this happens, no "splitting" of the incident light occurs and no phase delay is accumulated. The second polarizer blocks all the light and the result is a black image. A black image also occurs when looking at an optically isotropic sample, regardless of the sample's orientation. Another point worth mentioning is that the rotation of a birefringent sample changes only the brightness of a PIM image, but not its color. This can be seen by realizing for any given wavelength, rotation of the sample merely changes the amount of light at that wavelength that is transmitted through the second polarizer. Furthermore, since rotation of the sample affects the proportion of light transmitted by all of the wavelengths equally, the transmitted power spectrum remains the same except for a scaling factor.

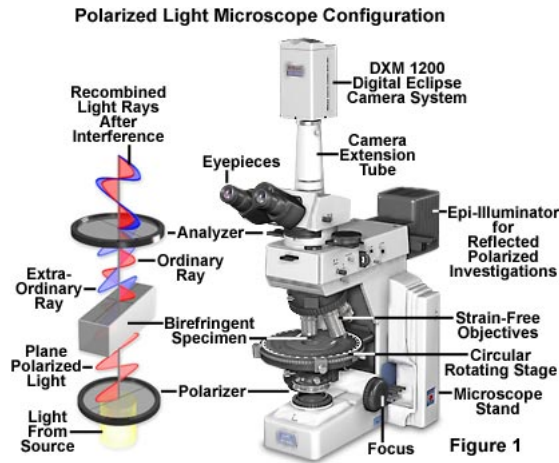


Figure 2.9: Schematic of PIM technique. Polarized light impinges upon a birefringent material. While traversing the sample, the ordinary and extraordinary components experience different refractive indices and a phase difference is accumulated between the two waves. The two waves are combined and interfere at a second polarizer which is oriented orthogonal to the initial polarization axis. The resulting interference pattern provides information regarding the sample's birefringence, thickness, and orientation. Note our PIM configuration differs from the one shown. In our setup the light originates from above the sample, is reflected from the bottom of the sample, traverses the sample again, and finally exits at the top.

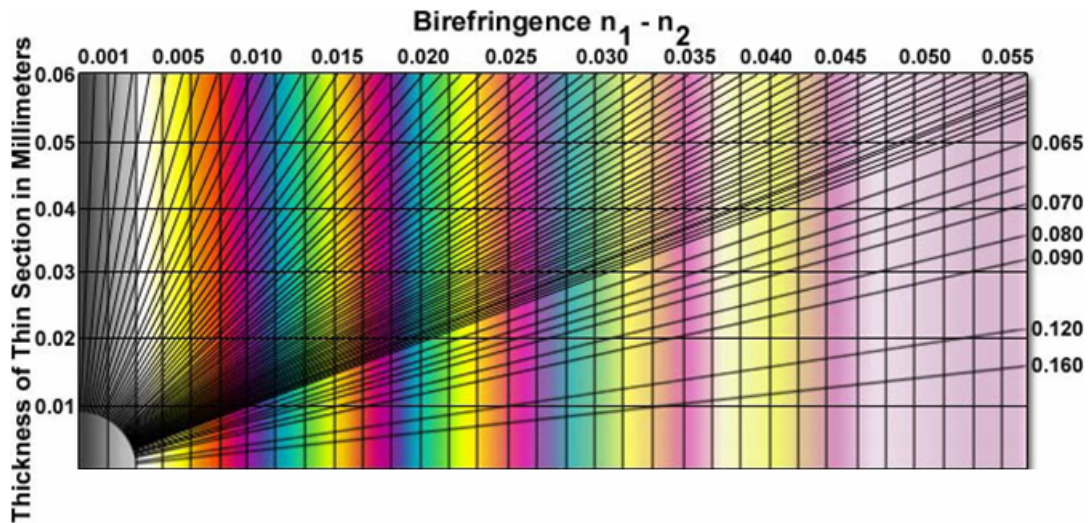


Figure 2.10: Michel-Levy chart showing the possible colors observed when using white-light illumination for PIM. The resulting color is not only a function of the sample's birefringence and thickness but is also dependent on the sample's orientation (orientational-dependent effective birefringence). For our purposes, we generally know the LC's birefringence and thickness that is being investigated, and so PIM primarily provides information regarding the LC's orientation. Consequently, PIM is useful in evaluating the effectiveness of the various LC alignment methods discussed in this thesis.

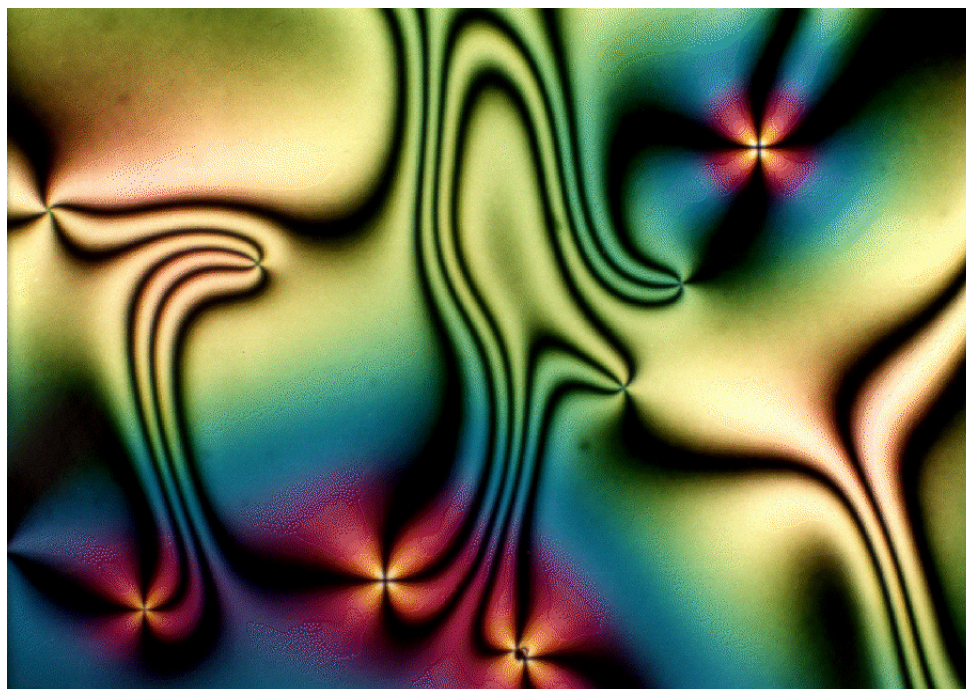


Figure 2.11: A beautiful PIM image showing point defects in nematic LC films [38]. The point defects are clearly identified by the “Maltese crosses.” The alignment of the LC around the defects and throughout the film can be inferred by the structure of the dark regions and by observing the movement of the black regions while rotating the sample under the polarizers. For a planar LC orientation, the dark regions are where the LC is aligned parallel to one of the two polarizers used in the PIM setup.

2.4 Ring Resonators

Ring resonators are traveling-wave resonators and closely resemble micro-toroid and micro-sphere resonators [3, 4]. They are fabricated as large as millimeter scale with low refractive index contrast materials such as Si_3N_4 , or polymer, and as small as a few microns using high index contrast semiconductor materials [5, 6]. To a good approximation (ignoring backscattering induced resonance splitting effects [39]), these resonators have well defined resonances corresponding to wavelengths of light that undergo an integer number of 2π phase shifts upon propagating around the ring. Recently, rings have been designed and fabricated with Qs exceeding 10^4 with a large free spectral range, which increases as the rings shrink [40]. These favorable optical characteristics, combined with a fabrication procedure that is compatible with conventional semiconductor processing techniques, make rings attractive for potential telecommunication applications.

Much interest in the past has focused on using rings as add-drop filters in telecommunication networks (see figure 2.12). The high refractive index contrast available in SOI ring resonators enables low-loss and high-Q filters with radii down to a few microns. Such resonators can be designed as notch filters for adding or dropping individual channels in the telecommunication bands and can be densely integrated in photonic networks [41–45]. For reconfigurable dense wavelength division multiplexing (DWDM) systems and to compensate for temperature changes, it is desirable to tune the precise channel frequency dropped by such resonator add/drop multiplexers.

2.4.1 Tuning Methodology

Two primary methods exist to control the optical path length of a ring resonator and thus tune its resonant frequencies. To statically tune a ring resonator one can either adjust the physical dimensions (in particular the ring's circumference) or construct the ring from materials with different refractive indices. Dynamically tunable resonators provide another level of functionality over statically tuned resonators and are most practically obtained by dynamically controlling the refractive indices of the constituent materials comprising the resonators. Dynamic tuning is commonly achieved

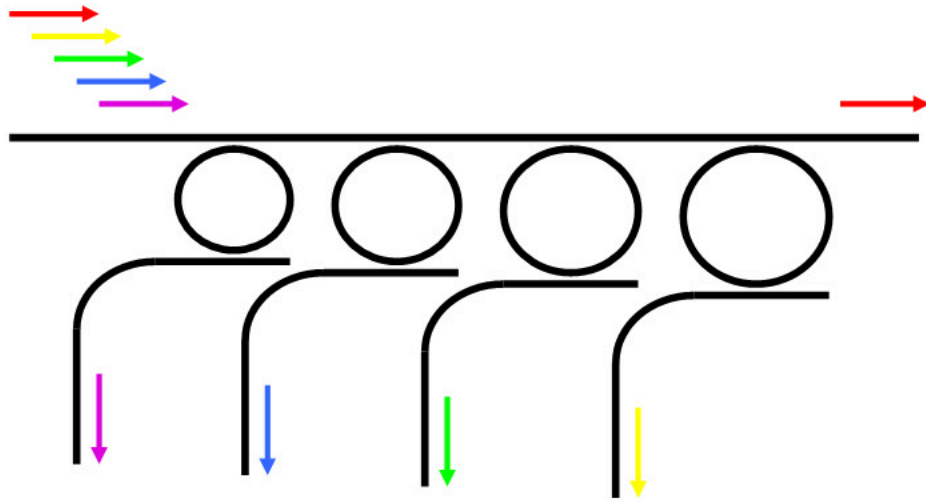


Figure 2.12: An illustration of a series of ring resonators serving as telecommunication filters. Each resonator is designed to be resonant with only one wavelength and drops that wavelength into a second waveguide. By concatenating a series of resonators with slightly different radii, many wavelengths can be simultaneously multiplexed on a chip.

by thermally changing the refractive index, traditionally by introducing a heater close to the resonator [46, 47]. However, power dissipation provides a serious problem in such tunable ring resonator designs, especially when many resonators have to be densely integrated in a DWDM multiplexing system. In this chapter we investigate the possibility of tuning ring resonators by changing its cladding refractive index by depositing EO polymer and LC around the rings.

2.4.2 Device Geometry and Sample Fabrication

Chips containing thousands of ring resonators were provided by Luxtera Inc. for integration and testing. The specific resonator geometry we investigated was fabricated from a silicon-on-insulator (SOI) wafer with silicon thickness of 205 nm, oxide thickness of 1 μm , ring radius of 5 μm , and ring and waveguide widths of 500 nm (see figure 2.13 (a)). The resonator was coupled to one waveguide, which served as both the input and output port, and was separated from the resonator by a 100 nm gap. The rings were initially encased in silicon dioxide and were immersed into a buffered HF oxide etch solution for 5-6 minutes (~ 70 nm/min etch rate) to expose the top and sides of the rings for later integration with either EO polymer or LC (see

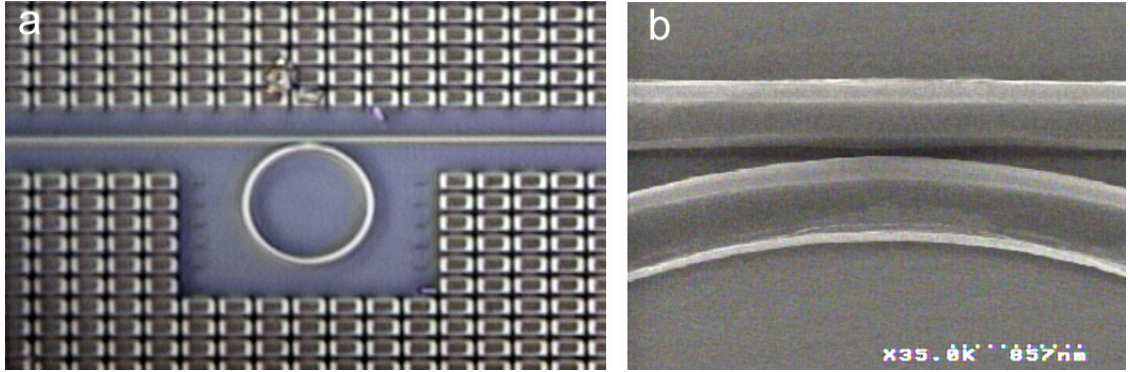


Figure 2.13: Images showing ring geometry. (a) Optical microscopy image of representative ring resonator. The ring radius is $5\ \mu\text{m}$, waveguide widths are $500\ \text{nm}$, and waveguide-ring gap is $100\ \text{nm}$. The silicon rectangles surrounding the resonator exist for planarization purposes during chemical-mechanical polishing. (b) A scanning electron microscope (SEM) image taken after the oxide etch showing the exposed ring sidewalls.

figure 2.13 (b)). Modulation electrodes were required for both the EO polymer and LC integration. The details of the electrode fabrication process are described later in the chapter.

2.5 Ring Integration with EO Polymer

We first discuss our attempts to integrate ring resonators with EO polymer. Although the refractive index change in EO polymer is fairly small (typically 10^{-3} - 10^{-4}), this drawback is partly compensated by the high frequency at which the refractive index can be modulated (GHz frequencies). In addition to using the rings as add-drop filters, the high modulation frequency theoretically possible with EO polymer integration potentially enables the rings to be used as modulators in telecommunication systems. Modulation of the EO polymer's (as well as LC's) refractive index required specific patterning and deposition of electrodes to provide the necessary electric fields. The electrodes were aligned to specific resonators on the chips, photolithographically defined, and deposited using standard lift-off processing. Negative photoresist NR1-3000PY from Futurrex was chosen for its negative-sloping sidewalls, which were conducive for lift-off processing. A negative tone resist was also convenient for precise alignment of the mask to the resonators because it enabled the majority of the chip to be viewed during the alignment and exposing steps. A $3\ \mu\text{m}$ layer of resist was

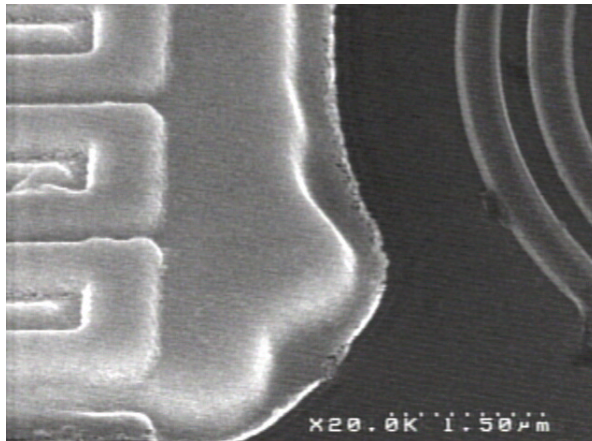


Figure 2.14: An SEM image showing the uneven electrode surface caused by the silicon rectangles protruding from the surrounding oxide. Evaporating thick electrodes were required to guarantee they were contiguous, given the uneven surface on which the electrodes were deposited.

spun onto the samples at 4800 RPM for 40 seconds and then baked on a hotplate at 150°C for 1 minute 15 seconds. The resist was exposed for 30-35 seconds and then underwent a post-exposure bake on a hotplate at 103°C for 1 minute 20 seconds. The resist was then developed with Futurrex RD6 developer for 15-20 seconds. Electrodes were then deposited by evaporating 500 nm of gold onto a 5 nm chromium adhesion layer. The thick layer of gold was required to guarantee contiguous electrodes, which were deposited on an uneven surface (see figure 2.14 (a)). The resist was then removed with Futurrex stripper RR4, which completed the lift-off process. The combination of a long metal evaporation with a resist featuring a significant undercut profile can result in poorly defined electrodes. During evaporation, a thin layer of metal migrated and became deposited under the overhanging resist (see figure 2.14 (b)). Lastly, it is worth noting that our judicious choice and spacing of alignment marks yielded consistent sub-diffraction-limited alignment of the electrode masks to the rings.⁴ Electrodes were routinely aligned to the rings to within 100 nm accuracy even though modest objective magnifications (10x) were used during the alignment process.

⁴Throughout the course of the research we experimented with numerous alignment marks and obtained the best accuracy by simply using widely separated concentric circle alignment marks. Small (i.e. below the diffraction limit) deviations from perfect alignment could be discerned (but not resolved) by observing subtle asymmetries around the circular alignment marks. Aligning multiple widely separated alignment marks enabled exceptional rotational as well as spatial alignment accuracy.

2.5.1 Electro-Optic Polymer Deposition and Poling

The EO polymer deposition and poling procedure described here is meant to be representative. Some variability existed in the procedure executed from one sample batch to another. First, 11% by concentration CLD-1 EO polymer was spun on the chips at 1000 RPM for 2 seconds. The samples were then pre-baked at 40°C for 1 minute and subsequently baked at 120°C for 30 minutes to remove the solvent. At this point, electrodes could be deposited on top of the polymer if needed for vertical poling or modulation.⁵ Otherwise, the samples were now ready to be poled using the in-plane electrodes (see figure 2.15 (a)). For poling, a voltage was applied across the electrodes to yield an electric field of approximately 100 V/ μm throughout the polymer. While the voltage was applied, the temperature was first ramped for 10 minutes up to 150°C, maintained at this temperature for 30 minutes, and then cooled back to room temperature. Unfortunately, the strong fields required for poling exceeded the breakdown field of silicon (30 V/ μm), and so the samples were destroyed during the poling process (see figure 2.15 (b)). Ultimately this problem could not be overcome with the ring geometries provided to us, and so we switched to integrating the ring resonators with LC. The EO polymer integration with ring resonators effort has continued elsewhere in the group, however, and some progress has been made. For instance, employing a split ring geometry bypasses the silicon breakdown problem during the poling process by using the ring structure, itself, as the electrodes [48].

2.6 Ring Integration with LC

Unable to surmount the problems afflicting the EO polymer poling, we refocused our efforts to integrating the rings with LC. Although LC modulation operates at much longer timescales ($\sim\text{kHz}$ frequencies), key advantages associated with LC are modest modulation voltages and large birefringences. The LC chosen to integrate with the rings was E63 from Merck and had a relatively large birefringence ($n_e = 1.744$, $n_o = 1.517$ at 589 nm). The LC, when spun onto the resonators at 4000 RPM for 40 seconds, formed the resonator's top and side cladding layers. The spinning process initially

⁵Vertical electrode configurations were also tried for EO poling but failed for the same reasons as the in-plane poling efforts.

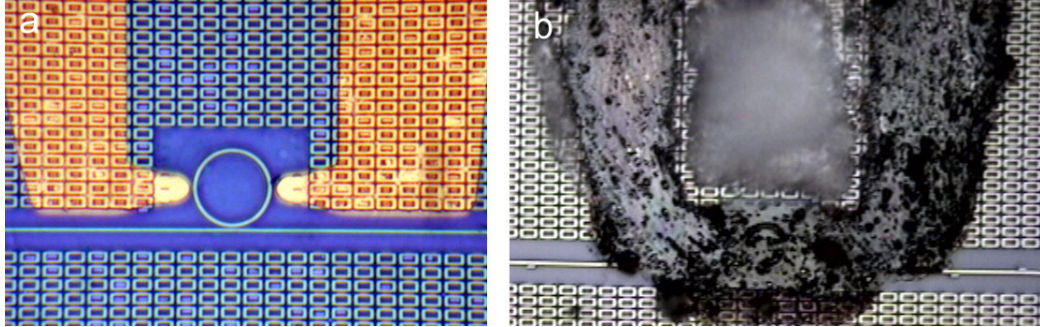


Figure 2.15: Optical microscopy images showing silicon breakdown during EO polymer poling. (a) In-plane electrodes were aligned to the resonator and evaporated. Electro-optic polymer was then spun on top of the rings and electrodes and was then ready to be poled. (b) The poling process requires strong electric fields ($\sim 100 \text{ V}/\mu\text{m}$) that exceed silicon's breakdown potential ($\sim 30 \text{ V}/\mu\text{m}$). Consequently, the silicon in between the electrodes broke down during poling and completely destroyed the resonator.

created nice films, but the surface tension present in the films eventually caused the LC to coalesce (over a period of hours) and form a droplet. For this reason, the LC was spun immediately before testing. The coalescing can be prevented by placing a coverslip on top of the sample. Lastly, no alignment layer was used to induce a preferred LC alignment around the ring.

2.7 Experimental Characterization and Tuning Results

In our devices light from a tunable semiconductor laser was grating coupled, both into and out of the respective ports. The grating couplers selectively coupled and transmitted the waveguide's single TE mode (electric field in the plane of the resonator). The resonators' resonances were measured by recording the power from the output port while sweeping the wavelength of the laser. Scans were taken with different electric potentials applied across the electrodes. As mentioned previously, the resonances of the rings correspond to the wavelengths of light coupling into the resonator which undergo a phase shift of an integer multiple of 2π upon one revolution in the resonator. The resonance wavelengths can be determined by modifying the Fabry-Perot etalon resonance equation to obtain [14]

$$\lambda_m = \frac{2\pi R n_{eff}}{m} \quad (2.4)$$

where $m = 1, 2, 3, \dots$, λ_m is the wavelength of the m^{th} resonator mode, R is the radius of the resonator (measured from the center to midpoint of ring), and n_{eff} is the effective refractive index of the waveguide mode. From equation 2.4, we can infer that the essence of dynamically tuning a resonator lies in changing n_{eff} . Fortunately, the TE waveguide mode contains evanescent tails that penetrate into the LC cladding, and so n_{eff} is partly dependent upon the LC cladding refractive index n_{clad} . For the TE guided mode, the contribution to n_{clad} of a LC molecule is given by equation 2.1, where θ now represents the angle between the LC director and the ring's radial axis.

The initial tests of electric tuning of ring resonators with LC used the first generation of in-plane electrodes designed for the EO polymer poling and modulation (see figure 2.16 (a)). These tests produced no resonance tuning even though PIM measurements confirmed that the LC reoriented to the applied field. A thorough analysis of the simulated field pattern generated by the electrodes using FEMLAB (a finite element simulation package) revealed the probable cause for the absence of electrical tuning. Albeit unlikely, the field pattern generated by the particular electrode geometry first tested essentially balanced the radial and azimuthal field contributions (see figure 2.16 (b)). The radial field component aligns the LC's director parallel to the light's polarization axis and increases the effective cladding refractive index, whereas the azimuthal field component aligns the LC's director orthogonal to the polarization axis and decreases the effective cladding refractive index. Balancing these two field components around the entire ring leads to no overall tuning if the LC is initially randomly oriented in the plane of the ring resonator.

Two new electrode configurations were designed to correct the field balancing problem. The first revised design shown in figure 2.17 (a) is meant to mimic the idealization of infinitesimal line electrodes on either side of the resonator. This configuration maximizes the azimuthal field component while minimizing the radial component (see figure 2.17 (b)). The second revised design shown in figure 2.18 (a) essentially strives to achieve the opposite of the first design by surrounding the resonator as much as possible with the electrode structure. This geometry maximizes the radial field component while minimizing the azimuthal component (see figure 2.18 (b)).

More samples were fabricated with this new generation of electrode designs and

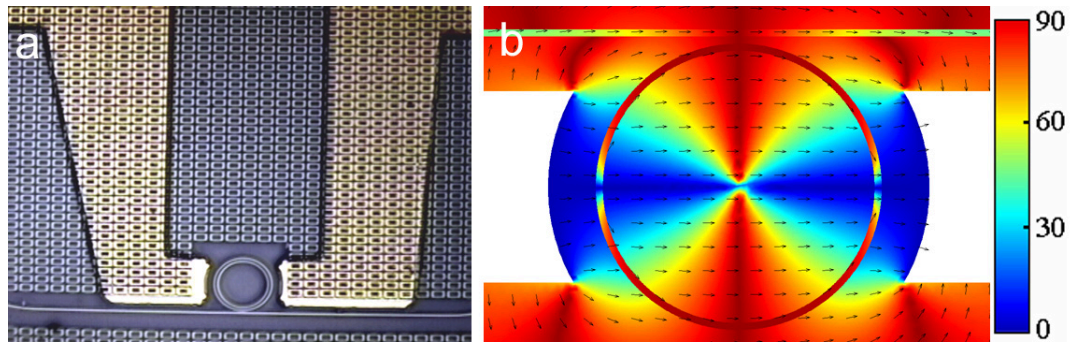


Figure 2.16: Optical microscopy image of electrodes and the corresponding electrostatic simulation of their generated electric field pattern. (a) Optical image of first electrode design used for LC tuning of ring resonator experiments. The rings could not be tuned with LC using this electrode geometry. One possible explanation can be found in the electrostatic simulations (b). The electrostatic simulation is a plot of the angular difference of the field direction and the ring's radial axis. Blue corresponds to purely radial field (0°) and red is purely azimuthal (90°). The simulations reveal that the azimuthal (red) and radial (blue) field components are roughly balanced when integrated around the entire ring. For this unusual case, no tuning is expected due to LC aligning to the field, and so new electrode geometries were designed and used. The resonator shown in (a) is a double ring resonator, but the rings actually tested are the single rings with geometries mentioned earlier in the chapter.

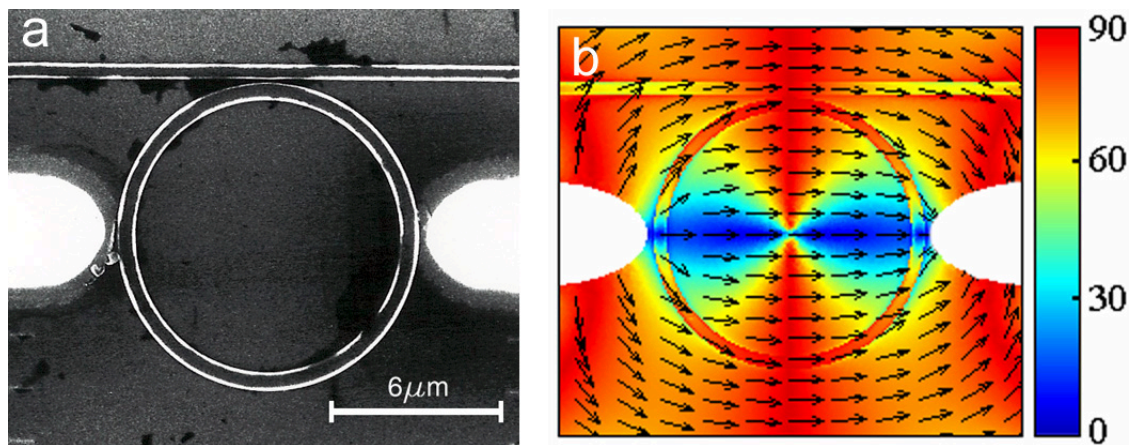


Figure 2.17: An SEM image of azimuthally-biased electrode configuration and the associated electrostatic field simulation. (a) Scanning electron micrograph of fabricated electrodes designed to maximize the azimuthal field component while minimizing the radial component. (b) Electrostatic simulations showing the electric field pattern produced by the electrode configuration. The angular difference of the field direction and the ring's radial axis is plotted. Blue corresponds to a purely radial field (0°) and red is purely azimuthal (90°).

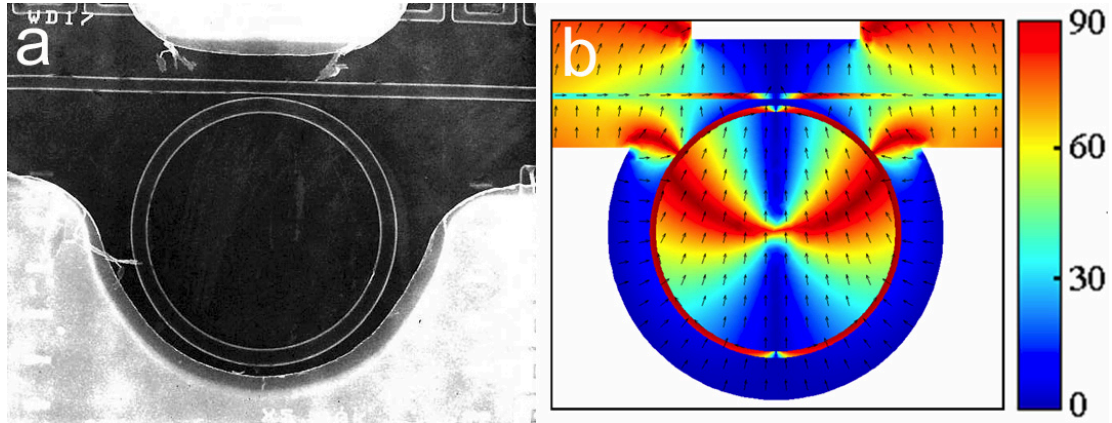


Figure 2.18: An SEM image of radially-biased electrode configuration and the associated electrostatic field simulation. (a) Scanning electron micrograph of fabricated electrodes designed to maximize the radial field component while minimizing the azimuthal component. (b) Electrostatic simulations showing the electric field pattern produced by the electrode configuration. The angular difference of the field direction and the ring's radial axis is plotted. Blue corresponds to purely radial field (0°) and red is purely azimuthal (90°).

tested. One such sample is shown in figure 2.17 (a). The left and right electrodes are approximately 4.0 microns wide and spaced about 400 nm and 300 nm from the resonator, respectively. The modulation electrodes preferentially orient the directors of the LC molecules azimuthally (parallel) to the resonator wall. Equation 2.1 shows that n_{clad} is expected to decrease towards n_o , in turn decreasing n_{eff} . A decreasing n_{eff} causes the resonances to shift to shorter wavelengths, as shown by equation 2.4. We recorded wavelength scans while applying potentials of 0-20 V across the electrodes and monitored the resonator drop frequency with a tunable laser. The resulting data for three resonances are shown in figure 2.19. Note that the resonance shift is in the expected direction, opposite of what would be the case if the resonator were being heated by absorption of the laser or leakage currents across the electrodes [49]. Similar tuning results were also obtained for rings with electrodes optimized for radial fields, but the resonances were red-shifted instead of blue-shifted. The resonance shifts were independent of field polarity and were completely reversible. After removing the electric field the resonances returned to their original wavelengths.

For the azimuthal optimized electrodes we obtained a maximum resonance shift of approximately -0.22 nm (27.5 GHz at $1.55 \mu\text{m}$) by applying 20 V. To correlate our experimental results with the degree of LC alignment, we start with a modified form

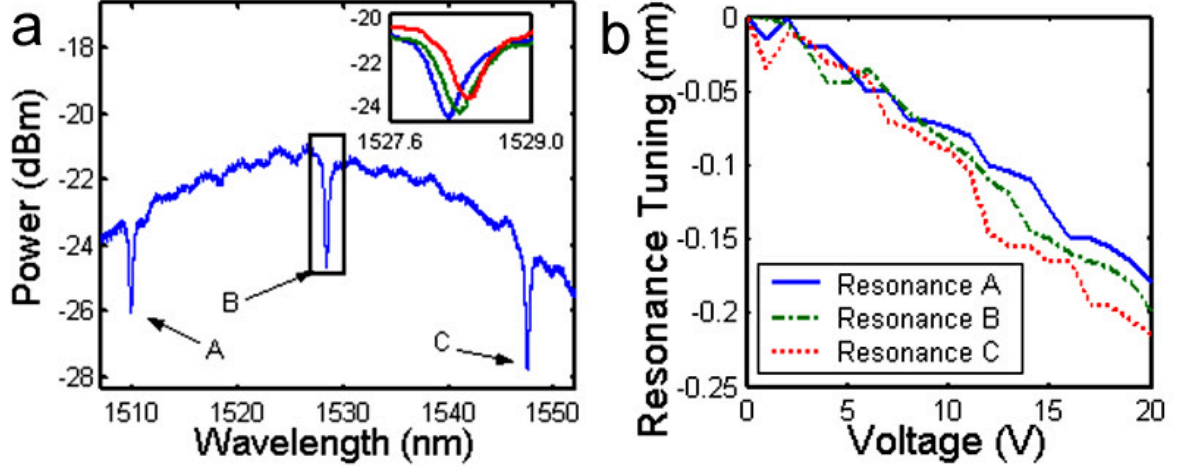


Figure 2.19: Experimental realization of LC-mediated ring resonator tuning. (a) Plot of collected transmitted power as a function of wavelength showing three resonances. (inset) Close-up of resonance B taken with 0 V, 10 V, and 20 V applied across the electrodes. (b) Resonance tuning as a function of voltage applied across the electrodes. All three resonances blue-shift approximately 0.20 nm at 20 V, and no threshold is observed in the tuning data, indicating the absence of a Fredericksz transition in the LC.

of equation 2.4 and obtain

$$\Delta\lambda_m = \left(\frac{\partial n_{eff}}{\partial n_{clad}}\right) \frac{\lambda_m \Delta n_{clad}}{n_{eff}} \quad (2.5)$$

where $\Delta\lambda_m$ is the shift in resonance wavelength, $\frac{\partial n_{eff}}{\partial n_{clad}}$ is the derivative of n_{eff} with respect to n_{clad} , and Δn_{clad} is the change in the cladding refractive index due to LC alignment.

We assume with zero applied electric field the LC is randomly oriented. For E63, this corresponds to an n_{clad} of 1.596.⁶ We subsequently used this n_{clad} in finite-difference time-domain (FDTD) simulations to estimate n_{eff} and $\frac{\partial n_{eff}}{\partial n_{clad}}$ for the three resonant wavelengths under study. Then, by using equation 2.5 we solve for $\frac{\partial \lambda_m}{\partial n_{clad}}$ and obtain the resonance wavelength sensitivity to n_{clad} (see figure 2.20). Using this in conjunction with the wavelength shift data, we obtain a Δn_{clad} of only -0.002 for all three resonances. Based on our electrostatic modeling for the azimuthally biased electrode configuration, in the LC saturation field regime we would expect a Δn_{clad} of -0.034. Though the applied voltage exceeds E63's saturation voltage of ~ 2 V, the resonances continue to shift up to the maximum applied field and appear as though

⁶The refractive index at IR wavelengths is likely to be lower than at visible wavelengths. This difference can help account for the discrepancy between the simulated and realized tuning of the ring resonators discussed below [50].

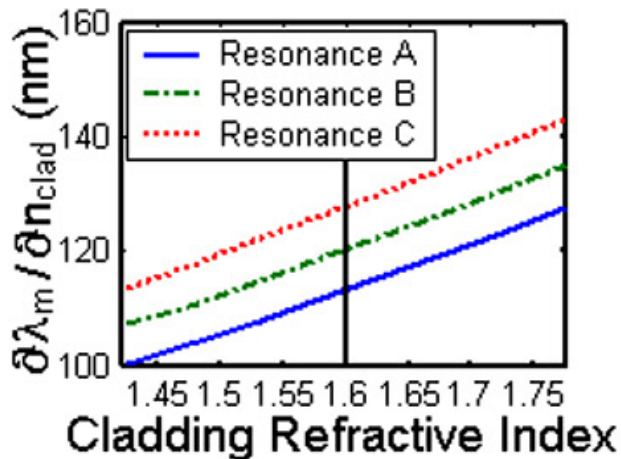


Figure 2.20: Plot of the resonance sensitivity to changes in the cladding refractive index. The resonance sensitivity increases with increasing cladding refractive index. This relationship is attributed to the fact that a larger fraction of the mode overlaps with the cladding as the cladding's refractive index increases. The black line corresponds to the cladding refractive index expected if the LC is randomly oriented around the ring.

the tuning would continue if the voltage is increased further. This indicates the applied electric field is insufficient to achieve complete LC alignment, and it partly explains the disparity between the calculated and measured Δn_{clad} values.

There are several sources of error which may further explain the disparity. First, the fabricated electrodes are not identical to the electrodes used in the electrostatics modeling. As can be seen in figure 2.17 (b), the modulation electrodes used in this study align the LC azimuthally, radially, or a combination of the two, depending on the position around the ring. The tuning of the resonances results from the relative imbalance between azimuthal and radial LC alignment, which in turn is extremely sensitive to the electrode geometry. The electric field generated by the fabricated electrodes may differ substantially from the simulated field and thus explain the significant difference between measured and simulated Δn_{clad} values. Other sources of error may include any unexpected reorientation and surface anchoring of the LC. These last two possibilities are best examined using PIM.

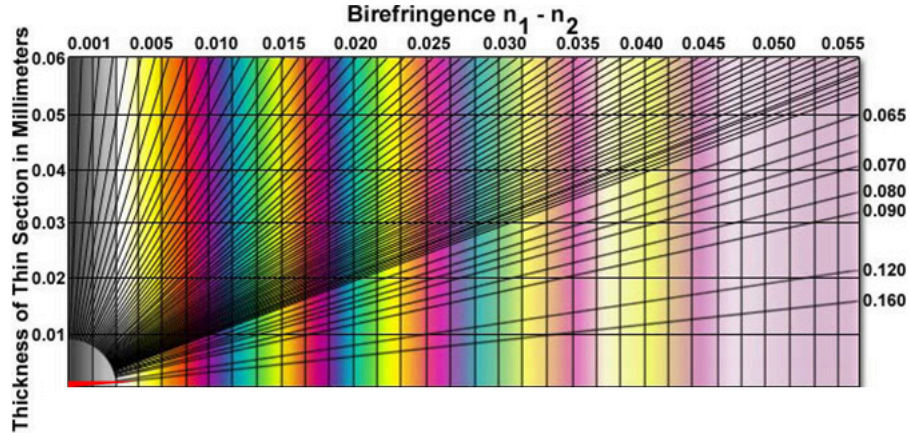


Figure 2.21: Michel-Levy chart indicating the possible colors for the PIM imaging of the LC ring resonator cladding. Considering the LC layer is exceptionally thin (sub-micron), we are confined to the extreme lower left corner of the chart, denoted by a red triangle. This suggests we can only obtain gray scale variations in the PIM images due to LC realignment.

2.7.1 Polarization Interference Microscopy Analysis of LC Alignment

Imaging the ring resonators using PIM while ramping the voltage applied across the electrodes reveals two aspects of the LC reorientation. First, the spun LC film is thin (most likely sub-micron), and so the Michel-Levy chart suggests we can only observe gray scale changes in the PIM images (see figure 2.21). As the voltage is ramped, the LC continuously reorients along the field and no threshold voltage is observed. The lack of a Fredericksz transition is expected given the electrode geometry employed. The electric field is not uniform and not orthogonal everywhere with respect to the LC. In such circumstances a Fredericksz transition does not occur [36]. The second observation aided by PIM is the LC's alignment not occurring as expected given the simulated electric field pattern (e.g., the apparent LC reorientation lacks the symmetry present in the simulated electric field pattern)(see figure 2.22 and external movie file ringPIMmovie.mov). The alignment is probably impaired by either surface anchoring to the ring, surface anchoring around defects, or by unexpected field patterns. The impaired LC alignment may further explain the discrepancy observed between the simulated and measured change in the cladding refractive index.

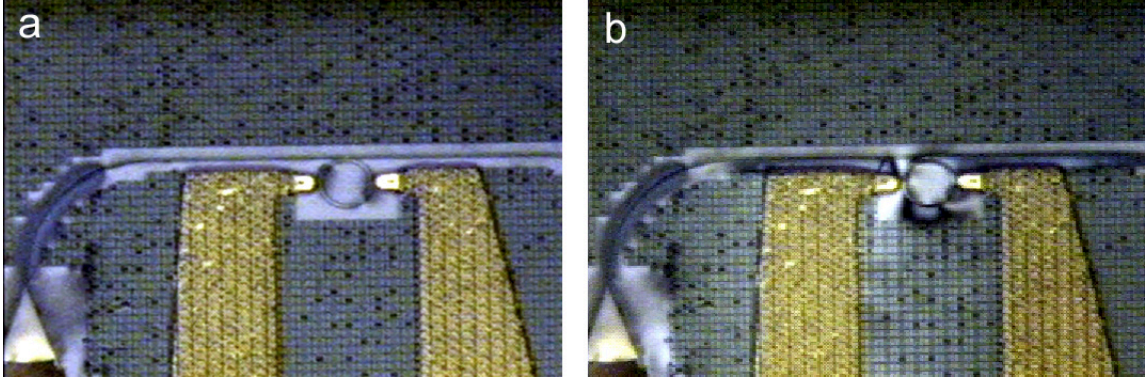


Figure 2.22: Polarization interference microscopy images of a ring with LC cladding. The images were taken with (a) 0 V and (b) 20 V applied across the electrodes. Although the precise LC orientation cannot be determined using the PIM images, it is clear the orientation lacks the symmetry of the simulated electric field. It appears the LC may be anchored to the ring surface and/or to defects around the ring. This can seriously impair the LC alignment and may explain the discrepancy between the expected and realized tuning of the resonators.

2.8 Discussion and Conclusions

Beyond creating tunable ring resonators for telecommunication applications, we also considered utilizing them as chemical and biological sensors. A ring can be used to detect analytes that approach the vicinity of the ring's surface. The analyte can either change the resonant wavelengths, modify the resonances' Qs, or a combination of the two. We inadvertently realized this while measuring a ring resonator coated with unpoled EO polymer. During the device characterization, which took place in the presence of oxygen (air), we observed a large resonance shift and also a change in the resonance's Q (see figure 2.23). These changes are attributed to the photochemical degradation of the EO polymer cladding. In this case the identification of the source of the resonance shift is straightforward given the luxury of knowing the cladding material. The difficulty in using rings as chemical sensors is obviously increased when the identity of the sample being tested is not already known. The difficulty is compounded further when multiple materials can cause similar changes in the resonators' optical properties. A couple of improvements can be implemented to circumvent these problems. First, a ring's surface can be functionalized to interact with a particular analyte which can then pinpoint the detection of that specific analyte. Second, large numbers of these functionalized rings can be fabricated with different resonant wavelengths on a single chip and integrated with micro-fluidic technology.

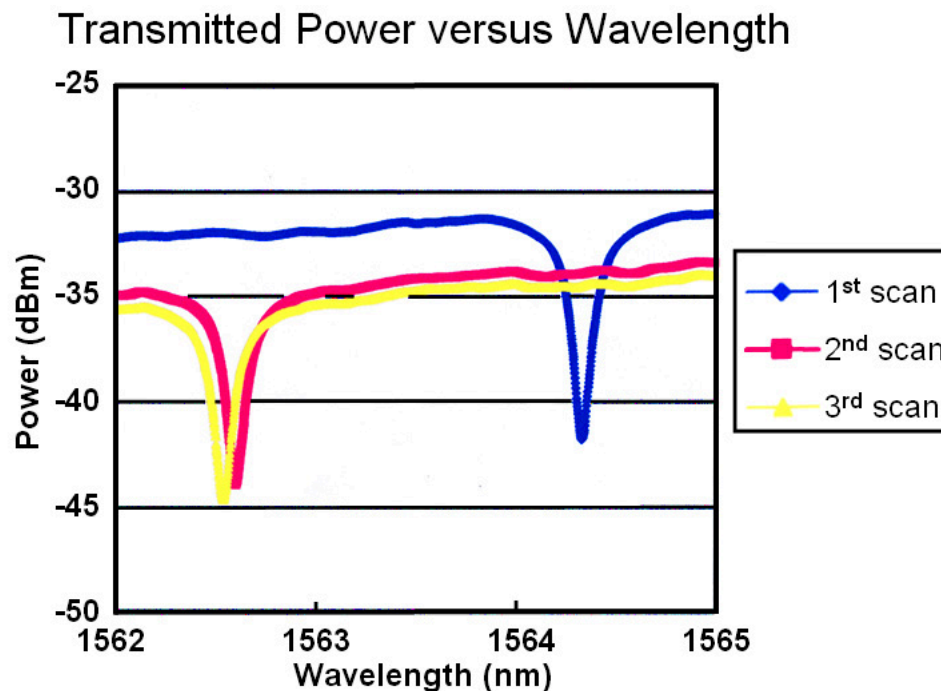


Figure 2.23: Demonstration of a ring resonator acting as a chemical sensor. Three scans, measuring the transmitted power past a resonator with an unpoled EO polymer cladding, were recorded over a period of approximately 20 minutes. Over the course of the scans the resonance was observed to blue-shift approximately 2 nm. The shift is attributed to a cladding refractive index change of $\sim 10^{-2}$ due to photochemical degradation of the polymer cladding. The detection of refractive index and absorption changes through the observation of resonance shifts can serve as the basis for using rings in chemical sensing applications.

Sophisticated data analysis algorithms can then be incorporated and transform the chip into a miniature detector array capable of accurately detecting multiple analytes simultaneously.

Chapter 3

Tuning Photonic Crystal Lasers

Chapter 2 introduced LC and discussed its successful integration to electrically tune ring resonators. In this chapter LC is utilized in creating electrically tuned PC lasers. Unlike previous tuning methods, this method enables both the precise and dynamic tuning of PC lasers' wavelengths. The chapter begins with a discussion of PCs and continues with a discussion of PC resonators and the motivation of LC integration with PC resonators. Section 3 presents the device specifications and cavity design. Section 4 addresses the multifaceted topic of integrating LCs within PCs. The section covers LC parameter considerations, LC cell construction, and introduces some characteristics of LC alignment in the vicinity of a PC slab. Section 5 presents the experimental characterization and demonstration of electrical tuning of PC lasers. The section begins with describing the experimental setup and procedures, continues with LC characterization and PIM analysis, and is followed by the laser tuning data. The section finishes with a discussion of the effect of LC domain orientation and surface anchoring on the tuning range and behavior. The chapter ends with discussion and conclusions.

3.1 Photonic Crystals

Photonic crystals are structures with periodic dielectric distributions in one, two, or three dimensions. One-dimensional PCs (or “Bragg stacks”) have been utilized as mirrors for over 20 years in applications such as distributed feedback lasers [2] and VCSELs [16–18]. The 1987 papers by Yablonovitch [51] and John [52] ushered in the

modern field of PC research, which has experienced exponential growth ever since. The immense interest in the field is largely due to a PC's ability to strongly manipulate the behavior of photons on a wavelength scale within the crystal. The exceptional control a PC exerts over photons can be explained by observing the analogies between PCs and semiconductor crystals.

A PC's dielectric distribution is in essence a periodic potential for photons, whereas semiconductors are periodic electronic potentials. The periodic electronic potential is the foundation of solid state physics and is responsible for the electronic properties of semiconductors. Therefore, it should come as little surprise that many solid state physics electronic phenomena have direct analogies with photons in PCs. Among the most important properties exhibited by PCs are their energy-momentum band structure, bandgaps, and defect states. Crudely speaking, the band structure determines the propagation behavior of photons within the crystals. For example self-collimation [53], negative refraction [54], and the so-called superprism [55] effects are a result of particular band structure features (flat, "inverted," and cusped equi-frequency contours, respectively). A PC possessing a complete bandgap prohibits the propagation of photons with energies within the bandgap in all directions and can also be used to inhibit the spontaneous emission of atoms and other emitters [51]. As with the doping of semiconductors, the introduction of defects within a PC pulls states from the bands into the bandgap. These defect states can then be used to localize and guide light within the crystal [56]. For instance, a point defect within a PC can localize light around the defect, creating a cavity. If a series of defects are strung together, then a waveguide can be created [57, 58].

Since the relatively recent emergence of the PC field, researchers have endeavored to fabricate higher dimensional PCs to access their more favorable optical properties. Although tremendous advances have been made in fabricating three-dimensional crystals [59–62], constructing these crystals remains time consuming and is still not commercially viable. Instead of fabricating three-dimensional PCs, many researchers employ two-dimensional PCs constructed from a semiconductor membrane. These structures offer a compromise between ease of fabrication and desired optical properties. Their two-dimensional nature makes them compatible with standard semi-

conductor processing techniques, while the refractive index contrast present in the membrane structure enables confinement in the third dimension due to total internal reflection. The PC research presented in this thesis is exclusively performed with two-dimensional PCs constructed from semiconductor membranes.

3.2 Photonic Crystal Resonators

Interest in PC cavities has steadily grown in recent years as researchers continue to discover new applications for their unique ability to strongly confine light in volumes approaching a cubic wavelength. These structures are suitable for (high-Q) nanocavities [63–65], optical filters [13], compact lasers [66], cavity quantum electrodynamics [67–69], and quantum information processing [70,71], among others. As promising and as diverse as these applications are, they are mostly based on “traditional” (air-filled) PC cavities. A relatively unexplored yet important aspect of PC cavities is that their intrinsic porous structure enables efficient integration with fluids [72,73] and polymers featuring a wide array of optical properties. Integrating PC cavities with these materials allows researchers to take full advantage of the tremendous design freedom and unique optical properties inherent in the cavities. Before we delve into the details of integrating these cavities with various materials, a brief background is provided regarding past efforts in designing the high-Q cavities required for their integration with other materials.

Photonic crystal resonators are created by placing defects within an otherwise unperturbed crystal structure possessing a bandgap. Associated with the defects are defect states within the crystal’s band structure which reside in the photonic bandgap and are pulled either from the dielectric band or air band depending on the nature of the defect [56]. Defect states pulled from the air band are preferable for our work because these states significantly overlap with the crystal’s holes, or equivalently with any material (e.g., LC) infiltrated within the crystal [12]. Air band defect states are created by locally increasing the amount of dielectric material in a region and can be easily achieved by decreasing the size of a single hole [56].

Much attention in PC cavity research has thus far been focused on designing cav-

ities with a maximum Q (and to a much lesser extent Q/V , where V is the cavity mode's volume). The rapid progress towards this end has been nothing short of astounding. Five years ago PC cavity Q s hovered around 2,000 [66], but today cavities have been reported with Q s exceeding 600,000 [65]. Although improved fabrication techniques likely are a contributing factor, the foundation for such a rapid improvement in cavity Q s is in the development of refined cavity design methodologies. The first systematic design methodology was proposed by Vučković et al. [74] and later advanced by Srinivasan et al. [75], who fabricated a cavity with a Q of several tens of thousands [63]. The idea underlying this methodology is that a cavity mode's spatial profile can be Fourier transformed into its k -space equivalent. Next, the designer strives to modify the cavity to minimize the mode components lying above the light-line.¹ These components are not confined by total internal reflection at the PC membrane/air interface and serve as a dominant loss mechanism in the cavities. Following this design rule has led to cavities with improved modal Q s, but a subsequent modification to this design rule proposed by Akahane et al. [64] has led to further cavity enhancements. Again, their goal is to minimize the Fourier components above the light cone, but they propose to do so by constructing cavities whose modal profiles resemble Gaussian wave packets as closely as possible. Initial results using this design rule showed the fabrication of a cavity with a Q of 45,000 [64], but this was soon followed by a completely different cavity design that supported a mode with a measured Q surpassing 600,000 and a simulated Q in the tens of millions [65].

Although tremendous progress has been made in designing cavities with maximum Q in air, very little attention has been devoted to designing cavities to optimize them using a different metric. For instance, in integrating LC with PC cavities we are interested in maximizing the cavity Q after LC infiltration (i.e., with an ambient refractive index of ~ 1.5) instead of a cavity immersed in air. Interestingly, we find that optimizing a cavity for air does not always yield a cavity which is optimized for a higher ambient refractive index. Cavities that possess relatively low Q s in air can have relatively high Q s in LC. This suggests that more work remains to be done in devising alternate cavity design methodologies for optimizing cavities based on

¹This design guideline is used in analyzing the cavity design in the next chapter.

metrics other than air-immersed Qs. The cavity design problem is discussed further in the next chapter.

3.2.1 Motivation for LC Integration/Previous Tuning Efforts

It has in the past been predicted that PCs will form the basis of future photonics systems. Indeed, many components of such systems have already been implemented, including laser sources [66], waveguides [57], and add-drop filters [13] among others. One potential obstacle for the future debut of PC-based systems is the stringent fabrication tolerances required for PC devices. This is particularly true for PC cavity devices, which are created by introducing defects within the PC structure. The resonances of such cavities are extremely sensitive to the precise defect geometry, and so specifying *a priori* the cavity resonances of a fabricated device pushes current fabrication technology to its limits. Currently, fabricating a cavity with a specific resonance wavelength entails fabricating a large number of devices and systematically tuning fabrication parameters (e.g., electron beam writing dose). Even so, such lithographic (static) tuning techniques yield cavities with a resonant wavelength resolution of several nanometers [76]. To alleviate this problem, a method to dynamically tune a cavity's resonances after fabrication is desirable. Dynamic tuning of PC lasers was first achieved by filling the PC holes with liquids of different refractive indices [12]. Since those early efforts it has been difficult to actively tune the emission frequency of PC lasers by deliberately changing the refractive index of the material inside of the cavity. To electrostatically tune PCs, infiltration of LCs into the pores of such structures was proposed several years ago [72]. Since then, several groups have demonstrated dynamic thermal tuning of PCs with infiltrated LCs [77–79], and more recently electrical tuning via LCs has been reported [80–82]. In this chapter we present our work on electrically tuning two-dimensional PC lasers by controlling the orientation of infiltrated nematic LC. This tuning method enables precise and dynamic tuning of the PC lasers and has not been achieved previously. As a side note, in the next chapter we move beyond the idea of using LC for optical-path-length-tuning of PC resonators and instead use LC integration to enable a completely new type of PC laser. This new PC laser is a Q-switched laser that exhibits enhanced functionality

over the electrical tuning presented in this chapter [21].

3.2.2 Tuning Methodology

The PC laser is tuned by modulating the refractive index in regions that overlap with the lasing mode. The refractive index change alters the cavity's effective optical path length and shifts the resonances. To see how a cavity can be tuned with LC, one can decompose light traveling through LC into two orthogonal components. One component always experiences the LC's ordinary refractive index while the other component experiences an effective extraordinary refractive index n_{eff} given by

$$n_{eff}(\theta) = \frac{n_o n_e}{\sqrt{n_o^2 \cos^2 \theta + n_e^2 \sin^2 \theta}} \quad (3.1)$$

where n_e and n_o are the LC's extraordinary and ordinary refractive indices, respectively, and θ is the angle between the light's polarization axis and the LC's director. Therefore, by rotating the LC with respect to the cavity, n_{eff} can be changed to tune the cavity. The tuning range is limited by the refractive index modulation in the holes and the top and bottom cladding layers. To maximize tuning, the modal overlap with these regions should also be maximized given the constraints dictated by the cavity's Q requirements. In light of this, the cavity geometry is chosen such that the optical mode's electric field maximum occurs within the central defect hole. Such cavities are particularly sensitive to the refractive index changes in the central hole and may also be used in sensing applications [12].

3.3 Photonic Crystal Cavity Design

The cavity design is one of three critical components in realizing PC lasers (the other two components are the specially designed wafer material from which the lasers are fabricated and the optimized fabrication procedures). Normally, the essential criterion governing the design process is the cavity's Q. A PC cavity must exhibit a sufficiently high Q in order for room temperature lasing to be possible. For our lasers we faced the further restriction of obtaining a sufficiently high Q *after* infiltrating the cavity with LC. Infiltrating the PC with LC decreased the refractive index contrast at the

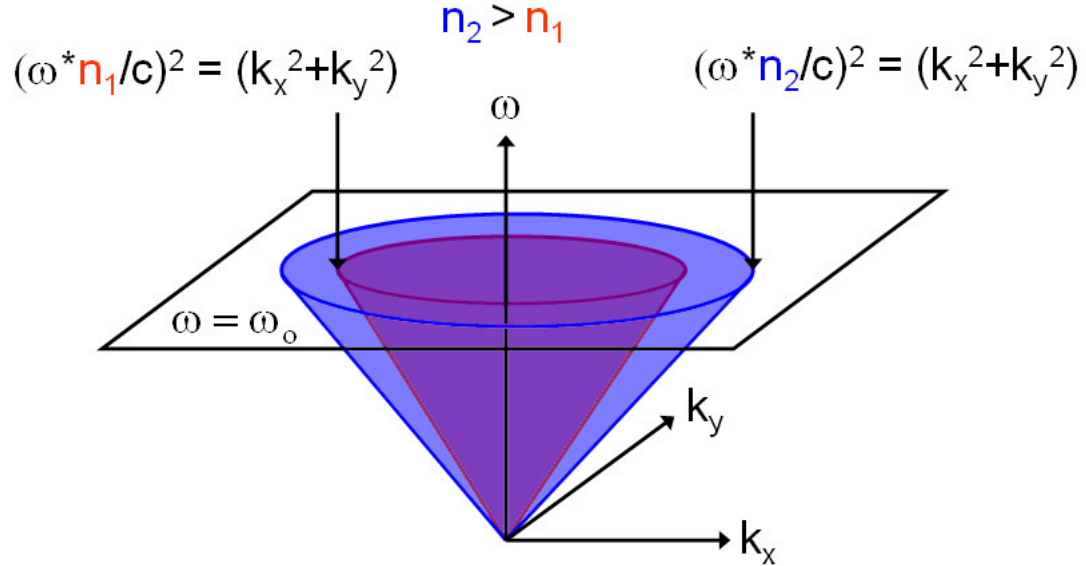


Figure 3.1: Schematic of cladding light cones. Light possessing k -vectors which lie above the cladding's (refractive index n_1) light cone can radiate into the cladding and are not well confined in the PC slab. Light below the light cone remains guided by the high index PC slab and undergoes total internal reflection upon striking the slab/cladding interface. Minimizing the Fourier components comprising a cavity mode that lie above the light cone is a technique for maximizing a mode's Q [64, 74, 75]. Increasing the cladding refractive index from n_1 to n_2 , however, increases the portion of k -space which lies above the light cone. A mode's Fourier components that lie between the two light cones are *now* no longer well confined and contribute to additional losses, lowering the mode's Q .

slab/cladding interface and reduced vertical confinement, which decreased the cavity's Q (see figure 3.1). Overcoming the decrease in vertical confinement was difficult and required a redesign of the PC cavities and involved extensive FDTD simulations.

A further constraint the cavity designs must have satisfied was the maximization of the tunability of the lasers with the infiltrated LC. This was achieved by maximizing the overlap between the optical field of the cavity mode and the LC. In our cavity designs, the central defect was obtained by shrinking an air hole, or equivalently viewed as increasing the local amount of dielectric material. Increasing the amount of dielectric material pulled states from the air band down into the bandgap. Such states strongly overlapped with the air holes and, as such, were ideal for interacting with infiltrated LC.

3.3.1 Photonic Crystal and Cavity Parameters

Photonic crystals provide researchers with enormous design freedom. For the cavity designer this design freedom is both a blessing and a curse. Although a PC defect cavity design may exist which satisfies the constraints of a given problem, discovering the design may be quite a challenge. Even though several researchers have studied the cavity design problem and have generated numerous insights [64, 74, 75], the design process retains an iterative component and can still be time consuming.

The bulk crystal parameters available to the cavity designer include lattice type, crystal periodicity, and hole size. Although researchers have also obtained high-Q cavities with square lattice PCs [63], we chose to construct our cavity from a triangular lattice PC because of its considerably wider bandgap (see figure 3.2). The wider bandgap was especially important considering the bandgap narrowing that occurred when the refractive index contrast was decreased after infiltrating a PC's holes with LC. Given a reduced refractive index contrast, the triangular lattice's considerably wider bandgap favored the existence of high-Q cavities over that of square lattice PCs. Due to the scale invariance of Maxwell's equations, the periodicity of a PC was largely determined by the wavelength region of interest (with some consideration given to the slab thickness, which normally can not be changed). The periodicity was chosen such that the bandgap considerably overlapped with $1.55 \mu\text{m}$, the engineered maximum in the quantum well emission (detailed quantum well specifications are discussed below). Our lasers had a 500 nm periodicity with a slab thickness of 330 nm. The bandgap width was also dependent on hole size, generally widening as the holes were enlarged [56]. As the holes became large, however, scattering in the vertical direction increased [83] and the structural integrity of the slab was diminished. As a compromise, our lasers featured normalized hole radii of 0.33 (r/a).

The cavity geometry consisted of a central defect shrunken hole ($0.2 r/a$) and two modified holes on either side (see figure 3.3). The modified holes were half-circles and half-ellipses with a minor axis length of $\sim 0.13 (r/a)$. The resulting cavity split the degeneracy of the orthogonally polarized X and Y dipole-like modes, which both featured electric field maxima in the central defect hole. Various plots of the mode

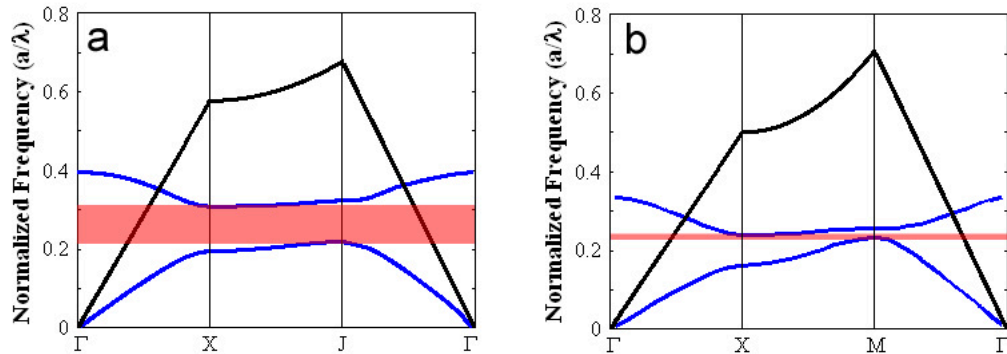


Figure 3.2: Representative two-dimensional band diagrams showing first TE-like bandgaps for triangular (a) and square (b) lattices. The photonic crystal refractive index is 3.4 and hole radii are 0.33 (r/a).

field profiles are shown in figure 3.4. This particular cavity geometry was designed to maximize the Q of the Y dipole mode at the expense of the X dipole mode. Finite-difference time-domain simulations were used to characterize the Q of this mode as a function of the hole/cladding (ambient) refractive index. The simulations were performed with a spatial resolution of 25 points per lattice period. To simulate the Q , a Gaussian electromagnetic pulse was used to excite the cavity. The field was then evolved through time and the data filtered for the frequency corresponding to the mode of interest and the rate of energy decay within the cavity calculated. The simulated Q versus ambient refractive index is shown in figure 3.5. Even though the Q is initially over 25,000 with an ambient refractive index of 1.0 (corresponding to air), the Q quickly drops to approximately 2,000 as the ambient refractive index increases to 1.5, an approximate value for the refractive index of LC.

After addressing the Q -dependent cavity design constraints, attention was directed towards maximizing the tunability of the laser. The PC laser was tuned by modulating the refractive index in the holes and cladding layers. Therefore to maximize tuning, the lasing mode should overlap these regions. The high- Q Y dipole mode of interest supported by the cavity design shown in figure 3.4 contains an electric field maximum in the central defect hole and also features evanescent fields which extend into both cladding layers. The considerable modal overlap with the hole and cladding regions provided sufficient opportunity for tuning the lasing wavelength by modulating the refractive index within these regions.

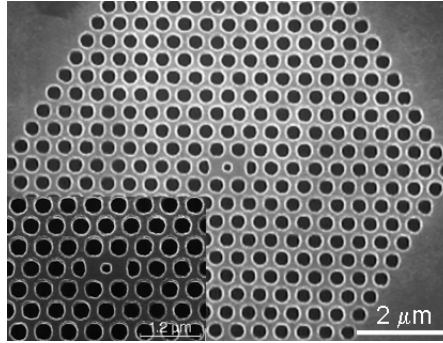


Figure 3.3: Scanning electron micrograph of fabricated PC laser cavity. The PC lattice periodicity, a , is 500 nm; the normalized hole radii are 0.33 (r/a); the normalized defect hole radius is 0.2 (r/a); and the half-ellipses have a normalized minor axis length of ~ 0.13 (r/a). (inset) Close-up of defect cavity.

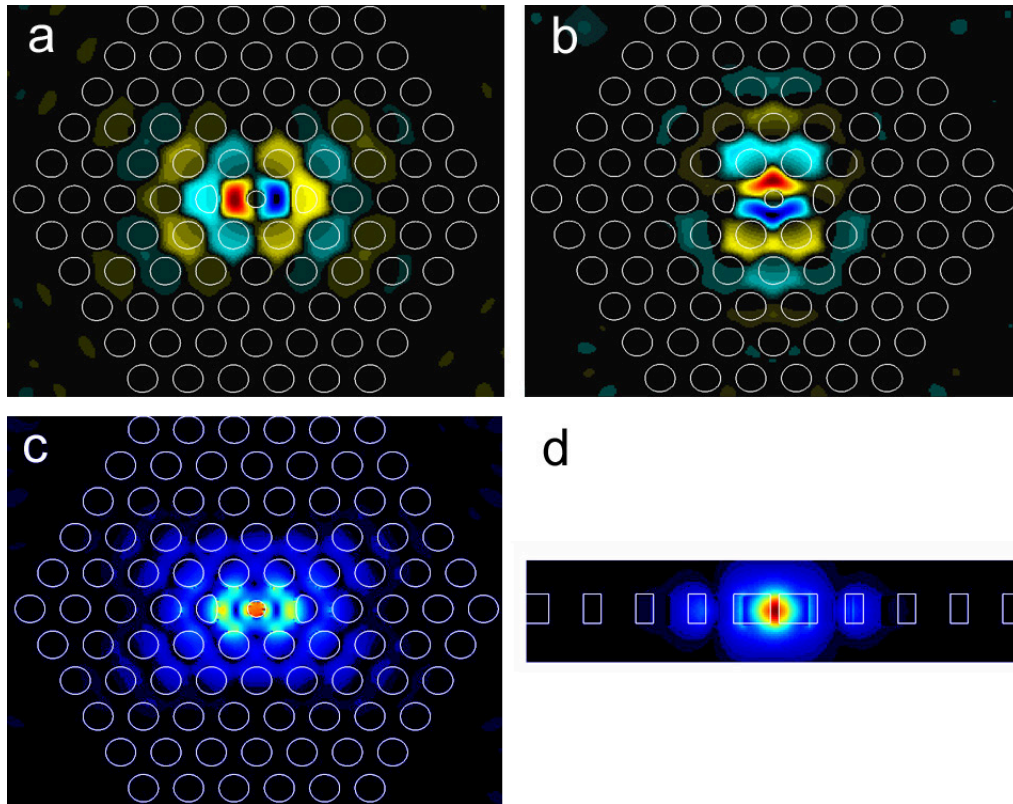


Figure 3.4: Simulated modal field profiles. Z (out-of-plane) component of magnetic field for high-Q Y dipole mode (a) and low-Q X dipole mode (b). (c) Electric field amplitude of Y dipole mode. (d) Cross-section view of electric field amplitude for Y dipole mode showing the evanescent fields extending into the cladding layers. The evanescent fields are important for tuning the cavity resonances because they enable tuning by changing the refractive index in the cladding regions.

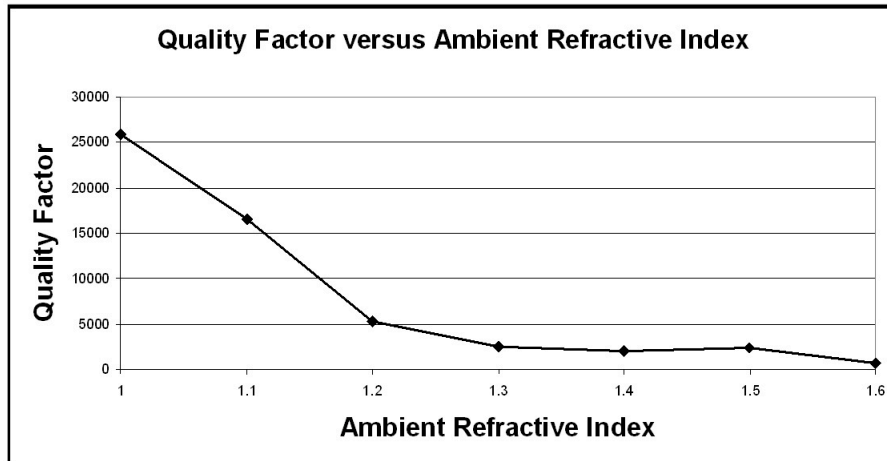


Figure 3.5: Finite-difference time-domain simulation of Y dipole mode Q as a function of ambient refractive index. Although the Q is above 25,000 at an ambient refractive index of 1.0, the Q plummets to approximately 2,000 at an ambient refractive index of 1.5. The simulations in conjunction with previously published PC laser work [66] suggest lasing is possible with this cavity design after LC infiltration.

Finite-difference time-domain simulations were used to estimate and quantify the lasing mode's sensitivity to the ambient refractive index. The results of these simulations are shown in figure 3.6. As expected, the photonic bandgap decreases with a reduction in PC/cladding refractive index contrast, and the cavity resonance red-shifts to longer wavelengths as the ambient refractive index increases. For the particular physical parameters used in the lasers presented in this work (lattice constant $a = 500$ nm, lasing wavelength $\lambda \approx 1.55$ μm , ambient refractive index ~ 1.5), the tuning rate is estimated to be approximately 210 nm per unit of ambient refractive index change.

3.3.2 Wafer Specifications and Sample Fabrication

The PC lasers were fabricated from a 330 nm thick slab of InGaAsP containing 4 compressively strained quantum wells optimized for emission at 1.55 μm . The precise wafer specifications are shown in table 3.1. A 130 nm thick layer of SiO₂ was grown on top of the wafer using plasma enhanced chemical vapor deposition (PECVD) and served as a hard etch mask for later etching steps. The next task was to define the PC pattern onto the wafer using e-beam lithography. Four percent 495 K polymethylmethacrylate (PMMA) e-beam resist was spun at 3000 RPM for 1

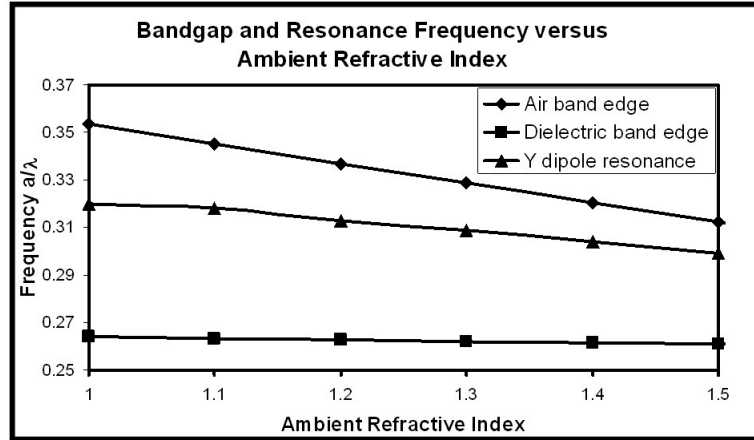


Figure 3.6: Simulation of dielectric band, air band, and Y dipole resonance as a function of the ambient refractive index. As the ambient refractive index increases, the bandgap narrows and the resonance red-shifts. For the lasers we use ($a = 500$ nm), the tuning rate of the resonance is approximately 210 nm per unit of ambient refractive index change.

minute and then baked at 170°C for 15 minutes. The resist was exposed using a Leica EBPG 5000+ e-beam writer at 100 keV with doses ranging from $800 \mu\text{C}/\text{cm}^2$ - $1200 \mu\text{C}/\text{cm}^2$. After exposure, the resist was developed for 1 minute using a solution of 1:3 MIBK:IPA (methyl isobutyl ketone:isopropanol alcohol). Next, a reactive ion etch (RIE) was used to transfer the pattern into the oxide mask using 20 sccm at 40 mTorr of CHF_3 and 90 W for 3 minutes 45 seconds. The pattern was then transferred into the wafer using an inductively coupled plasma reactive ion etch (ICPRIE) with 30 sccm HI , 10 sccm H_2 , and 3 sccm Ar at 100 W forward power, 850 W ICP power, 10 mTorr chamber pressure, and 12 mTorr strike pressure, cooled with 20°C water for 1 minute 20 seconds. Next, the sample was immersed in HF to remove the oxide mask and any residual PMMA. Lastly, the quantum well slab was undercut by immersing the sample in a 4:1 $\text{HCl}:\text{H}_2\text{O}$ (37% hydrochloric acid:water) solution at 0°C for approximately 7 minutes, or until the membrane was sufficiently undercut. Considering HCl preferentially attacked InP along particular crystal planes, proper etch guides were designed to ensure complete undercutting with this final etch step. The end result was a suspended quantum well membrane patterned with PCs. A schematic of the fabrication procedure is shown in figure 3.8.

Layer	Composition	Description	Bandgap	Comments	Thickness (nm)
1	InP	Cap			50
2	InGaAsP	Electron confinement	$E_g=1.22 \mu\text{m}$		117
3	InGaAsP	Quantum well	$E_g=1.55 \mu\text{m}$	85% compressive strain	9
4	InGaAsP	Electron confinement	$E_g=1.22 \mu\text{m}$		20
5	InGaAsP	Quantum well	$E_g=1.55 \mu\text{m}$	85% compressive strain	9
6	InGaAsP	Electron confinement	$E_g=1.22 \mu\text{m}$		20
7	InGaAsP	Quantum well	$E_g=1.55 \mu\text{m}$	85% compressive strain	9
8	InGaAsP	Electron confinement	$E_g=1.22 \mu\text{m}$		20
9	InGaAsP	Quantum well	$E_g=1.55 \mu\text{m}$	85% compressive strain	9
10	InGaAsP	Electron confinement	$E_g=1.22 \mu\text{m}$		117
11	InP	Sacrificial layer			1000
12	InGaAs	HCl etch stop			20
13	InP	Substrate			
Total InGaAsP thickness					330

Table 3.1: InGaAsP wafer specifications. The active region is comprised of 4 quantum wells optimized for emission at $1.55 \mu\text{m}$. The quantum wells are compressively strained to favor coupling to the PC cavity's TE modes and are centered within the 330 nm thick slab.

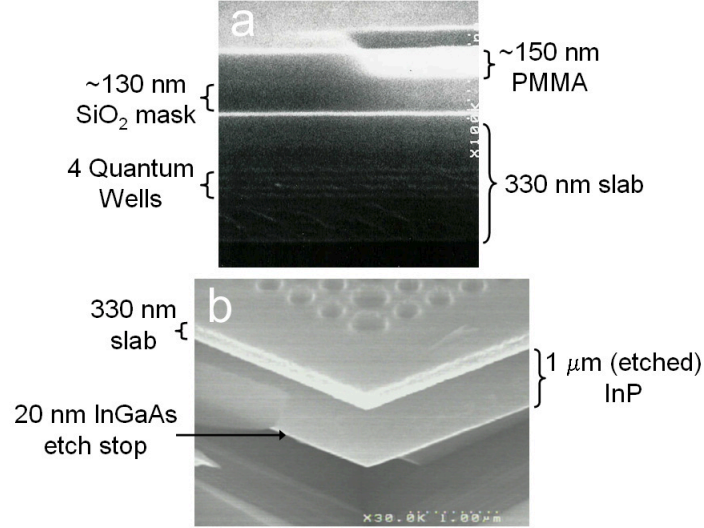


Figure 3.7: Scanning electron micrographs showing wafer composition. (a) This cross-section image is taken after e-beam lithography processing, but before any etching steps. The various layers (including the 4 quantum wells) comprising the wafer can be discerned in the image. (b) This image is of a fully processed sample and shows the removal of the 1 μm InP layer (for optical isolation purposes) and the suspended thin InGaAs etch stop layer (the layer was penetrated during the HI dry etch step under the PC etch guides and enabled the undercutting of the layer during the HCl wet etch step (see figure 3.8)).

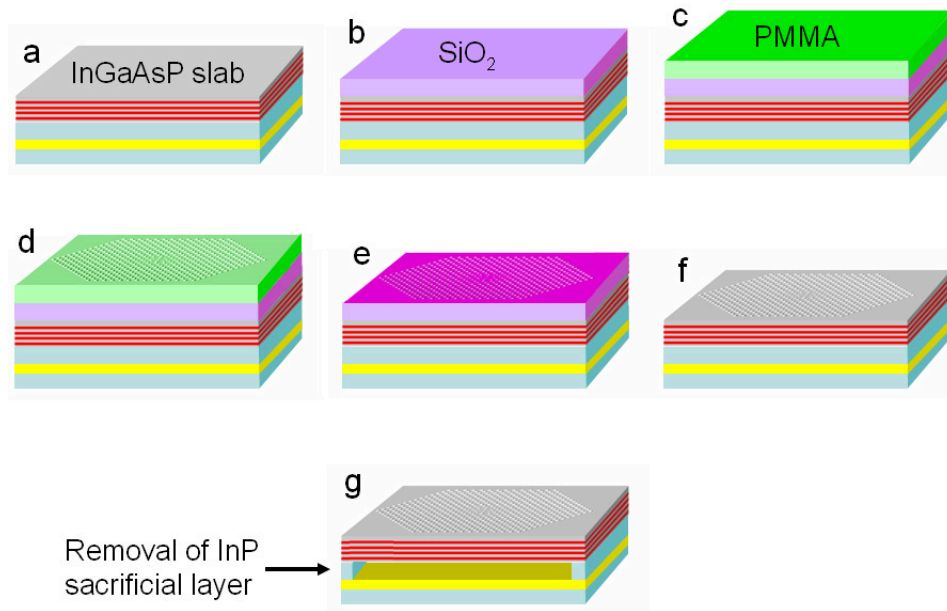


Figure 3.8: Schematic of fabrication procedure for InGaAsP quantum well PC lasers. (a) The original wafer before any processing. (b) First, a 130 nm SiO_2 hard mask is deposited on the wafer using PECVD. (c) Next, PMMA is spun on the sample in preparation for the subsequent e-beam lithography steps. (d) The PMMA is exposed with the PC pattern and is completely transferred into the PMMA after developing the exposed resist. (e) Next, the pattern is transferred into the SiO_2 hard mask via a CHF_3 RIE etch. (f) The pattern is then transferred into the quantum well slab with a HI-based ICPRIE etch. Lastly, the slab is undercut by dissolving the InP sacrificial layer beneath the slab with a HCl wet etch.

3.4 Integration of PCs with LC

Now we discuss some of the issues and considerations involved with integrating PCs with LC. We begin by describing the relevant LC parameters that must be considered and the inherent tradeoff between a LC infiltrated PC cavity's tunability and its Q. We then discuss the process of fabricating a LC cell around the PC lasers. Lastly, we highlight some aspects of LC behavior which impact the tuning characteristics of PC cavities. In particular, we focus our attention on domain formation and the confinement effects LC experiences when infiltrated into the small holes of a PC.

3.4.1 Liquid Crystal Parameters

As mentioned previously, infiltrating the PC with LC decreases the slab/cladding refractive index contrast and decreases the cavity mode's vertical confinement, lowering its Q. Moreover, the LC can introduce further losses due to scattering if it is not uniformly aligned [31], especially within the holes of the PC. To mitigate these deleterious effects, a LC featuring the lowest refractive indices and smallest birefringence should be used. Fortunately, the birefringence of LCs tends to decrease as the refractive indices decrease, and so both desirable qualities can simultaneously be realized. Unfortunately, as with the cavity design criteria the LC selection involves a tradeoff between Q and tunability. Both the lower refractive index, which causes the lasing mode field to penetrate less into the cladding, and the smaller birefringence, which decreases the possible refractive index modulation, reduce the tuning range of the laser. For this work we chose a common LC (MLC-6815 from Merck) with a low refractive index ($n_e = 1.519$, $n_o = 1.467$ at 589 nm) and a modest birefringence (0.05 at 589 nm) to maximize the cavity Q while still obtaining a detectable lasing resonance shift. In the future, as cavity designs and fabrication methods improve, LCs with a larger birefringence can potentially be used to increase the tuning range of the PC lasers.

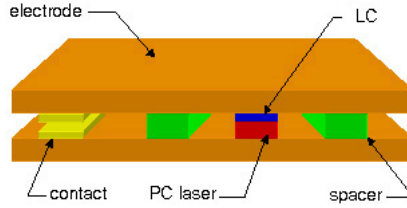


Figure 3.9: Cross-section of LC cell constructed around PC lasers. The LC comprising the top cladding layer is estimated to be approximately $15\ \mu\text{m}$.

3.4.2 Liquid Crystal Cell Fabrication

To construct an LC cell around the PC lasers, the PC sample was first glued along with two spacers to a transparent conducting indium tin oxide (ITO) glass plate that served as the bottom cell electrode. A drop of LC was then placed onto the PC sample. A second ITO plate was glued to the spacers, and the resulting gap between the top ITO plate and the PC sample was approximately $15\ \mu\text{m}$. The ITO plates were chosen to minimize absorption at $1.55\ \mu\text{m}$ and feature 92% transmission at that wavelength. The LC cell was then heated above the LC's clearing point (67°C) on a hotplate at 90°C for 5 minutes which helped ensure complete infiltration into the PC. It should be noted that this heating step is now believed to be superfluous for the LC infiltration. Without exception, excluding the heating step seemed to make no difference in the degree of infiltration.² This implies the capillary-like forces present within the PC holes are sufficient to completely draw the LC into the structure. After heating, wires were attached to the ITO plates with conducting tape which were then connected to a power supply. A schematic of a completed cell is shown in figure 3.9.

3.4.3 Liquid Crystal Domain Formation

In the absence of an alignment layer, the LC is not uniformly aligned, meaning the directors exhibit orientational fluctuations. These director fluctuations lead to domain-like behavior in the LC [84]. For short (micron) length scales, the LC is predominantly aligned in a given direction, but for longer length scales no correlation exists between the orientations of disparate regions.³ Even in the presence of an alignment layer,

²This step was excluded in the experiments discussed in the next chapter.

³The LC is believed to be primarily oriented homogeneously though, and so the lack of an orientation correlation for longer length scales means LC in disparate regions are rotated with respect to each other but are all still oriented in the plane of the PC.

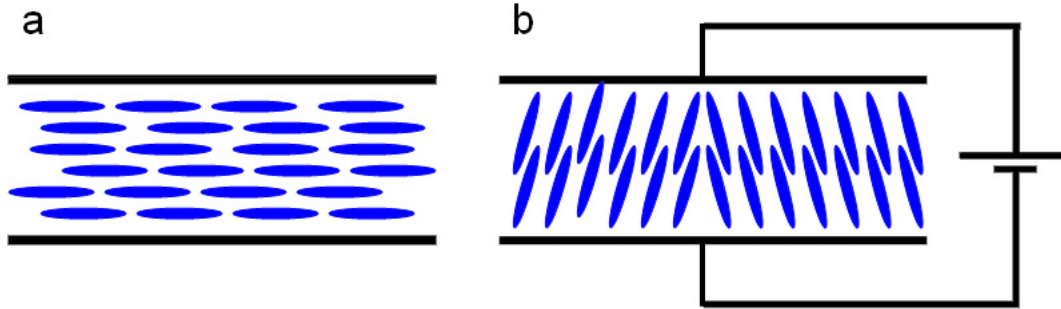


Figure 3.10: Schematic showing origin of domain wall formation. (a) With no voltage applied across a standard LC cell, the LC is aligned parallel to the plates. (b) When a voltage is applied across the cell that is above the threshold voltage, the LC reorients and aligns in the direction of the field. For voltages below saturation the LC is not perfectly aligned to the field and multiple orientation possibilities exist for the LC that are energetically equivalent. The interface between these different orientations forms a domain wall which separates the two regions. These domain walls can be seen using PIM and appear as bright lines in the images.

domains can still form in the LC. Take for instance the standard LC cell configuration shown in figure 3.10 (a). The LC is aligned parallel to the plates and an applied field is oriented perpendicular to this orientation. As the voltage is increased above the Fredericksz transition threshold, the LC begins to tilt and align parallel to the field. From a free energy standpoint, however, multiple equivalent possibilities exist for the LC to do this, and two of them are shown in figure 3.10 (b). The intersection of these two orientations forms a wall, separating the two domains. These domain walls can be observed using PIM (see figure 3.11), and the shape of the domain wall can be used to quantitatively determine physical properties (e.g., ratios of elastic constants) of the LC [31].

3.4.4 Confined Geometry Effects

The behavior of LC in confined geometries is of obvious relevance when infiltrating LC in PC holes. The two most important issues of concern are the prevalent orientations that exist within the holes and the impact the confined hole geometry has on controlling the LC orientation. The LC community has investigated these issues in part by studying the behavior of LC in small cylindrical pores. Two systems which have been used for the studies are Nucleopore and Anopore membranes [85]. Nucleopore membranes are 10 μm thick polymer membranes that have cylindrical channels



Figure 3.11: Polarization interference microscopy image of LC domains. The bright lines are the domain walls formed by LC aligning differently in response to an applied electric field as in figure 3.10

penetrating through them with radii ranging from 30 nm to 12 μm . Anopore membranes can be thicker, but the pore diameters are limited to 200 nm (which happens to be the approximate diameter for our PC cavity defect holes).

Nuclear magnetic resonance (NMR) techniques are used to determine the stable LC orientations within the pores. The orientations which have been found to exist include the escaped radial with point defects, planar-polar, escaped-twisted, planar-bipolar, parallel axial, tilted axial, and twisted bipolar [85]. Several of the more common configurations are shown in figure 3.12. The factors which determine the lowest free energy configuration and, hence, LC orientation are the hole size, the surface texture, LC interaction with the hole's inner surface, and the temperature (for thermotropic LCs). Although chemical affinities may exist between LC and some materials which can influence an LC's orientation, usually the orientation is determined by the physical inner wall geometry. The inner walls of the PC holes are dependent upon the etch characteristics and so may vary from one sample, or even one hole, to another. A possible scenario is that the etch process leaves nanometer-scale striations parallel to the hole axis, which favors a parallel axial LC orientation. Unfortunately, the NMR technique used to investigate LC orientations within holes requires extremely long holes and, as such, is not compatible with PC laser samples. The short aspect ratio of the PC holes (length to diameter ratio is close to one) raises another concern. The

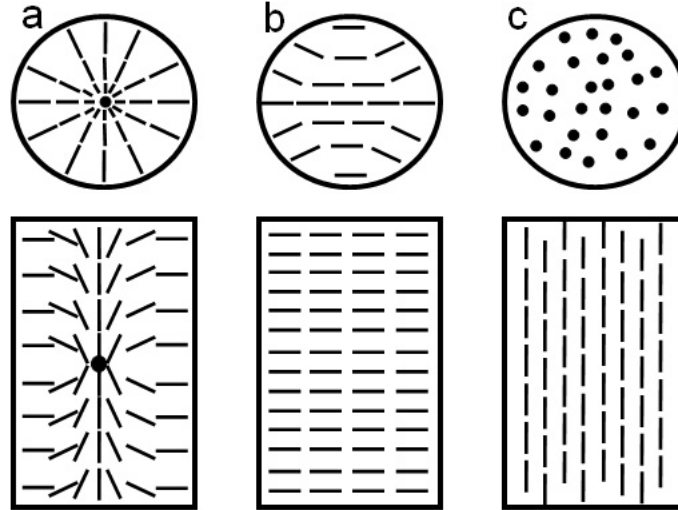


Figure 3.12: Schematic of three LC configurations commonly found in small cylindrical holes. Top and cross-section views are provided for (a) escaped radial with point defect, (b) planar-polar, and (c) parallel axial configurations.

configurations shown in figure 3.12 are found in extremely long-essentially infinitely long holes. In comparison, the PC holes are short, and so the LC configuration is likely to be a hybrid between one of the idealized hole configurations and the cladding layer configurations.

Another aspect of the confinement effects (experienced by the LC infiltrated within the PC holes) of concern is the extent to which the orientation can be actively controlled with electric fields. Earlier in the chapter we discussed the role surface anchoring plays in parallel plate LC cells. Specifically, surface anchoring inhibits alignment of LC within a characteristic length of the surface. To determine an LC's characteristic length for a given surface, one needs to know the LC's elastic modulus and the surface anchoring energy. Unfortunately we know neither of these. We can, however, make conservative estimates using data compiled for other LC systems [33]. By doing so, a conservative lower bound of 100 nm is reached for a characteristic length. In other words, the characteristic length is at least as large as the radius of our PC cavity defect hole. Consequently, we expect the surface anchoring induced orientation within the PC defect holes to be largely unaffected by the applied electric field. This is unfortunate because it significantly reduces the tunability of our lasers.

3.5 Electrical Tuning of LC Infiltrated PC Lasers

We now discuss our efforts in successfully tuning PC lasers with infiltrated LC. We begin by describing the experimental setup and procedures used to characterize the lasers as well as the LC. Polarization interference microscopy is used again to provide valuable insight into the orientational behavior of the LC both with and without an applied electric field. Next the results of the electrical tuning of the PC lasers are presented and analyzed. The section concludes with a discussion of the effects of LC domain orientation and surface anchoring on the tuning characteristics of the lasers.

3.5.1 Experimental Setup and Procedures

Samples were measured using a micro-photoluminescence (μ PL) setup similar to the one shown in figure 3.13. The samples were pumped with 10 mW peak power using an 830 nm laser diode with a pulse length of 15 ns and a periodicity of 1.5 μ s. Pump light was focused onto the sample using a 100x microscope objective lens. The emitted light from the cavities was then collected through the same objective lens and directed into an optical spectrum analyzer (OSA) for recording of spectra. A polarizer was also occasionally inserted in front of the OSA to test the polarization properties of the emitted light. Spectra were acquired while adjusting the voltage applied across the LC cell. These spectra were then analyzed to determine the tuning characteristics of the lasers.

We initially encountered significant difficulties achieving lasing with the PC cavities after infiltrating them with LC. This is understandable given that the infiltrated cavities' simulated Qs are approximately 2,000. This roughly coincides with the Qs of the first comparable PC lasers ever reported [66]. The early testing results were discouraging and we investigated the feasibility of creating customized LC mixtures or even diluting LC mixtures in an effort to decrease the overall refractive index and boost the cavities' Qs. Eventually, however, we were able to achieve lasing in our PC samples and these efforts were abandoned. Before obtaining lasing, though, we made a critical alteration to our testing procedure. The change was made to guarantee that a potentially legitimate PC sample would not be prematurely eliminated from

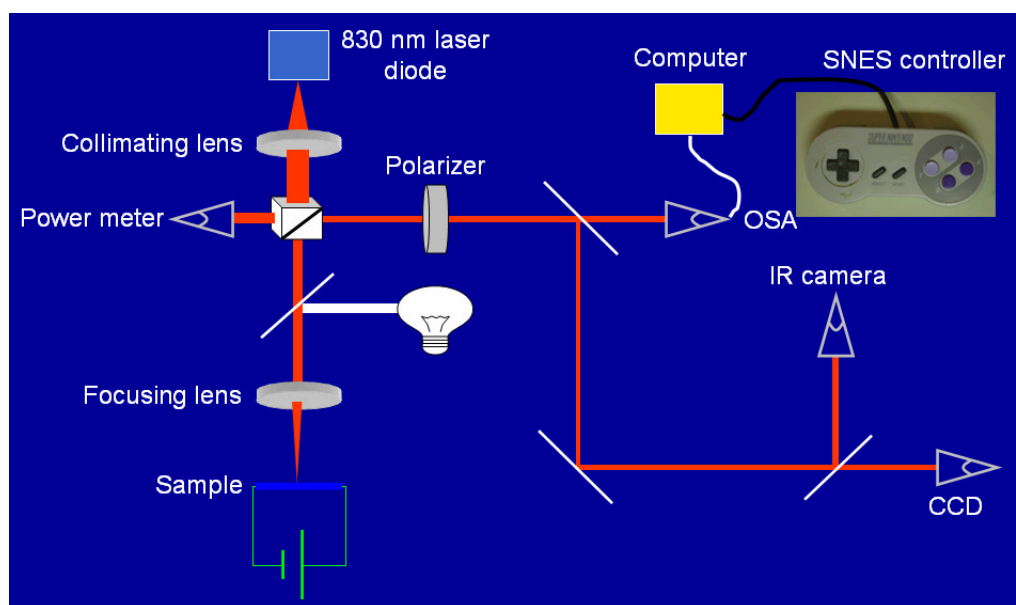


Figure 3.13: Schematic of μ PL setup used to characterize PC lasers. Light from an 830 nm laser diode was focused onto the PC sample with a 100x objective lens. Emitted (or reflected pump) laser light was collected by the same objective lens and was either sent to an OSA to record the spectra, into a CCD for imaging, or into an IR camera to view the modal profiles. A removable polarizer could be inserted in front of the OSA to measure the polarization of the light emitted by the PC laser. A computer running LabView was used to store the spectra recorded by the OSA and was integrated with a Super NintendoTM controller which was used to trigger the spectra acquisitions. A picture of a slightly modified version of the setup can be seen in the next chapter in figure 4.18.

consideration. The original testing algorithm first characterized the lasers before infiltration and then tested them again after infiltration, devoting more attention to the best lasers from the first round of testing. Although quick, this procedure was susceptible to eliminating perfectly good lasers for a couple of reasons. First, if a cavity was barely of sufficient quality to lase, then the pumping conditions needed to be nearly ideal to achieve lasing. Given the number of pump parameters (e.g., pump location, period, width, power, and spot size), finding these ideal pump conditions was time consuming and impractical to thoroughly investigate for all devices. The original testing algorithm was inadequate in identifying the best cavities, which should warrant most thorough testing. This inadequacy resulted from the wavelength dependence of the quantum well gain spectrum (see figure 3.14) in conjunction with the significant red-shift of the resonant wavelengths that occurred due to LC infiltration (see figure 3.15). A cavity which seemed exceptionally good before infiltration may become horrible after infiltration because the cavity resonance started near the peak of the gain spectrum but shifted considerably past it after infiltration. The ideal cavity was one whose resonance shifted into the gain maximum *after* LC infiltration. To accommodate this reality the testing algorithm was modified as follows. First, all lasers were characterized before infiltration and again after infiltration with a 1.3 refractive index matched fluid. Based on these measurements, a subset of the cavities were tested after infiltration with a 1.4 refractive index fluid, and another subset was then tested after infiltration with a 1.45 refractive index fluid. The cavities were then infiltrated with the LC and the best cavities thoroughly tested with much effort expended on optimizing pump conditions.

Lasing of the PC cavities after LC infiltration was confirmed by recording characteristic input power-output power (L-L) curves as shown in figure 3.16. The measured peak threshold power of approximately 5 mW for the LC infiltrated cavity is significantly higher than thresholds from similar cavities without LC infiltration [86]. The higher threshold after infiltration is attributed to increased losses primarily from the decreased vertical confinement. Further losses were introduced by reflection and absorption of the pump laser by the ITO plate, scattering of the lasing mode's light from nonuniformly aligned LC, and by the LC coupling, through polarization rota-

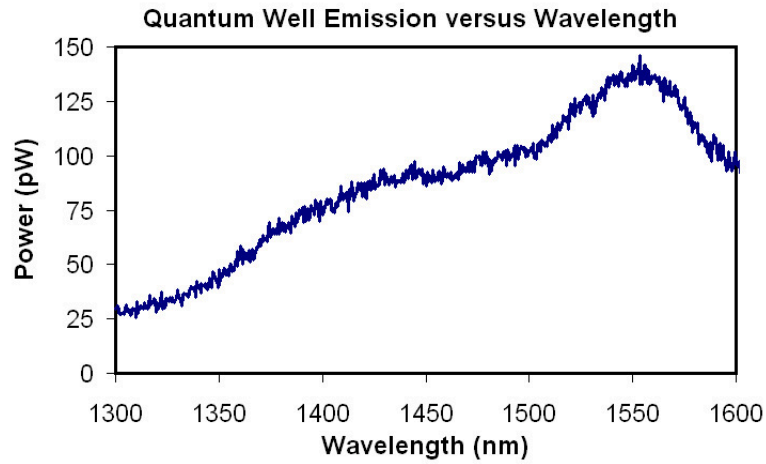


Figure 3.14: Emission spectrum from unprocessed InGaAsP material. The emission is a maximum at 1550 nm, the desired engineered maximum.

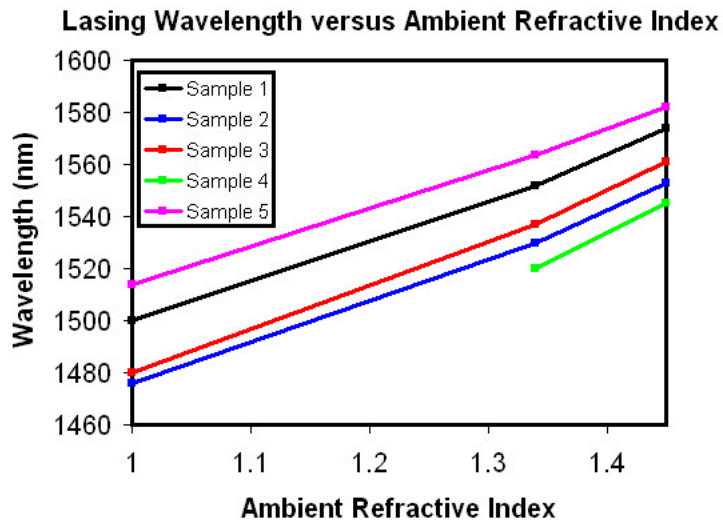


Figure 3.15: Experimental demonstration of PC laser tuning with liquid infiltration. Lasing wavelengths are recorded for several samples after infiltrating with index-matched fluids. The resonant wavelengths red-shift approximately 80 nm after being infiltrated with a 1.45 refractive index liquid. This shift is in good agreement with simulations which predict a shift of about 90 nm and is also roughly the resonance shift expected due to infiltrating the cavities with the LC.

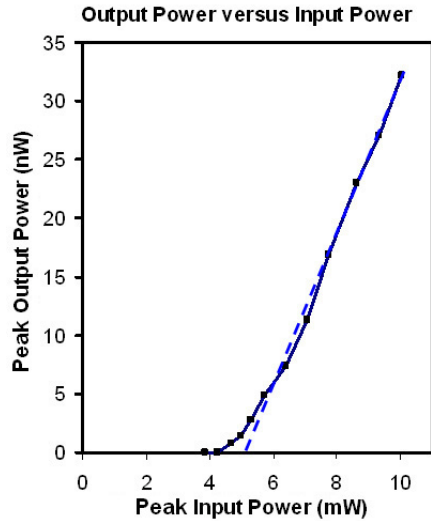


Figure 3.16: L-L curve of laser infiltrated with LC. The lasers were pumped with 30 ns pulses and 3 μ s periodicity. The laser peak threshold power is estimated to be approximately 5 mW. The relatively high threshold is primarily attributed to the increased losses associated with the LC infiltration.

tion, photons out of the TE-polarized lasing mode.

3.5.2 Liquid Crystal Characterization

The refractive indices of the LC used in this work are only specified at the LC industry standard 589 nm and not at the relevant wavelengths of 1.55 μ m. To characterize the LC at infrared wavelengths, we infiltrated PC lasers with the LC and compare the resonance shifts to the shifts obtained by infiltrating the same cavities with index-matched fluids. Within this method's resolution, the experiments indicated the LC's refractive indices, and by extension the birefringence, to be the same at 1.55 μ m as at visible wavelengths. Therefore, in the analysis which follows we assume the LC's refractive indices and birefringence at 1.55 μ m to be those specified at 589 nm. The uncertainty of this method is dominated by the fact the LC orientation in the PC is not known. In theory the ambient refractive index experienced by a cavity mode due to the LC can range anywhere from n_o (director everywhere orthogonal to polarization axis of mode) to n_e (director parallel to polarization axis), but most likely the surface anchoring-governed LC orientation yields an effective ambient refractive index far from either extreme.

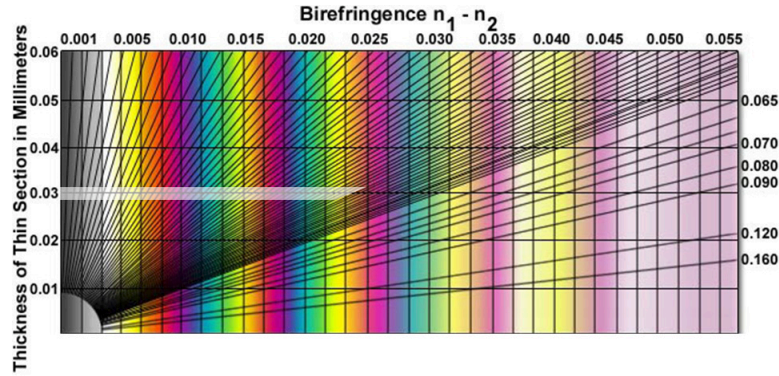


Figure 3.17: Michel-Levy chart showing the color region accessible given the LC's birefringence (~ 0.05) and thickness ($\sim 15.0 \mu\text{m}$), keeping in mind the PIM images are created by light traversing the LC cell twice.

3.5.3 Polarization Interference Microscopy Analysis of LC

Polarization interference microscopy was used to further characterize the LC and also proved to be a valuable tool in analyzing the laser tuning data (discussed below). Since we knew the LC's birefringence and its thickness ($\sim 15 \mu\text{m}$), PIM provided substantial information regarding the orientation of the bulk LC in the top cladding layer above the PC slab. By examining the PIM images prior to applying a voltage across the cell and referring to the Michel-Levy chart (see figure 3.17), we determined that the LC exhibited a homogeneous (planar) orientation (see figure 3.18 (a)). Secondly, the LC spontaneously formed domain-like features with length scales commonly exceeding a few tens of microns (see figure 3.18 (b)). Rotation of the sample with PIM revealed these in-plane domain-like structures were rotated with respect to each other.

Polarization interference microscopy provided further insights into the LC behavior during voltage modulation. The PIM images were studied to infer information regarding the LC behavior as a function of the voltage applied across the cell. The existence of a Fredericksz transition can clearly be observed with an abrupt and dramatic change in the image. At threshold, the colorful image became mostly black, which was expected given that the LC was now oriented vertically and parallel to the electric field (see figure 3.19 and external movie file *EtunedPCPIMmovie1.mov*). By recording PIM images while slowly ramping the voltage, the threshold voltage was determined to be approximately 4 V, larger than the specified AC threshold voltage

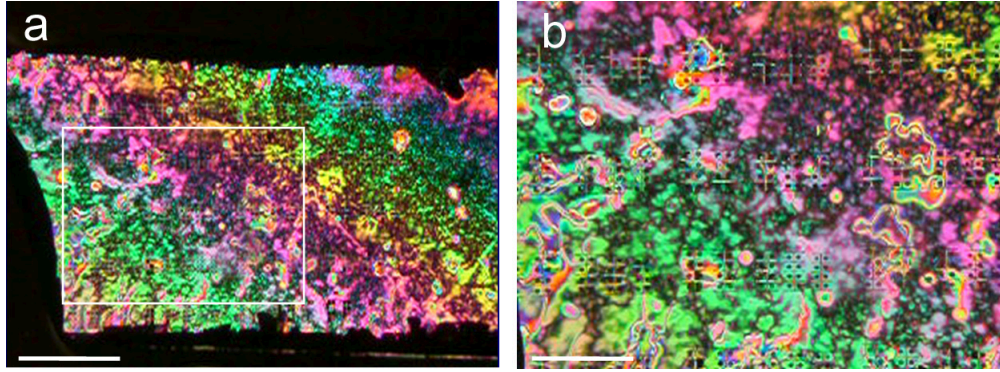


Figure 3.18: Polarization interference microscopy images showing LC planar orientation and domain-like features. (a) By referring to the Michel-Levy chart in figure 3.17 we see the bulk LC is predominantly homogeneously aligned. The gradient in color is attributed to a gradient in cell thickness caused by the ITO top electrode plate not being parallel to the PC substrate. The cells are normally fabricated with the top plate parallel to the PC substrate. Scale bar is $500 \mu\text{m}$. (b) A close-up of part (a) denoted by the white box. In this image the domain-like structures are more clearly seen and the hexagonal PC samples can be seen as well. The LC forms well-aligned regions that are rotated with respect to each other, causing variations in the brightness of the image but not in color (the variations in color are due to variations in the degree of in-plane alignment). Scale bar is $250 \mu\text{m}$.

of 2.3 V. The discrepancy may have been due to charging effects resulting from our DC modulation.⁴ As the voltage was increased beyond threshold, the LC increasingly aligns itself parallel to the field and normal to the PC sample. By increasing the voltage until negligible further alignment was observed in the bulk LC, the saturation voltage was estimated to be approximately 8 V.

Polarization interference microscopy also revealed the existence and behavior of LC domains above threshold. As the voltage was ramped above the Freedericksz transition, the numerous small domains quickly merged and collapsed into a few large domains. The remaining domain walls can be seen as white lines in the PIM images, and further consolidation can be induced and accelerated by increasing the voltage across the cell (see figure 3.20 and external movie file *EtunedPCPIMmovie2.mov*). During repeated cycling of the voltage between zero and saturation, the PIM interference pattern always returned to the same configuration, suggesting the LC exhibited surface alignment memory resulting from surface anchoring (see figure 3.21 and external movie file *EtunedPCPIMmovie3.mov*). Even though the bulk LC changed

⁴The LC industry normally uses AC modulation to increase the longevity of the devices and to minimize impurity and charging effects which can compromise the device performance. These effects may explain the slightly higher than expected threshold voltage.

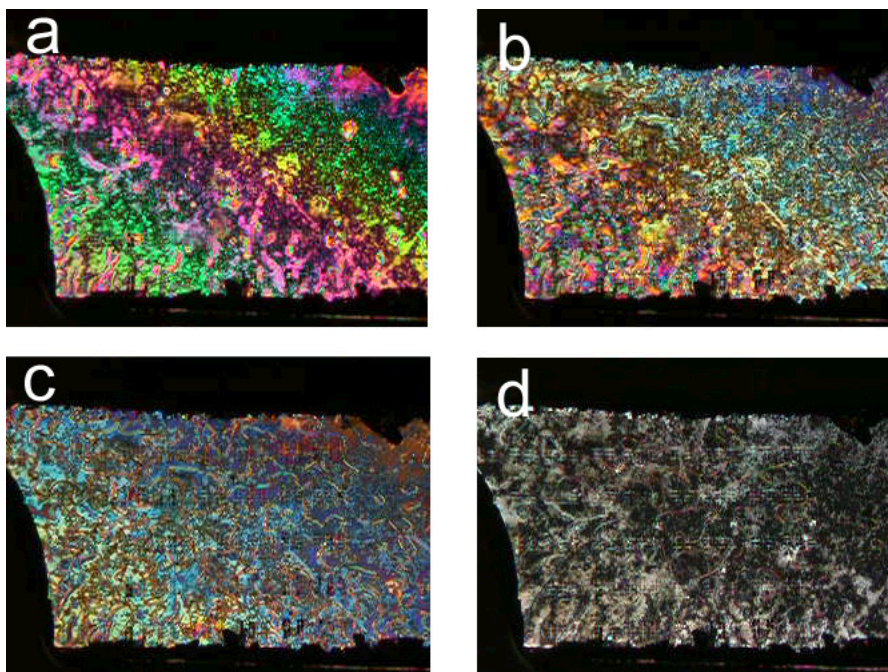


Figure 3.19: Sequence of PIM images showing LC undergoing Freedericksz transition. The voltage applied across the cell is slowly ramped from 0 V (a), through the threshold voltage (b) and (c), and up to 20 V (d). The threshold voltage is determined using this method and is approximately 4 V. As the voltage is increased toward saturation, the LC continues to align parallel to the electric field and causes the PIM image to become black.

orientation throughout the cycling, the LC near the surfaces remained anchored. The bulk LC orientation appeared to be determined by the orientation at the surfaces. The surface anchoring locked the orientation of the LC near the surfaces into a stable configuration which then propagated through the bulk LC in the cell.

One drawback to the PIM technique is that it only reveals information about the bulk LC orientation and, as such, does not provide conclusive evidence of the orientation in the vicinity of the PC slab. The PIM images are unable to distinguish whether or not the bulk LC orientation is due to the anchored LC at the PC surface, electrode surface, or both. With that said, however, the planar geometries of the PC slab and the ITO plate favored a homogeneous LC orientation and the PIM data suggest that neither surface was anchored vertically (homeotropically). Therefore, with a high degree of confidence the LC is believed to be primarily oriented homogeneously in the vicinity of the PC slab. The tuning data presented later in the chapter also supports this hypothesis. The presumed homogeneous alignment is the desired

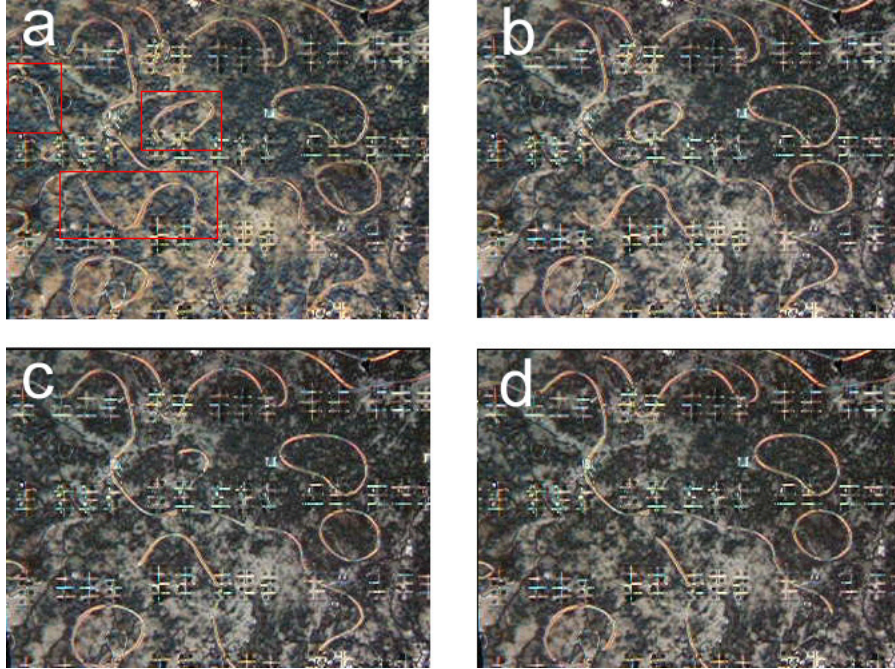


Figure 3.20: Sequence of PIM images showing LC domain consolidation. All images are taken at voltages above the Fredericksz transition. Consolidation of domains is indicated by disappearing domain walls (bright lines). The red boxes in (a) highlight domain walls which are in the process of disappearing in the sequence of images (a)-(d).

alignment for our tuning experiments and is the reason why an alignment layer was not used. We originally investigated using a rubbed polyimide layer to induce a homogeneous LC orientation but discontinued these efforts after observing that the LC tended to automatically possess this orientation after the cell fabrication.

3.5.4 Electrical Tuning Results

During the optical pumping of the PC cavities, the LC was reoriented and the lasers were tuned by application of an electrostatic field between the top ITO electrode and the InP wafer substrate. The tuning range strongly depends on the LC's refractive indices and the birefringence at the lasing wavelength ($\sim 1.55 \mu\text{m}$), the zero-field LC orientation, the overlap between the lasing mode and the LC, and the electric field pattern generated by the electrodes. For the sake of establishing a baseline for the laser tuning range, the LC is assumed to have a spontaneous random orientation. The influence of the applied voltage on the LC orientation is modeled using electrostatic simulations of the generated electric field patterns (see figure 3.22). These simulations

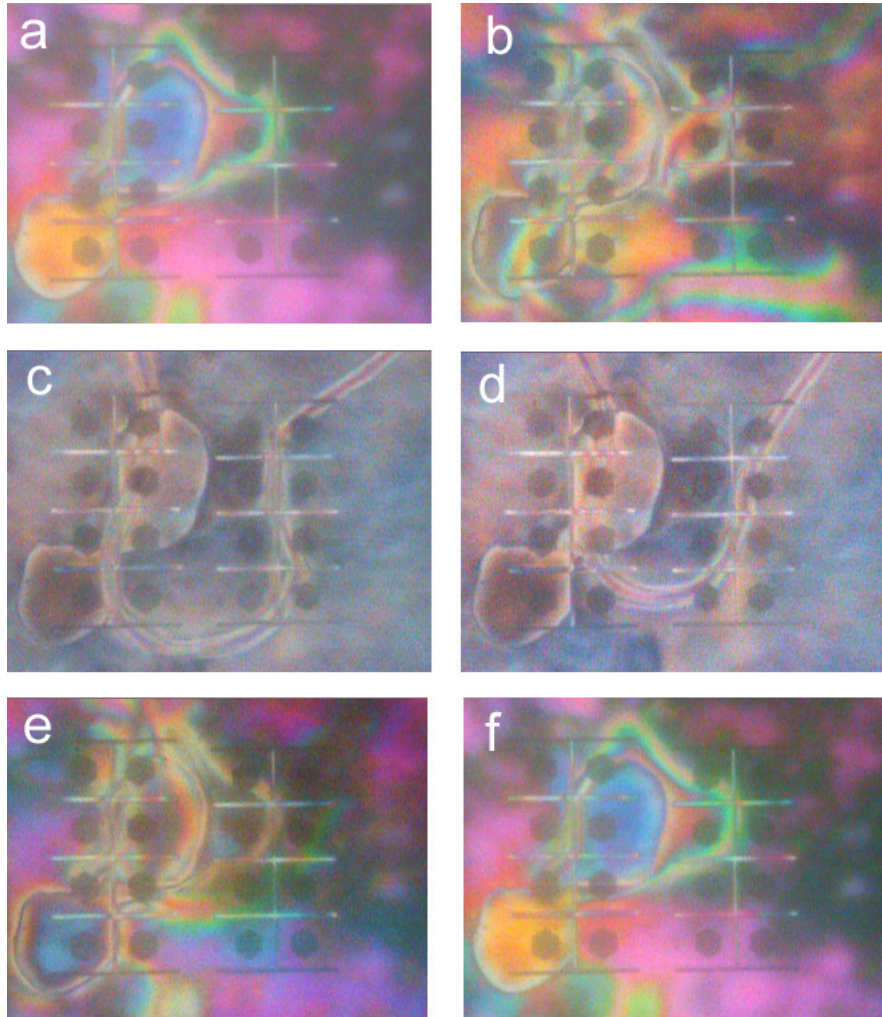


Figure 3.21: Sequence of PIM images showing LC surface alignment memory. (a) This image shows the initial LC orientation with no voltage applied across the cell. (b) This image is taken as the voltage is ramped through the Fredericksz transition. (c)-(d) These images are taken when the LC is aligned vertically with 20 V applied across the cell. A domain wall can be seen moving across the PC samples. (e) This image is taken as the voltage is ramped down through the Fredericksz transition. (f) This image is taken with no voltage applied across the cell. The beginning and ending LC orientations appear to be identical. The LC at the surfaces is believed to be anchored and dictates the orientation of the bulk LC in the cell.

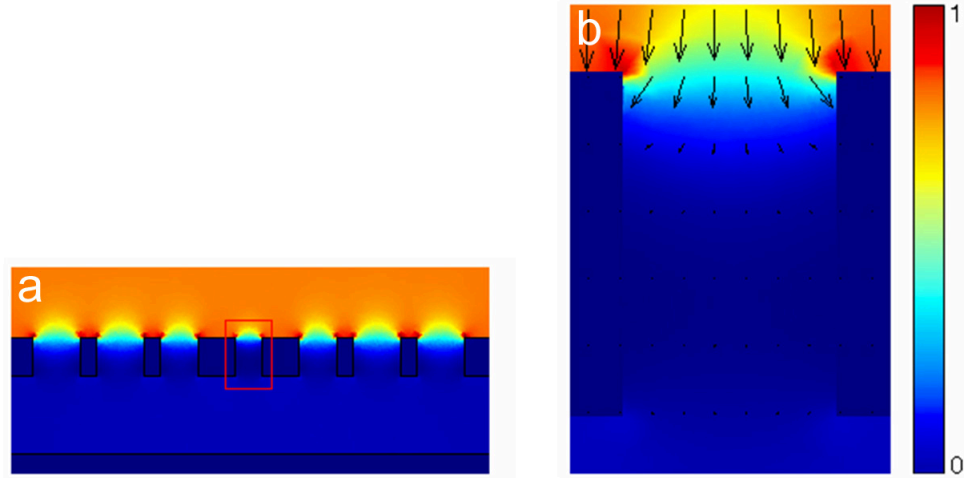


Figure 3.22: Finite element simulation of electric field around PC slab generated by the ITO electrodes. Electric field magnitudes are represented by a normalized color scale from 0 to 1, and arrow direction and length denote field direction and amplitude, respectively. (a) Cross-section of the PC membrane slab. The electric field is screened from the PC holes due to the doped semiconductor slab. (b) Close-up of field in central defect hole denoted by red box in part (a). The simulation suggests the electric field does not penetrate appreciably into the defect hole. The screening of the electric field may significantly impair the ability to tune the lasers by prohibiting the controlled alignment of the LC within the PC holes.

indicate the LC in the top cladding layer can be aligned vertically, but the electric field is sharply damped in the holes of the PC due to the screening by the conducting PC membrane. Fortunately, the lasing mode features an evanescent field which extends into the cladding layers and is influenced by the refractive index in these regions. Therefore, changing the refractive index in the top cladding layer can achieve tuning of the laser.

To demonstrate LC tuning of the PC lasers we recorded lasing spectra as a function of the gate voltage applied across the cell. The electrostatic simulations predict the LC in the top cladding should align vertically to the surface, lowering the refractive index from ~ 1.485 to ~ 1.467 and blue-shifting the lasing wavelength. Such a blue-shift was observed upon ramping the gate voltage from 0 to 20 V (see figure 3.23). The tuning starts at approximately 4 V, in agreement with the observed threshold voltage using PIM, and signals the onset of the Fredericksz transition [87]. In figure 3.23 (a), a maximum blue-shift of approximately 1.2 nm is observed at 20 V but larger tuning ranges of nearly 2 nm were also obtained using similar device geometries. The magnitude of the tuning range suggests only the LC in the top cladding layer was

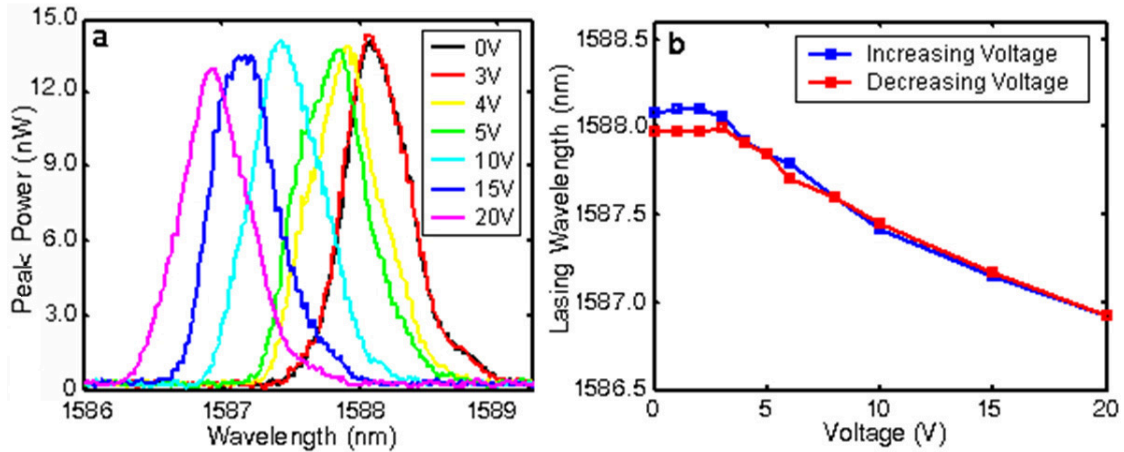


Figure 3.23: Demonstration of laser tuning via LC realignment. a) Laser spectra taken with an applied voltage ranging from 0-20 V across the LC cell. The threshold for tuning is approximately 4 V, coinciding with the measured LC threshold voltage using PIM (see figure 3.19). A maximum blue-shift of 1.2 nm is measured at 20 V. For clarity note lasing wavelength monotonically decreases with increasing voltage, with the 0 V trace being the far right and the 20 V trace being the far left. b) Lasing wavelength versus applied voltage for a voltage ramp cycle. Although the tuning rate lessens at higher voltage, the data suggest saturation is not even reached at 20 V and further tuning may be possible with stronger fields. The tuning is reversible but demonstrates a slight hysteresis at low fields which may be due to charging or impurity effects. The marker box height represents the upper bound of the uncertainty in the lasing wavelength obtained from the spectra.

being aligned to the field, a topic discussed further below. This tuning is independent of the DC field polarity. A slight hysteresis can be observed which may be attributed to charging and impurity effects in the LC (see figure 3.23 (b)).

3.5.5 Effect of LC Domain Orientation on PC Tuning Range

The PC cavity modes exhibit in-plane electric field components with the X and Y dipole-like modes primarily polarized along the X and Y directions, respectively. The effective refractive index experienced by the high-Q Y dipole mode due to the LC is dependent upon the orientation of the LC with respect to the mode's polarization axis as shown by equation 3.1.

If the LC spontaneously forms homogeneously oriented domains as the PIM data suggest, then equation 3.1 implies a variability of laser tuning range based upon the orientation of the domains with respect to the polarization axis of the lasing mode (see figure 3.24). The tuning range is dependent upon the effective refractive index difference from the zero-field state to the saturated state. The zero-field refractive

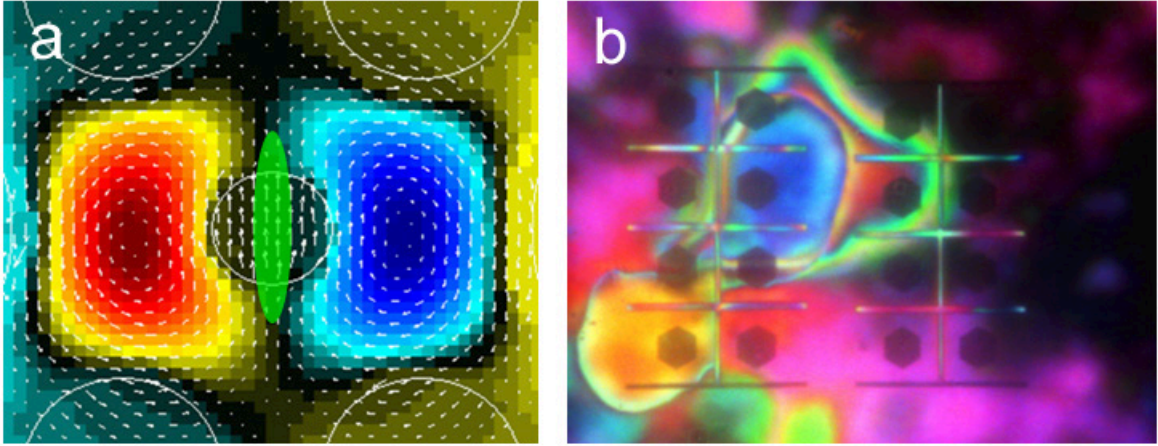


Figure 3.24: Illustration of PC laser tuning dependence on LC domain orientation. (a) Close-up of Y dipole mode showing polarization structure with superimposed hypothetical LC molecule. (b) Interference pattern captured using PIM showing the LC spontaneously forming domains above PC lasers (hexagons). The laser tuning ranges are partly dependent upon the zero-field LC orientation in the top cladding. Maximum tuning occurs when the LC is initially oriented such that its director is parallel to the mode's dominant polarization direction (shown in (a)). In this scenario the mode's top cladding refractive index modulation is essentially the maximum possible and ranges from n_e to n_o . As the LC zero-field orientation differs from the ideal case, the achievable tuning decreases and is a minimum when the LC's director is aligned orthogonal to the polarization axis.

index is a function of the domain orientation, but the saturated refractive index is always the same (n_o). Maximum tuning is thus expected when the refractive index is initially n_e and is then switched to n_o . This can occur when the LC domain is initially oriented such that the LC directors are aligned parallel to the mode's polarization axis. Conversely, minimum tuning is expected when the domain is initially aligned perpendicular to the mode's polarization axis. The observed distribution in tuning range data suggests that this is indeed the case.

3.5.6 Effect of Surface Anchoring on PC Tuning Behavior

The surface anchoring experienced by the LC at the ITO and PC slab interfaces locks the crystal into a stable configuration. One of the manifestations of the surface stabilization is that the LC exhibits surface alignment memory. Upon cycling the voltage between zero and saturation, the LC returns to its original configuration set by the boundary conditions (see figure 3.21). Both the tuning and PIM data indicate this reversibility is occurring. The stable configuration experienced by the nematic state can be destroyed, however, by heating the LC above its clearing point and

into the isotropic state. Upon cooling and condensing back into the nematic state, the LC settles into a different stable configuration. This is confirmed by measuring different tuning ranges for the same lasers after thermal cycling and also by observing a different PIM interference pattern of the bulk LC.

Beyond stabilizing the tuning behavior of the lasers, LC anchoring to the surface of the PC slab also inhibits their tuning range. The surface anchoring heavily influences the alignment dynamics of the LC in the vicinity of the PC membrane, where the lasing mode's evanescent field is strongest. The surface anchoring inhibits the LC from aligning along the electric field and thus decreases the tuning of the laser. The effects of the surface anchoring are the most pronounced for LC closest to the PC membrane. As the gate voltage is increased, LC molecules progressively closer to the PC membrane minimize their free energy by aligning along the electric field direction. This progressive alignment explains the continued tuning of the lasers even far above the saturation voltage (see figure 3.25). Although the surface anchoring reduces the overall tuning range, a benefit is that it enables the lasers to be continuously and precisely tuned over a range of wavelengths. Unlike other tuning methods such as lithographic tuning, LC tuning enables Angström or even sub-Angström precision in the control of the lasing wavelength.

Two outstanding questions that remain are the zero-field LC orientation and the degree of LC alignment in the PC holes. The electrostatic simulations indicate the field is screened from the holes, which limits the ability to control the alignment there. Of even greater importance, however, is the likelihood that the LC experiences anchoring to the inner walls of the holes. Liquid crystals have been studied in similar confined geometries and are found to experience relatively strong surface anchoring effects. The LC in these confined geometries can also feature homeotropic or escaped radial orientations among others [85, 88, 89]. As a result, even if the electric field had penetrated the PC holes, the LC might still not have aligned appreciably to the field, but remained stationary. Finite-difference time-domain simulations of the expected tuning range of the lasers support the premise that negligible alignment occurs within the PC holes and the alignment is confined to the top cladding layer. For example, simulations predict a blue-shift of 1 nm for an initially randomly oriented LC, but with

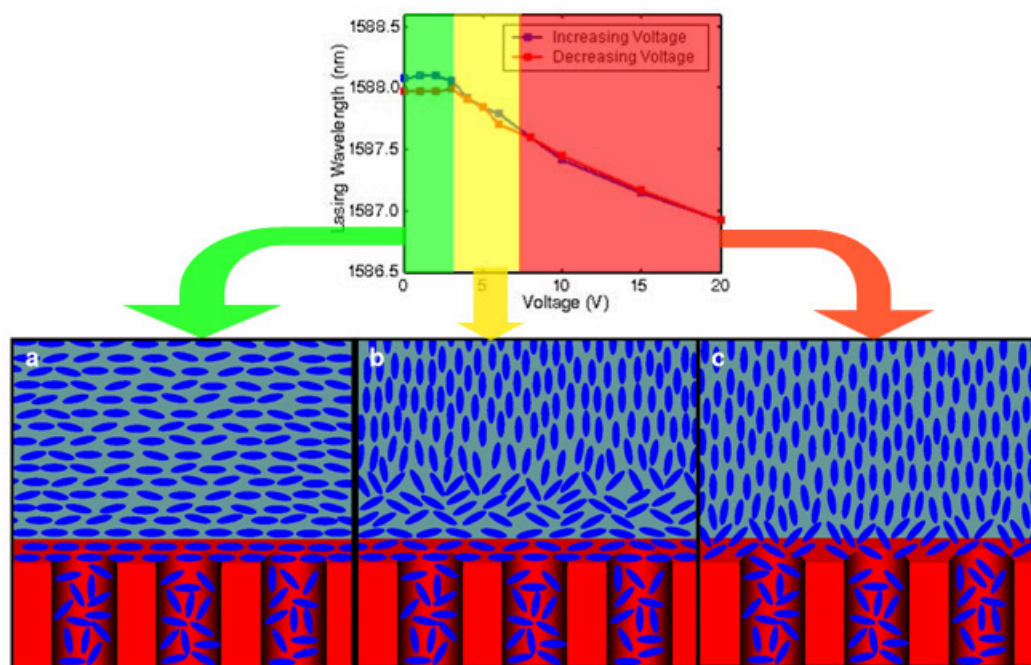


Figure 3.25: Presumed LC orientation at three different field regimes. a) Below threshold, the LC is oriented homogeneously. b) Immediately above threshold the bulk LC aligns parallel to the field, but the LC near the PC surface remains anchored to the surface. c) As the voltage is increased, LC progressively closer to the PC membrane find it energetically favorable to reorient and align parallel to the field. Note LC in holes is drawn with a random orientation for convenience. The actual orientation within the holes is not known, but numerous possibilities exist and are discussed in the previous chapter.

only the top cladding switching to a vertical orientation. As discussed previously, the tuning range is increased when the LC in the top cladding layer is initially oriented such that its director is aligned parallel to the lasing mode's polarization axis. For this case the simulated tuning range increases to 2 nm. The tuning range sharply increases, however, if the LC in the holes aligns with the field. Finite-difference time-domain simulations predict a tuning of 6 nm when both the holes and top cladding are aligned from a *random* state. Therefore the tuning data suggest that only the top LC cladding layer is aligning to the field.

3.6 Discussion and Conclusion

We have fabricated and demonstrated LC infiltrated electrically tunable PC lasers. These PC lasers were fabricated from a slab containing active InGaAsP quantum wells by using electron beam lithography followed by several etching steps. The PC cavity geometry and LC were chosen to maximize the Q of one of the cavity's dipole modes after LC infiltration. Cells were constructed around the laser samples with transparent, conducting ITO plates as the modulating electrodes. The tuning behavior and LC orientation dynamics were characterized by recording laser spectra while adjusting the gate voltage across the cell and also by analyzing interference patterns obtained with PIM. Electrostatic simulations indicate the conducting PC slab screened the applied electric field and the field did not significantly penetrate the holes of the PC. The minimal electric field, surface anchoring, and confinement effects experienced by the LC within the holes suggest the LC orientation could only be controlled in the top cladding layer. The observed laser tuning ranges in conjunction with FDTD simulations of the expected tuning range support this assertion. Furthermore, by studying interference patterns using PIM we discovered the LC in the top cladding layer spontaneously formed homogeneously oriented domains. Simulations indicate the lasers' tuning ranges to be dependent upon the relative orientation of the LC domains to the lasing modes' polarization axis. Experimental results of laser tuning ranges and PIM interference patterns, obtained through thermal cycling the LC between nematic and isotropic states, support this link. Lastly, the absence of a

tuning saturation is believed to be due to the LC anchoring to the PC slab. Although surface anchoring inhibited the overall tuning range of the lasers, an advantageous side effect is that it enabled continuous and precise tuning of the lasing wavelength.

The demonstration of an LC infiltrated electrically tuned PC laser is significant in several respects. First, incorporating various device optimizations can significantly increase the tuning range of the lasers, perhaps by an order of magnitude or more, and possibly enable the lasers to be used in future lightwave systems, spectroscopic applications, etc. Possibilities for increasing the tuning range include designing a higher Q cavity which can support the use of a wide assortment of LCs featuring larger birefringence, using more efficient electrode geometries to enhance the control over the LC orientation, or by using an alignment layer to control the LC zero-field orientation. In particular, if the surface anchoring and confinement effects could be reduced in the holes, then the orientation of the LC in the top cladding layer may be able to propagate through the PC holes and thus dramatically increase the tuning range. Beyond an electrically tunable laser, these structures also provide a platform to probe the behavior of LCs confined in nanoscale geometries while enabling the simultaneous study of a LC's nonlinear optical interaction with an intense optical field. Furthermore, the successful integration of electronics and fluidics with PC lasers demonstrates the flexibility of these structures and suggests that even further functionalization is achievable. In fact, the next chapter discusses one such example of using fluidic and polymeric integration to create optically triggered Q-switched PC lasers. These devices, whose defining functionality emerges directly from the integration of PC lasers with the fluidic and polymeric materials, are specifically designed to bypass the limitations associated with the electrically tuned PC lasers resulting from the inability to control the LC orientation within the holes of the PC lasers.

Chapter 4

Optically Triggered Q-Switched Photonic Crystal Lasers

In the previous chapter we discussed the electrical tuning of PC lasers by the controlled reorientation of infiltrated LC. One of the limitations of that project was that the LC orientation could only be controlled in the top cladding layer above the PC, not in the PC holes. Even if the semiconductor slab did not screen the aligning electrostatic field from the holes, the LC would likely still not appreciably reorient due to the strong surface anchoring present in the small holes. Not controlling the LC orientation in the PC holes is a significant setback because the evanescent field contribution to the cavity mode is relatively small as compared to the contribution within the holes. As such, the achievable tuning of the lasers is limited to a fraction of what it would otherwise be. In the hopes of circumventing this problem, a new material called PAP is introduced and integrated with the PC lasers. The polymer is utilized in implementing a different scheme for modulating the emission of PC lasers. This new scheme is referred to as Q-switching, but it is not the same as conventional Q-switching [2, 15]. Whereas traditional Q-switching yields pulsed lasing¹ from temporally modulating a single cavity mode's Q, the Q-switching presented here involves selecting the lasing mode by quasi-statically modulating the relative Qs of *two* cavity modes.

The chapter begins by introducing PAP. The polymer's physical properties are presented along with a thorough discussion of the polymer's experimental charac-

¹Generally, Q-switching refers to the technique of generating high-power laser pulses by periodically lowering and raising a laser cavity's Q. The lower Q enables an increase in energy buildup within the cavity which can then be quickly released as a brief and intense laser pulse by increasing the Q and bringing the laser above threshold.

terization. Section 2 describes the methodology underlying the Q-switching technique. Section 3 describes the new cavity that is specifically designed to implement Q-switching. The Q tunability and Fourier analysis of the cavity modes are also addressed. Section 4 describes the integration of PAP and LC with PC lasers. Section 5 encompasses the experimental aspects of realizing the Q-switched lasers. It begins by describing the experimental setup and procedures including the PAP/LC alignment procedure. The motivation for using the PAP is its reported ability to align LC. Evidence is then presented demonstrating the LC aligning to the PAP's orientation. The section concludes with the data demonstrating the Q-switching and a discussion of the various possible Q-switching regimes. The chapter ends with some discussion of future directions in research and conclusions.

4.1 Photoaddressable Polymer

The PAP utilized and investigated for integration with PC lasers was chosen for its unique optical properties. The most relevant properties exhibited by the birefringent PAP is its ability to be aligned with polarized visible light and in turn align LC. The polymer features a PMMA backbone with azobenzene chromophores and mesogenic side chains [90,91](see figure 4.1). The chromophores absorb visible light and undergo *trans-cis-trans* isomerization cycles [92–94]. The excited *cis* state is able to rotate and undergoes rotational diffusion (but may also exhibit orientation biases due to steric and dipolar interactions with the neighboring side chains) before returning to the largely immobile ground state. The isomerization process can continue until the chromophore is oriented orthogonal to the polarization of the incident light. At this point, the transition dipole moment is zero and no further excitations can occur. The chromophore and mesogenic side groups tend to align parallel and reinforce each other's orientation. In the end, both the chromophore and mesogenic side chains are oriented orthogonally with respect to the incident polarized light (see figure 4.2). The mesogenic side chains mimic the behavior of LC and also contribute to the polymer's large birefringence (~ 0.4 at visible wavelengths). The liquid crystalline nature of the mesogenic sides chains is also likely responsible for the polymer's ability to align LC.

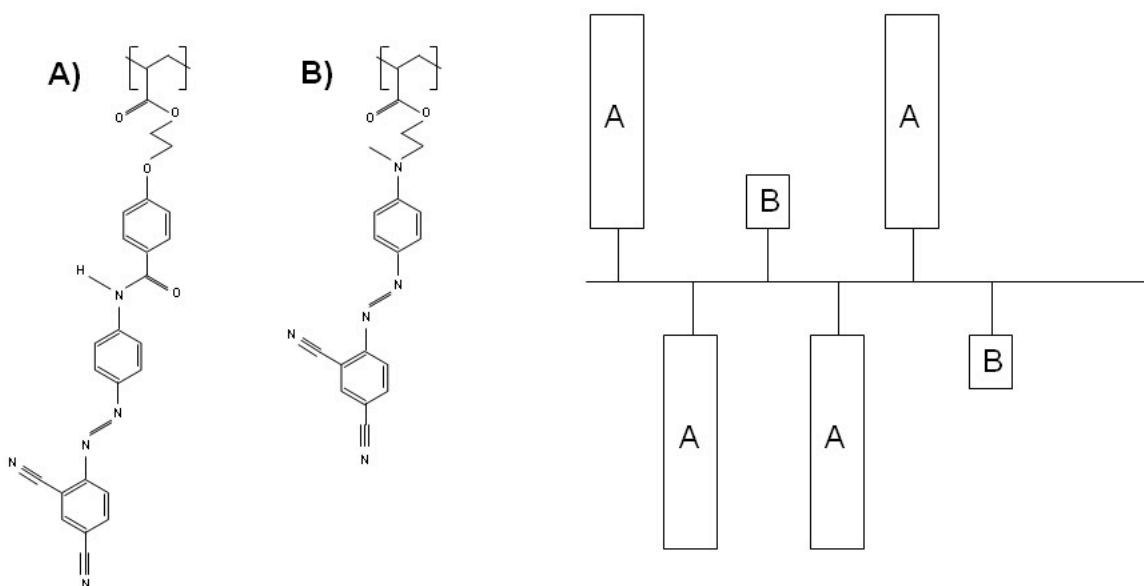


Figure 4.1: Schematic of a typical PAP chemical structure. The longer molecule (a) is the mesogenic side group, whereas the shorter molecule (b) is the azo-chromophore. The chemical composition of the monomers can vary, but the monomers are typically present in roughly equal concentrations in the polymer. The side groups are attached via spacers to a methacrylate backbone. The azo-chromophores absorb light and undergo *trans-cis-trans* isomerization cycles, the primary alignment mechanism in the polymer. The mesogenic groups follow the orientation of the chromophores and help reinforce it [91].

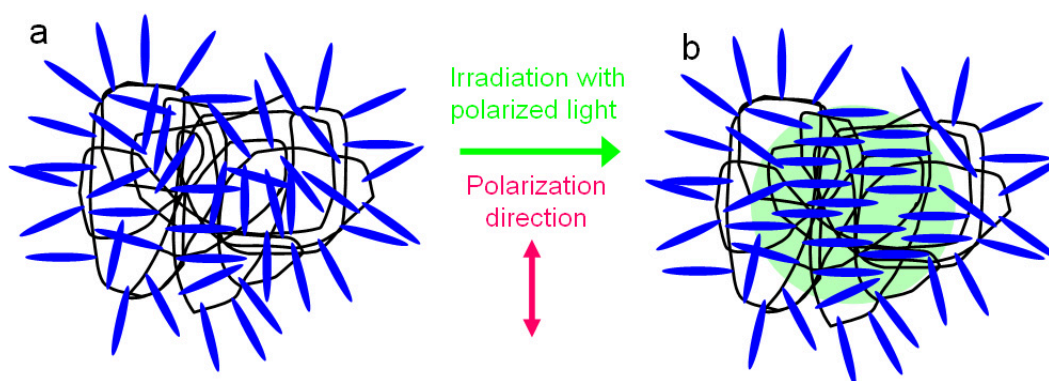


Figure 4.2: Schematic of PAP aligning orthogonal to the polarization axis of incident light. (a) Initially the PAP is randomly oriented. (b) Upon illumination with visible light, the chromophore side groups undergo *trans-cis-trans* isomerization cycles, during which they are free to rotate. This process continues until the chromophore side groups are oriented orthogonally with respect to the actinic light's polarization axis. At this point the transition dipole moment is zero and the chromophore groups can no longer be excited, and so their orientation is frozen. The mesogenic side groups follow the orientation of the chromophores, and eventually the entire PAP becomes aligned orthogonal to the actinic light's polarization axis.

4.1.1 Experimental Characterization

The initial strategy was to directly infiltrate the PC lasers with the PAP and tune the emission by controlling the orientation of the birefringent polymer. Towards achieving this goal a considerable effort was spent investigating the PAP's physical and optical properties. The first priority was to thoroughly characterize the polymer's optical properties. To do this we assembled the optical setup shown in figure 4.3. This setup measured the birefringence of PAP films and transmission of light through the films during illumination by a visible writing laser. The setup initially used a 488 nm Ar ion laser to write the PAP and the birefringence was probed at 670 nm. Later, a second probe laser was added to measure the birefringence at 1550 nm, the wavelength at which the PC lasers were designed to operate. Before discussing the details and operation of the experimental setup, a note is in order. All optical measurements presented here were based on determining the ratio of power measured from two detectors. To minimize the error in these measurements, we calibrated all of the detectors at the beginning of each experimental run. Furthermore, the optical setup was designed with a minimum of optical components to eliminate any superfluous component which could otherwise introduce errors in the measurements. A side effect of this reductionist approach, however, was that the probe lasers were oriented obliquely to the sample (approximately 4° for 670 nm and 8° for 1550 nm). Although this introduced errors in the measurements, these errors were systematic and are believed to not be the dominant error source in the experiment.²

The writing laser first passed through a series of polarizers which set the polarization to either linear or circular. Usually the writing laser was linearly polarized, and the polarizers were arranged such that the intensity was independent (in theory) of the polarization angle. The writing laser was then split by a beam splitter with one part going into a detector and the other part writing the polymer and then going into a second detector. The ratio of power measured by these two detectors was used to determine the absorption of the writing laser by the polymer during the writing process. The birefringence of the polymer was determined by the probe lasers. Both

²Measuring the PAP film thickness with a profilometer is believed to be the dominant error in the characterization measurements.

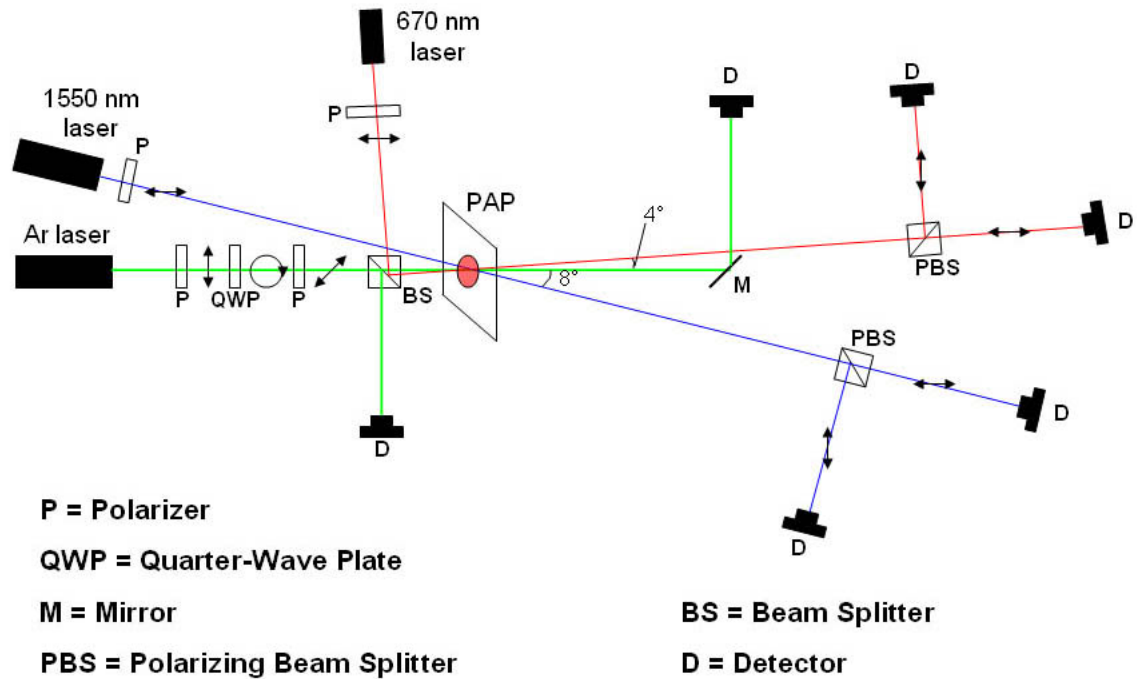
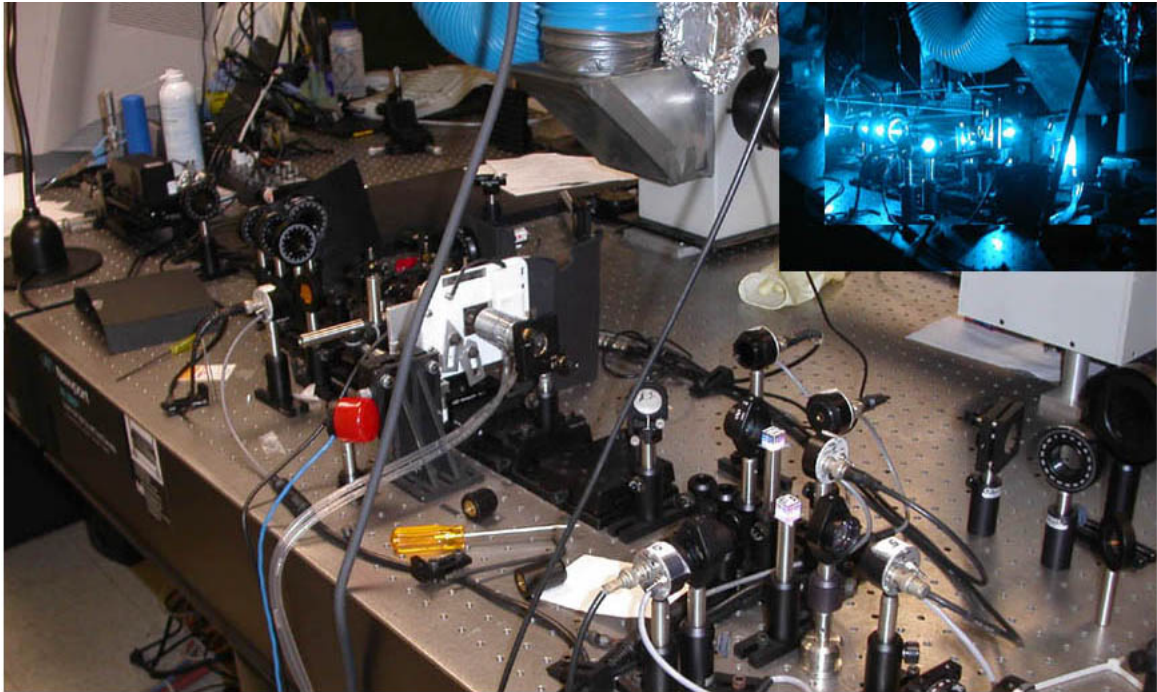


Figure 4.3: Photoaddressable polymer optical characterization setup. (top) Picture of setup. (inset) Picture of setup with Ar laser writing PAP. (bottom) Schematic of optical setup for characterizing the optical properties of the PAP. The PAP was written either with a 488 nm Ar ion laser or a 532 nm frequency-doubled Nd:YAG laser (not shown). The birefringence was measured using probe lasers at 670 nm and 1550 nm. The probe lasers were linearly polarized at a 45° angle with respect to the linearly polarized writing lasers. The birefringence was determined by measuring the polarization rotation of the probe lasers traversing the PAP with detectors arranged to measure the ratio of horizontally and vertically polarized light emanating from the sample.

probe lasers operated under the same conditions. The lasers were initially horizontally polarized when they struck the sample. The polarization was then rotated by an amount proportional to the polymer's birefringence, its orientation with respect to the polarization axis, and film thickness. A beam splitter then separated the transmitted light into horizontal and vertical components before the light struck the detectors. The birefringence was then determined by the following equation [95]

$$\Delta n = \frac{\lambda}{\pi d} \sin^{-1} \sqrt{\frac{I_{\perp}}{I_{\perp} + I_{\parallel}}} \quad (4.1)$$

where λ is the probe laser's wavelength, d is the sample thickness, and I_{\parallel} and I_{\perp} are the powers measured for the horizontal and vertical polarizations, respectively.

Numerous PAP samples were fabricated for testing. The polymer was first dissolved in tetrahydrofuran and diluted to concentrations of 100 g/L, 50 g/L, and 25 g/L, and was then spun at 3000 RPM for 40 seconds on coverslips and heated at 60°C for 10 minutes on a hotplate. The sample thicknesses were measured using a profilometer and found to be approximately 600 nm, 260 nm, and 130 nm, respectively, with some variability between the samples. Note that these samples were considerably thicker than the PAP films ultimately used for the Q-switched laser. When these samples were made, the intention was still to directly infiltrate the PC with the polymer. Once this was no longer the case (see below), then considerably thinner samples became preferable to the original thicker ones.

Below is a discussion of a series of experiments conducted to characterize the physical and optical properties of the PAP. The experiments focused particularly on investigating the properties relevant to PC integration. The first experiment studied the birefringence during numerous writing cycles. The Ar laser's polarization was repeatedly switched between 45° and 135°, and the writing intensity was ~ 140 mW/cm². The data show that the PAP exhibits an initial birefringence of approximately 0.37 at 670 nm which decays quickly with the writing cycles (see figure 4.4). The decay is explained by a phenomenon referred to as photobleaching. As mentioned earlier, the PAP aligns itself orthogonally with respect to the polarization of the writing laser. In other words, for any given writing polarization the PAP can orient itself in any

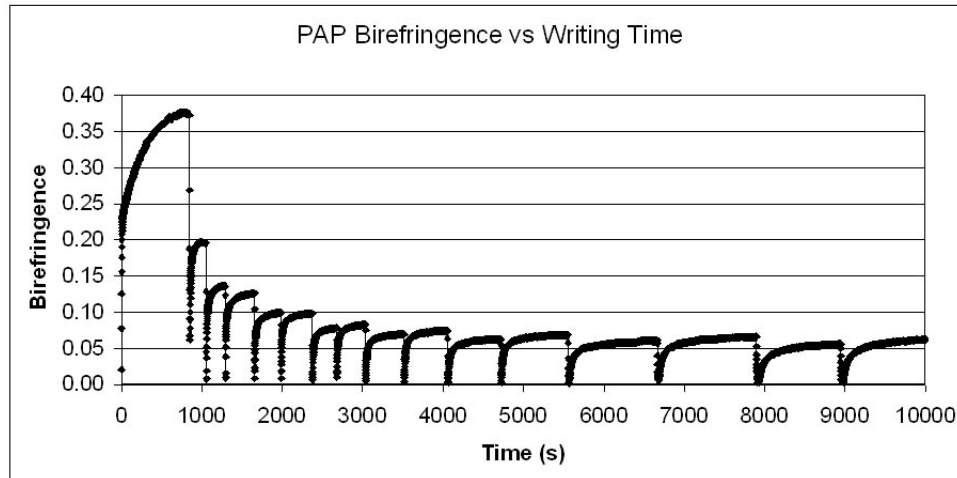


Figure 4.4: Photoaddressable polymer birefringence versus writing time. The initial written birefringence is approximately 0.37 at 670 nm but quickly decays due to photobleaching to around 0.07. The slight oscillation in the maximum birefringence for each writing step is likely due to imbalanced writing intensities between the two different writing polarizations.

direction within a plane that is orthogonal to the polarization axis. The polymer can thus satisfy this requirement by tilting out-of-the-plane of the film, which reduces the measured (in-plane) birefringence (see figure 4.5). With each successive writing cycle and in the absence of a restoring mechanism, the polymer tilts progressively more until it is oriented completely out-of-the-plane and can no longer be written and exhibits zero measured birefringence [96].

For the next experiment a second probe laser was added to compare the PAP's birefringence at 1550 nm to its birefringence at visible wavelengths. Quantifying the birefringence at 1550 nm is important because this is the wavelength region in which the PC lasers operate. Determining the birefringence at this wavelength enables the estimation of the tunability of the lasers. A representative PAP writing dataset is shown in figure 4.6. As is common for liquid crystalline materials, the birefringence is found to be lower at infrared wavelengths. The data show that the birefringence at 1550 nm is approximately 0.67 that of 670 nm. Further experiments suggest the birefringence at 1550 nm is a bit lower, approximately 0.61 that of 670 nm.

The next experiment was designed to study the degree of anisotropy in the film due to the spinning process. Researchers have claimed in the literature that the spinning process induces a planar orientation in the film [97]. To test this we decided

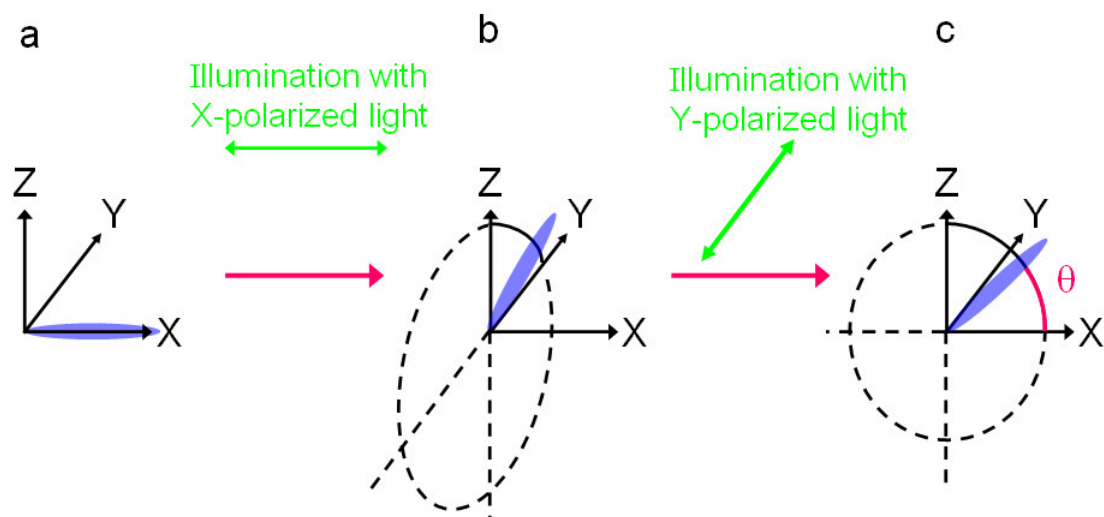


Figure 4.5: Schematic illustrating PAP photobleaching process. (a) Initially the PAP is oriented along the X axis. Then, visible light polarized along the X axis illuminates the polymer. (b) The polymer now rotates until it is orthogonal to the polarization axis. This means the polymer can align itself anywhere along the Y-Z plane and not just along the Y axis. (c) Next, Y polarized light illuminates the polymer, and the polymer now aligns along the X-Y plane. So instead of returning to the X axis, the polymer now possesses some out-of-plane alignment and is oriented at an angle θ with respect to the X axis. A few comments regarding the photobleaching process are in order. Although the polymer can realign anywhere within a plane when illuminated with linearly polarized light, the polymer exhibits a strong bias to maintaining a planar orientation. This bias is attributed to two causes. First, probabilistically the polymer is most likely to realign completely in-plane. This can be seen by viewing the realignment as a rotational diffusion (i.e., random walk) process, and an in-plane realignment represents the shortest “rotational path” available to the polymer. Secondly and probably more importantly, the in-plane bias is also attributed to dipolar interpolymeric interactions which help to maintain a dominant in-plane orientation. Researchers have investigated the factors influencing the photobleaching rate and have even designed new PAP with particular structural characteristics to inhibit the photobleaching and thus increase the number of useful writing cycles available with the polymer.

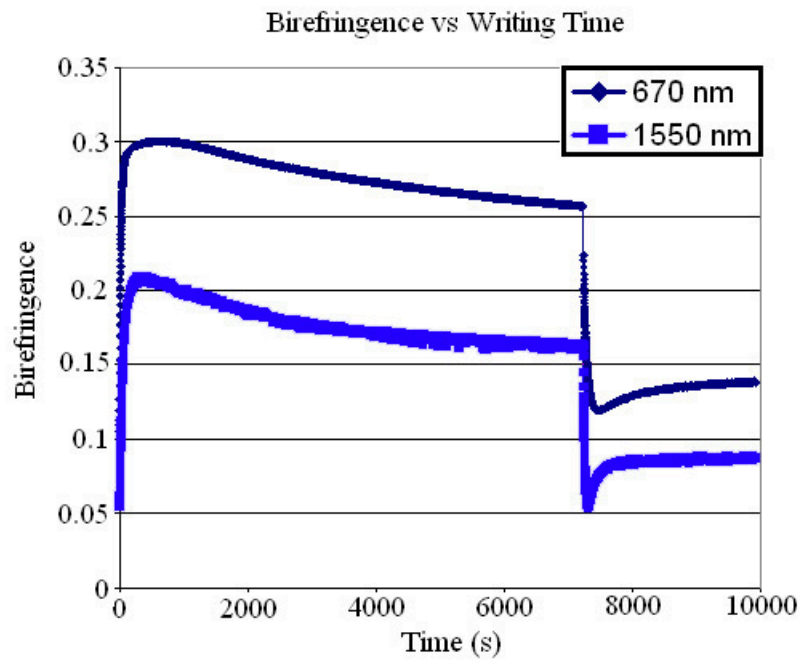


Figure 4.6: Comparison of PAP birefringence at 670 nm to 1550 nm. The PAP's birefringence measured at 1550 nm (the designed optimum operating wavelength for the PC lasers) is approximately two thirds the birefringence measured at 670 nm using the optical setup and procedure described earlier in the chapter.

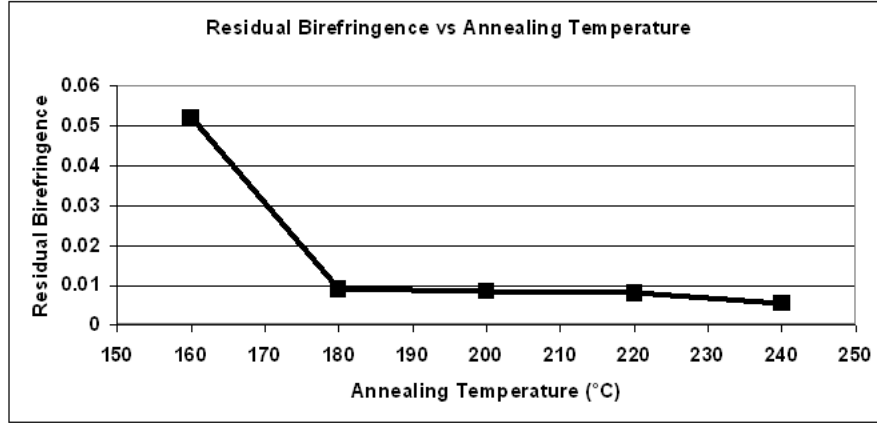


Figure 4.7: Residual PAP birefringence versus annealing temperature. The PAP's birefringence was completely erased for annealing temperatures above 160°C, and the PAP became randomly oriented. The subsequent written birefringences were lower after annealing, indicating that the polymer initially possessed a degree of planar alignment due to the spinning process. The residual birefringences at annealing temperatures of 180°C and higher are primarily attributed to measurement error intrinsic to the optical setup.

to write the polymer samples before and after annealing them and to compare the subsequent birefringence. The samples' initial birefringence was measured to be approximately 0.4 (at 670 nm) before the annealing. The samples were then annealed on a hotplate for 15 minutes at several temperatures and the birefringence remeasured (figure 4.7). Although some birefringence remained up to 160°C, the birefringence was completely eliminated at higher temperatures. The samples were then rewritten, but the maximum birefringence obtained after annealing was usually about 0.2, half of the pre-annealing birefringence. This result agrees with the hypothesis that the spinning process introduces a planar orientation. The annealing randomizes the polymer and thus increases the out-of-plane alignment.³ This in turn decreases the maximum (in-plane) birefringence that can be written with these samples. Conducting further experiments with annealing cycles and measuring the subsequent written birefringence shows that the possibility does not exist of thermal degradation being a source for the decrease in birefringence. The planar orientation induced by the spinning process not only increases the achievable birefringence, but is also conducive for aligning LC and is discussed later in this chapter with PIM.

The last set of experiments investigated the writing of the PAP under conditions

³The PAP orientation can also be randomized (and photobleached) using circularly polarized light.

that mimic those to be found in the PC setup. The polymer writing was tested with a 40 mW frequency-doubled 532 nm Nd:YAG laser, the actual writing laser used in the PC laser setup. Considering the polymer's absorption band cutoff was around 630 nm, the green laser was suitable for writing the polymer as anticipated. The last experiment involved testing the writing of the polymer with white light. This was crucial because white light was required for imaging purposes during testing of the PC lasers. If white light could write the polymer fast enough then it may have been unintentionally written and completely photobleached before the actual experiments even began. Multiple tests with several light intensities were used for the testing and we found that the polymer could be written with white light and even diffuse unfocused white light (albeit slowly). In response to this, precautions were implemented during the PC laser testing to prevent inadvertent polymer writing and are discussed later in the chapter.

4.1.2 Applications

Photoaddressable polymer may be suitable for future optical data storage applications. Two methods which have been proposed include using the polymer either as a thin rewritable recording layer analogous to the DVD format or possibly as write-once data storing holograms [91, 96]. One reason why PAP may lead to significantly higher data storage for DVDs is their ability to implement gray level recording. The PAP birefringence can be locally written with a laser. The state or "bit" is then read by measuring the degree of polarization rotation experienced by a probe laser traversing the polymer film. Relatively small variations in the polarization rotation can be measured and so each film location can be used to store considerably more information than with conventional two-state bits. Although this method permits higher data densities for DVD-like storage devices, densities can be further increased with holographic-based devices. A two-dimensional image (possibly created with LC-based spatial light modulators) is encoded onto a signal laser and interfered with a reference beam inside a block of PAP. The interference pattern is written into the polymer as a hologram and can be read in parallel by shining the reference laser on the sample. Data densities can be further increased using angular multiplexing.

Slightly changing the incident angle of the reference laser enables new holograms to be written and read without interfering with the other holograms. Prototypes demonstrating these PAP-based storage techniques have been constructed and successfully tested. It remains to be seen if the technology will sufficiently mature for products to reach the marketplace though.

4.2 Motivation for Q-Switching

One of the limitations encountered with the electrically tuned PC laser, described in the previous chapter, was the inability to control the LC orientation in the holes of the PC. The tuning only occurred by changing the refractive index in the top cladding layer through LC realignment, which only overlapped with the mode's evanescent field. As a result, the tunability of the lasers was greatly diminished. Increased tuning can of course be achieved by somehow obtaining control of the LC's orientation in the holes of the PC, but considering how strongly the LC is anchored to the inner walls of the holes, this possibility remains unlikely even if an electric field can penetrate into the holes. Another alternative for increasing the tuning range is to completely change the method by which the cavity is tuned. Instead of relying on tuning by changing the optical path length of a single cavity mode, the tuning can be increased significantly by incorporating a second mode and using an entirely different tuning methodology referred to as Q-switching.

4.2.1 Q-Switching Methodology

The advantage of the Q-switching technique is that it surmounts the fundamental limitation plaguing the optical-path-length-based tuning method by largely decoupling the birefringence of the infiltrated material from the cavity tunability. This is achieved by no longer using the infiltrated material as a tuning element but rather using it as a switching element to switch the cavity emission between one of two cavity modes (see figure 4.8). To implement this, first a cavity was designed and fabricated that supported two high-Q orthogonally polarized modes. Then the cavity was infiltrated with a birefringent material such as LC. Since the cavity modes are

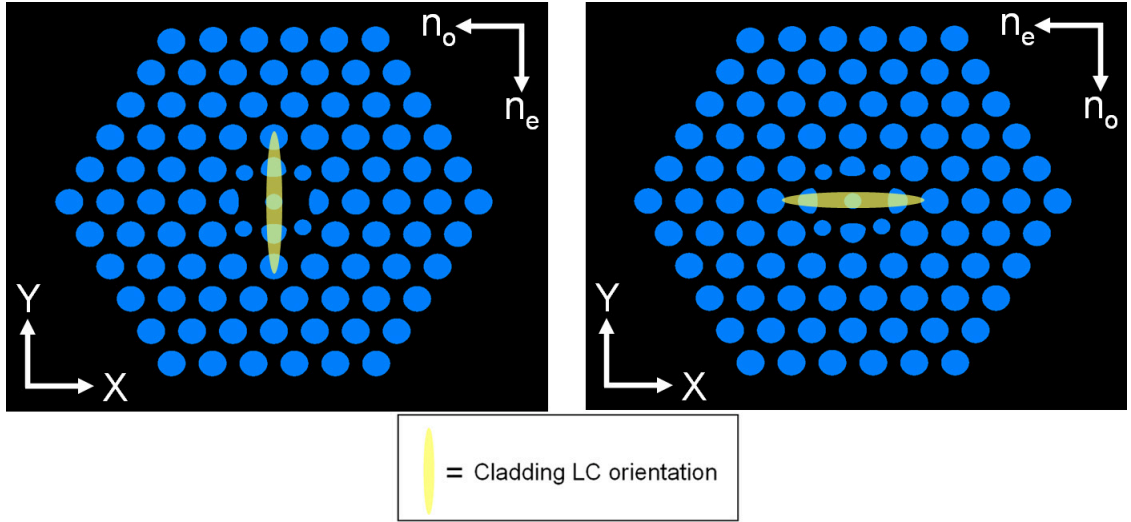


Figure 4.8: Schematic illustration of Q-switching methodology. By rotating a birefringent material in the top cladding layer (e.g., LC), the effective refractive index experienced by orthogonally polarized cavity modes can be controlled. This, in turn, affects the relative modal Qs and is the basis for the implementation of the Q-switching technique presented in this chapter.

orthogonally polarized and the modal Qs depend sensitively on the ambient refractive index, by controlling the orientation of the LC one can control the refractive index, and hence Q, of each mode. By rotating the LC, the relative Qs can be tuned and the desired mode can be selected to lase. Lastly, since the two modes resonate at different wavelengths, switching a laser's output between the modes also switches the wavelength of the laser's emission.

Experimentally, the Q-switching can be implemented with a scheme that controls the in-plane orientation of infiltrated LC. Both electrical and optical methods were investigated to actuate the LC. Pairs of electrodes were deposited around the PC samples to generate the in-plane electric fields required for the LC actuation (see figure 4.9 (a) and (b)). Although never fully implemented, the mask designs and processing steps were mostly characterized. For completeness, a thorough discussion of this fabrication procedure is presented later in the chapter. The second LC alignment method utilized a layer of PAP whose alignment was controlled with a polarized green laser. The PAP oriented orthogonally with respect to the incident light's polarization axis and, in turn, the LC aligned parallel to the PAP (see figure 4.9 (c) and (d)). This LC alignment method was used to implement the Q-switching, and the details of the method are described later in the chapter.

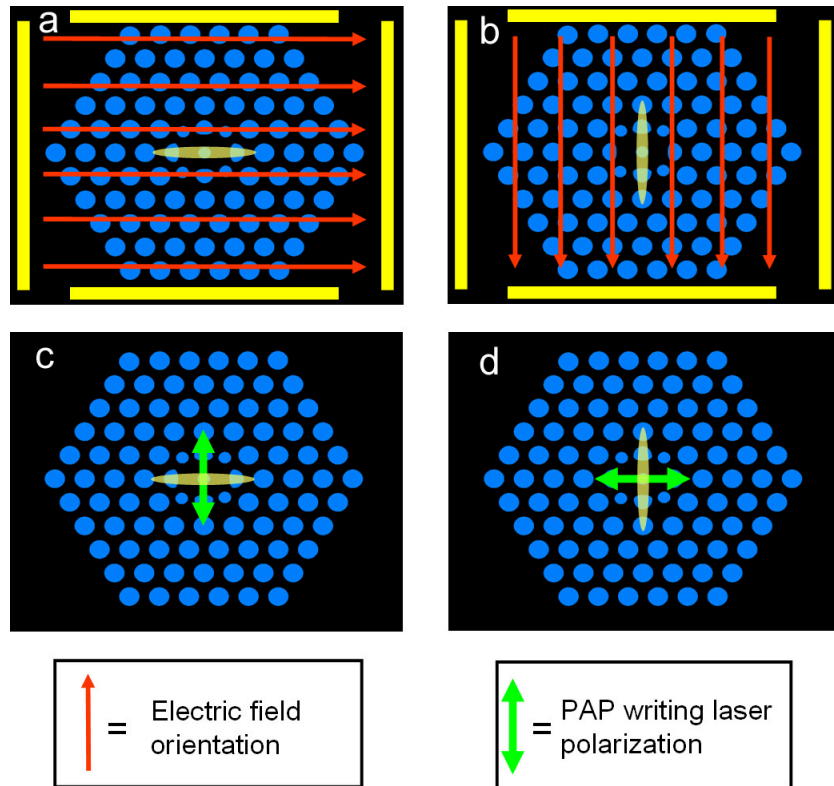


Figure 4.9: Schematic of Q-switching implementations utilizing LC as the control element. (a) and (b) Electrodes are used to generate electric fields to align the LC in the top cladding layer. By adjusting the potential across the two sets of electrodes, the LC can be aligned in any arbitrary direction in the plane of the PC. (c) and (d) A polarized laser, in conjunction with a film of PAP, is used to align the LC orthogonal to the writing laser's polarization axis. By controlling the polarization, the LC can be aligned in any arbitrary direction.

4.3 Photonic Crystal Cavity Design

The cavity design criteria for the Q-switched PC laser was significantly more stringent than for the electrically tuned laser. Beyond having a single post-infiltration high-Q mode which substantially overlapped with the environment, the implementation of the Q-switching technique required *two* orthogonally polarized high-Q modes after infiltration. Specifically, our goal was to design a cavity that supported two modes with Qs of at least 4000 at an ambient refractive index of 1.5. Setting this somewhat arbitrary level for the Qs was meant to compensate for any extra losses incurred by the infiltrating material and to guarantee lasing was possible in both modes simultaneously. The design of a cavity which satisfied all of these requirements took considerable effort. The general strategy employed was the following. To remove the possibility of a spurious FDTD simulation⁴ or some other abnormality from unjustly eliminating a design family from consideration, we first simulated a group of closely related cavity designs with an ambient refractive index of 1.0. Simulating all cavity Qs with a 1.0 ambient refractive index provided a baseline for comparing new designs with past simulations. We, however, were not interested in the air immersed cavity Qs per se, but rather valued these Qs for their predictive power in identifying designs which featured high Qs, even with high ambient refractive indices. From our experience, we know the Qs drop precipitously as the ambient refractive index increases, and we also know the drop in Q *nearly* always decreases monotonically with increasing ambient refractive index. A typical Q versus ambient refractive index dependence is shown in the next section (figure 4.13). Using this known behavior of Q and ambient refractive index, we modeled the cavities and discarded the ones that did not support at least one mode with a Q above a certain threshold, say 12,000.⁵ The cavities which passed this filter were then modeled with an ambient refractive index of 1.5 and were optimized until at least one mode's Q surpassed 4000, if possible. If this goal was

⁴The FDTD simulations were conducted in a similar manner as the ones described in chapter 3 with one notable exception. Due to the more stringent design requirements, we sought to increase the simulation accuracy by boosting the spatial resolution to about 31 points per lattice period.

⁵We acknowledge that initially simulating cavities in air and later optimizing them with higher ambient refractive indices (and vice versa) raised the possibility of discarding some designs with abnormal or pathological Q/ambient refractive index dependencies (e.g., Q is constant at 5000, independent of ambient refractive index). We took this concern under consideration and attempted to minimize the probability of this occurring by setting the air immersed Q threshold "relatively low." In the end, we thought the benefit of having a common baseline of Qs for comparison with all previously modeled cavities outweighed the small risks of prematurely discarding legitimate cavity designs.

met, then the cavity was further optimized to maximize the Q of the second mode while not lowering the Q of the other mode below 4000. This process continued until a cavity satisfying all objectives was discovered.

Admittedly, the cavity design algorithm contained a substantial amount of iterative random-walk-style optimization. Machine learning techniques such as genetic algorithms and neural networks as well as inverse mathematical methods were evaluated for developing a more efficient algorithm for cavity design optimization, but ultimately were discarded for several reasons. Perhaps the most serious problem which afflicts all automated cavity design algorithms is the large dimensionality of the design problem. By sacrificing thorough exploration of the design parameter space, the dimensionality can be decreased by restricting the number of free parameters specifying the cavity design. The design space is truly enormous, though, and reducing it to the point of a tractable design problem will likely only result in mediocre cavities (or restrict the design algorithm to merely tweak, enhance, or simply rediscover an already known decent geometry). Another obstacle in using the genetic algorithms and neural networks methods is the representation or parameterization. How does one efficiently parameterize a cavity such that machine learning algorithms can make sense of the parameterization and then use it for optimizing the cavities? The parameterization dilemma itself is not insurmountable, but it leads to another hurdle. The phase space for “good” cavity designs is extremely sparse and little correlation may exist, in general, between the parameters specifying “good” cavities (or at least the correlation between good cavities can be extremely difficult to decipher). In other words, the machine learning algorithms can not effectively learn to optimize cavities solely by analyzing the evolution of the cavity parameters and the resulting effects on Q s because multiple cavities with little correlation in the parameters specifying their designs can have equally high Q s. The success of machine learning algorithms can likely be greatly improved, however, if they can be used to identify and optimize cavity characteristics which universally (or at least frequently) boost cavity Q s. For example, graded lattices [98] and displaced holes [64] appear to boost Q s by decreasing a mode’s Fourier components which lie above the cladding’s light cone. Using machine learning techniques to optimize such general design guidelines and then ap-

plying the method to particular cavity designs is likely to be somewhat successful and should be pursued. Another limitation of some machine learning techniques is the reliance of the techniques on training data. Unfortunately, the number of known good (i.e., single high-Q mode cavities) cavities is very small (~ 10), let alone the number of known cavities which satisfy the requirements for the Q-switching technique introduced here (1). This provides for a very meager training set for learning algorithms.

Beyond machine learning techniques, several researchers have studied the cavity design problem and have made insightful discoveries (which were discussed in the previous chapter) [64, 74, 75]. These techniques are undoubtedly useful in designing single-mode high-Q cavities in air, but it is unclear how effective these methods are for designing a cavity satisfying the more stringent requirements for Q-switching from scratch. All of this suggests that the cavity design problem is far from being solved. As experiments demand cavities with atypical or multiple constraints, new insights will be required to expedite the design process. Improving cavity design techniques remains an active area of research.

4.3.1 Photonic Crystal and Cavity Parameters

The overarching criteria governing the design of the cavity was that it supported two orthogonally polarized high-Q modes *after* LC infiltration. As with the previous electrical tuning project, we investigated cavities within a triangular lattice because of its relatively large photonic bandgap and resulting robustness towards a decreased refractive index contrast. We concentrated our modeling efforts on point-like defect cavities, as these cavities are known to generally support orthogonally (X and Y) polarized dipole modes [99]. An early success in the cavity design process was the realization of a cavity with a Y polarized mode exhibiting a high Q, even with an ambient refractive index of 1.5. The next step was to modify this design in such a way to raise the Q of the X dipole mode while not sacrificing too much Q from the Y dipole mode. To achieve this, we settled on the strategy of trying to replicate the cavity as seen by the higher-Q Y dipole mode for the X dipole mode. We were able to do this without seriously degrading the Y dipole mode because of the orthogonal

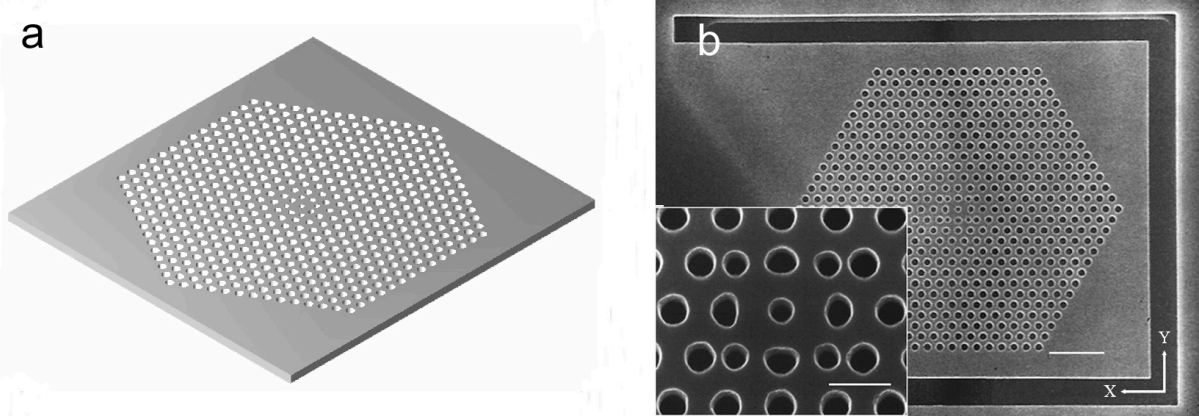


Figure 4.10: Schematic of idealized cavity design and real fabricated cavity. (a) Three dimensional rendered image showing idealized cavity. (b) Scanning electron micrograph of actual fabricated PC laser cavity. The square-like cavity geometry is designed to replicate the cavity experienced by the Y polarized mode for the X polarized mode without substantially decreasing the Y mode's Q. The periodicity of holes is 450 nm. The inset shows a close-up of the cavity geometry taken with a sample tilted 15°. Scale bar, 2 μm . Inset scale bar, 500 nm.

modal profiles. The X mode is largely confined along the cavity's Y axis of symmetry, whereas the Y mode is confined along the X axis. So by tweaking the cavity design along the Y axis, the Y mode's effective cavity could be replicated for the X mode without significantly perturbing the cavity as experienced by the Y mode. We found our strategy to be successful, and an SEM image of the intuitive final cavity design and resulting mode profiles are shown in figure 4.10 and 4.11, respectively. Furthermore, as expected, the dipole-like modes are orthogonally polarized as verified by the FDTD simulations as shown in figure 4.12. The main characteristic of the cavity is the square-like defect structure. The square-like structure achieves the goal of boosting the X dipole mode's Q at little expense to the Y mode's Q. The cavity is also embedded within a graded lattice [98], which further enhances the modal Qs. The full specification of the cavity can be found in table 4.1.

A couple of concluding remarks regarding the cavity modeling are in order. First of all, we found that optimizing a cavity's Q in air does not necessarily optimize the cavity for a higher ambient refractive index. The X and Y dipole modes corresponding to the final cavity design have relatively modest Qs of 12,000 and 30,000, respectively in air, but both have relatively high Qs of 4000 at an ambient refractive index of 1.5 (figure 4.13). Throughout the course of the cavity modeling, numerous cavities were

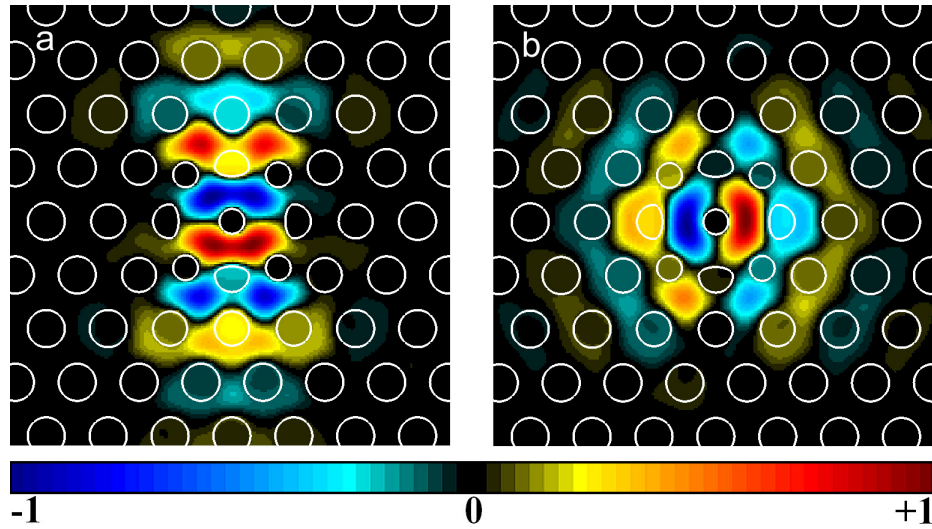


Figure 4.11: Photonic crystal cavity modes. Finite-difference time-domain simulation of Z component of magnetic field for (a), X polarized and (b), Y-polarized modes. The orthogonal nature of the modes' polarizations can be seen in the magnetic field patterns but are explicitly shown in figure 4.12.

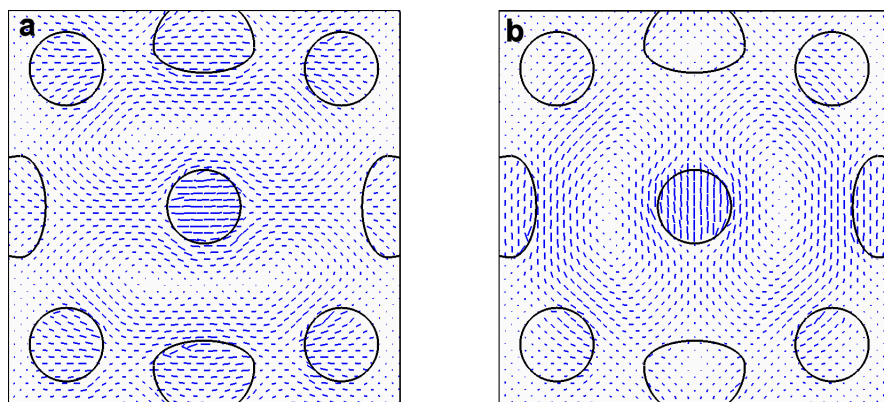
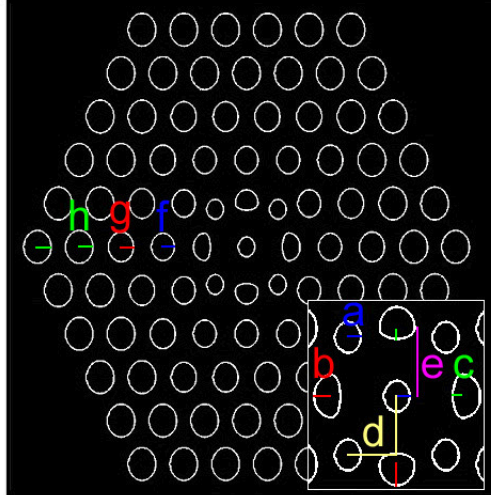


Figure 4.12: Photonic crystal cavity modal polarization structures. Finite-difference time-domain simulation of the (a) X polarized and (b) Y polarized cavity modes.



Label	Parameter description	Value
a	Radius of small holes (central and 4 holes)	.2 (r/a)
b	Radius of half-holes	.275 (r/a)
c	Minor axis of half-ellipses	.5*.275 (r/a)
d	X and Y displacement of 4 holes from center	.75 a
e	Y displacement of vertical half circle/half ellipses	$\sqrt{3}/2 a$
f	Radius of first hole in graded lattice	.275 (r/a)
g	Radius of second hole in graded lattice	.3 (r/a)
h	Radius of normal holes	.33 (r/a)

Table 4.1: Detailed specification of Q-switched cavity design. Any cavity parameter which is not explicitly specified is to be taken as the unaltered crystal value.

discovered with higher air-cladding Qs, but the Qs tended to plummet with increasing cladding refractive index and were lower at an ambient refractive index of 1.5. Also, the most significant challenge in the design process was to get both modes' Qs above the 4000 threshold. Even though the design efforts continued after the discovery of the first cavity, satisfying all stated requirements, the original cavity remains the only known cavity which possesses two modes with Qs of at least 4000 at an ambient refractive index of 1.5.

4.3.2 Cavity Q Tunability

As mentioned earlier, the Q-switching is in part due to the tuning of the relative Qs of the two cavity modes. The degree of control we have over the cavity modes' Qs is dependent upon the sensitivity of the Qs to the ambient refractive index and on our ability to control the ambient refractive index. Shown below in figure 4.14 is the reproduced figure 4.13 displaying the sensitivity of Q versus ambient refractive index with the addition of a darkened box highlighting the refractive index range accessible by the infiltrated LC (ZLI-3086 from Merck, $n_o = 1.5040$, $n_e = 1.6171$ at 589 nm). Fortunately, the Q tunability implied by the figure underestimates the real tunability. To understand why this is the case, first note that this figure was generated from simulations which assumed an isotropic ambient refractive index. In reality, the

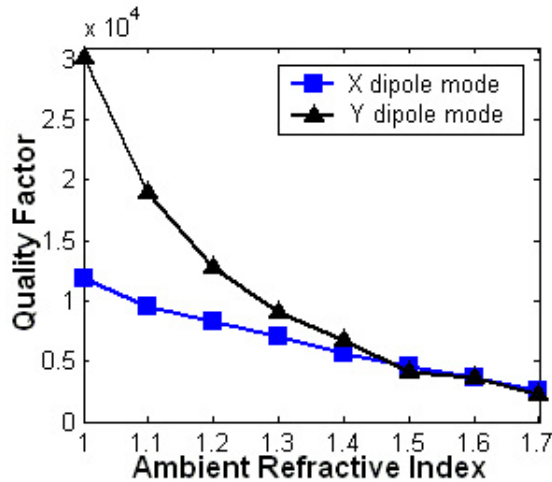


Figure 4.13: Simulation of cavity mode Qs versus ambient refractive index. Although the modal Qs are significantly different at low ambient refractive indices, they converge at higher refractive indices, and both modes maintain a Q exceeding 4000 even at an ambient refractive index of 1.5. These high Qs are critical for achieving lasing with both modes after infiltrating the cavities with LC.

infiltrated LC creates an anisotropic ambient refractive index environment which has an enormous effect on the cavity Qs. In particular, the rotation of LC produces an asymmetry in the cladding refractive indices, significantly degrading the Qs [100]. So in reality our control over the cavity Qs is likely to far exceed that which is implied in figure 4.14.

4.3.3 Fourier Space Analysis of Cavities

In chapter 3 the important concept of the “light cone” was introduced, and its relevance to estimating cavity mode Qs was discussed. Cavity mode contributions above the light cone are not well confined and are free to radiate vertically into the cladding layers. In light of this, several researchers have proposed and implemented a cavity design rule for maximizing a cavity’s Q by minimizing the modal components above the light cone [64, 74, 75]. We use this design rule to evaluate the differences between the new cavity design presented earlier in this chapter and the one presented in the previous chapter.

First, for each cavity geometry we utilized FDTD simulations to excite the cavities and then to isolate the resonances. Next we obtained spatial field profiles of the cavity modes by filtering the temporally evolving fields at the resonant cavity frequencies.

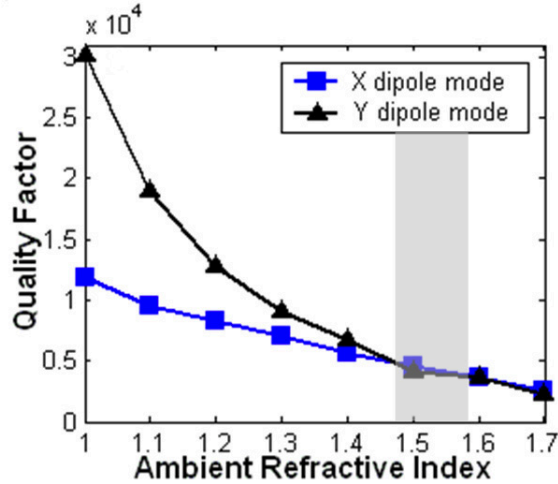


Figure 4.14: Simulation of cavity mode Q s versus ambient refractive index. The gray box marks the ambient refractive index range achievable by infiltrating the PC with the LC. This refractive index range in conjunction with the Q simulations provide an estimate of the Q tunability of our cavities. Note, however, the Q tunability estimate using these simulations likely underestimate the real tunability of the cavities because they assume an isotropic ambient refractive index, whereas in reality the cavities have anisotropic ambient refractive indices.

Once we had the spatial modal profiles we then applied a Fourier transform to obtain the modal profiles in momentum (or k) space. Figure 4.15 shows the k -space modal profiles for the cavity modes discussed in this chapter and the previous chapter. Light cones are indicated by the red circles. Any modal components within these circles are leaky and contribute to cavity losses. The figures on the left (right) column were obtained with an ambient refractive index of 1.0 (1.5). As the ambient refractive index increases towards 1.5, the light cone increases for all the cavity modes and consumes larger portions of the modes. This effect can clearly be seen by comparing the images from the left and right columns. Further analysis of the images reveals the likely reason why the new cavity design supports significantly higher Q s after LC infiltration than the previous design. By comparing the simulation of the old Y polarized cavity mode (figure 4.15 (b)) to the new Y and X polarized cavity modes (figure 4.15 (d) and (f), respectively), one sees the old cavity mode's k -space distribution start to significantly overlap with the light cone at the higher ambient refractive index, whereas the new cavity mode distributions overlap considerably less. This characteristic is likely the reason why the new cavity design exhibits two significantly higher- Q modes even after LC infiltration than the earlier design.

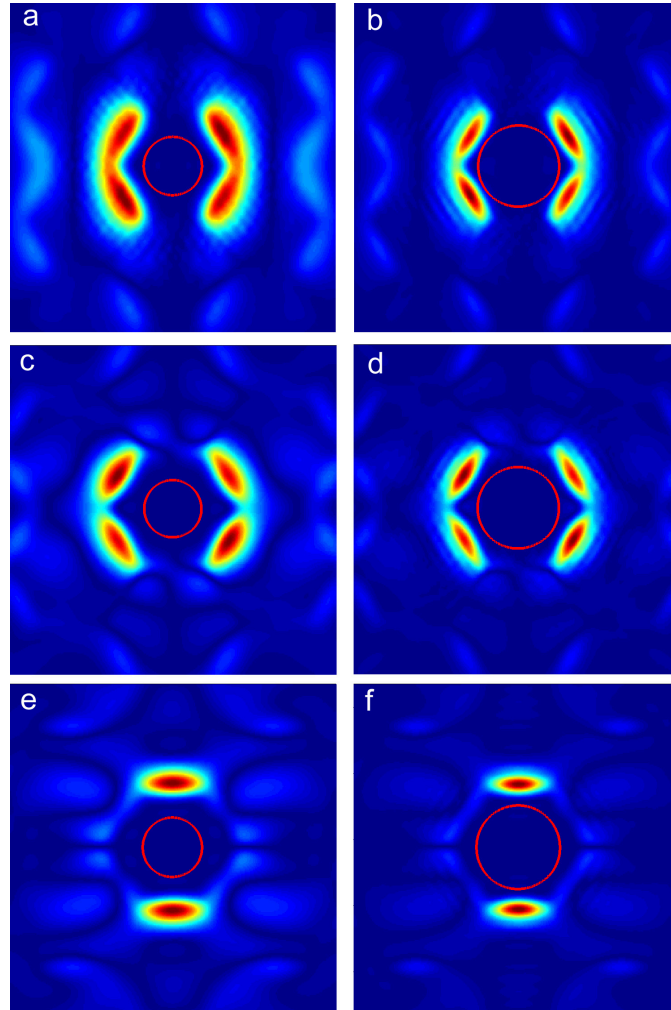


Figure 4.15: Simulation of k-space modal distributions and cladding light cones. Simulations of k-space distributions for (a) and (b) old Y polarized cavity mode, (c) and (d) new Y polarized cavity mode, and (e) and (f) new X polarized cavity mode. The simulations on the left column feature an ambient refractive index of 1.0, whereas the right column has an ambient refractive index of 1.5. The red circles represent the cladding light cones. Note how a significantly larger fraction of the mode in (b) is enclosed within the light cone than in (d) and (f). This is likely the reason for the superior Qs exhibited by the new cavity design after LC infiltration. The figures are plots of the absolute value of the Fourier transformed B_z field amplitudes. The field profiles are acquired from the middle of the PC slab.

4.3.4 Laser Fabrication and Wafer Specification

The wafer specifications and fabrication procedures were similar to those discussed in chapter 3. A new wafer was grown with the same specifications given in table 3.1. Like the previous wafer, the new one also had an experimentally measured emission maximum at $1.55 \mu\text{m}$ (shown in figure 4.19). The fabrication procedure remained the same as the procedure illustrated in figure 3.8 except for minor changes in a couple etch parameters necessary to compensate for changing etch conditions over time.

4.4 Integration of PCs with PAP and LC

The initial motivation behind using PAP can be understood in terms of the problems encountered utilizing LC to electrically tune the emission wavelength of PC lasers. The most serious limitation with LC was the inability to control its orientation within the PC holes. This difficulty arose because of two reasons. First, the electric field was screened from inside the holes by the doped semiconductor slab. The screening by itself, however, may not preclude alignment within the holes. In theory, the alignment of the LC in the top cladding layer can propagate through the holes of the PC if it were not for the second problem: surface anchoring. The LC likely experienced strong surface anchoring effects at the inner walls of the PC holes, which would inhibit alignment even in the presence of an electric field. Surmounting this alignment problem was the initial motivation behind directly integrating PAP with the PC lasers. The alignment mechanism for PAP, which is based on photo-induced isomerization cycles, is fundamentally different than for LC and could possibly be immune to confinement effects. Unfortunately, due to fabrication difficulties we were never able to successfully infiltrate PC holes with the PAP to test this hypothesis. We made numerous attempts to spin PAP films onto the PC samples but were never able to both infiltrate the PCs and still maintain a reasonably homogeneous film. Spinning extremely dilute solutions favored high quality films but did not infiltrate the crystals well (see figure 4.16). On the other hand, spinning more concentrated solutions may have infiltrated the crystals more, but the film quality was poor (see figure 4.16). One source of difficulty associated with the spinning process is linked to the solvent used for

PAP dissolution. The solvent, tetrahydrofuran, evaporates extremely quickly, which makes spinning high quality films difficult. Using another solvent (if it exists) that evaporates slower may improve matters. Another possibility for directly infiltrating PAP with PCs may be to use critical point drying techniques. Again, another solvent which is both suitable for critical point drying and dissolves PAP must be found before this can even be tried. Stamping a film of PAP into a PC may be another alternative. This technique is not appropriate for our fragile membrane structures, but other robust PC devices supported by a low index oxide layer may be compatible with the stamping process. After failing to infiltrate the PC lasers directly with the PAP we decided to instead utilize the PAP as an optically triggered LC alignment layer. Using the PAP film as an intermediary to optically control the LC orientation bypassed the arduous task of obtaining the same functionality using electrostatic fields.⁶

4.4.1 Photoaddressable Polymer Film Fabrication

The purpose of the PAP film was to serve as an optically actuated LC alignment layer. Ideally the layer should respond quickly to the optical trigger and minimally scatter and absorb the pump beam and laser emission. As discussed in the PAP section in the beginning of the chapter, the response time of the polymer increases with film thickness due to absorption of the actinic light. So to minimize both absorption and writing time, extremely thin films should be used. Spinning thinner films also generally produced higher quality films. Our PAP films were made first by heavily diluting the polymer in tetrahydrofuran at a concentration of 15 g/L. The solution was then mixed for 10 minutes with a magnetic stir bar to help ensure complete dissolution of the PAP in the solvent. The PAP was then deposited onto a coverslip that was already spinning at 3500 RPM for 40 seconds. Depositing the PAP onto spinning substrates dramatically increased the quality and uniformity of the films.⁷ Finally, the PAP samples were baked on a hotplate at 60°C for 10 minutes to ensure

⁶Using electrostatic fields to align the LC was also investigated. Later in the chapter we discuss our efforts to develop the processing procedure required for depositing multiple layers of electrodes necessary to generate the in-plane electric fields for the Q-switching technique.

⁷Tetrahydrofuran has an extremely high vapor pressure and evaporates appreciably even in the time necessary for the substrate to ramp up to the target RPM.

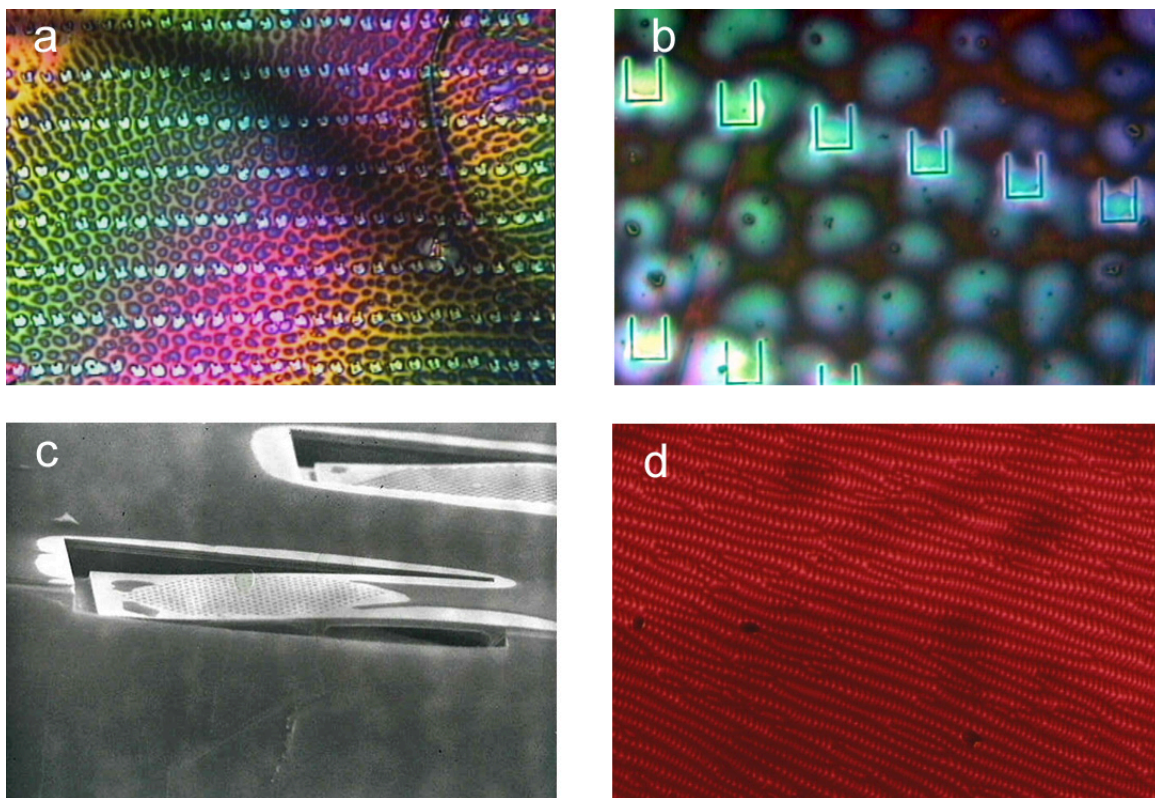


Figure 4.16: Images showing poor PAP film quality. (a) PIM image taken after spinning a heavily diluted PAP solution onto a PC sample and enclosing the sample in a LC-filled cell. The bright areas denote the PC samples and indicate the PAP did not infiltrate the PC samples. (b) Close-up of some PC samples from (a). (c) An SEM image taken of partially collapsed PC membranes from the same sample as (a) and (b). The white areas are where there was no PAP. In other words, the PAP films *avoided* the PC samples. The formation of PAP films seems to be repelled by surface inhomogeneities and edges. The membranes likely collapsed during the spinning process. (d) An optical micrograph image of a concentrated PAP solution spun onto a glass coverslip. The film appears to be inhomogeneous, featuring radially directed striations. These striations may form in response to rapid solvent evaporation during the spinning process.

complete solvent removal. Atomic force microscopy measurements indicated the PAP film thickness was 31 ± 1 nm with an estimated surface roughness of 1 nm.

4.4.2 Liquid Crystal Parameter Considerations

The same deleterious effects associated with LC infiltration mentioned in the previous chapter also afflicted the Q-switched PC laser. Again, the main encumbrance was the significant degradation of the cavity's Q due to the decreased vertical confinement caused by the lower refractive index contrast at the semiconductor/cladding interface. To surmount this difficulty, in the last chapter we chose to integrate the PC lasers with an LC with the minimum refractive indices. Although we were able to achieve lasing using this LC, the small birefringence reduced the tuning of our lasers. Fortunately for this project we have an improved cavity design with significantly higher Qs. The higher Qs alleviated some of the restrictions placed on the selection of LC by enabling the use of LC with higher refractive indices and larger birefringence. A second loss mechanism associated with LC is scattering from heterogeneously aligned LC molecules [31]. This scattering rate is sensitive to the LC's dielectric anisotropy (scaling as the second power of $\epsilon_{\parallel} - \epsilon_{\perp}$) and should not be completely discarded. Unfortunately we do not know the degree of heterogeneity in the LC alignment in our devices, and so an educated guess must be made as to the importance of this loss mechanism.

The choice of LC again represents a tradeoff between cavity Q and tunability. In the end, we chose to use nematic LC ZLI-3086 ($n_o = 1.5040$, $n_e = 1.6171$ at 589 nm) from Merck. Having more than twice the birefringence of the LC used in the previous chapter, this LC was a significant improvement over the previous LC. Furthermore, this birefringence was critical in obtaining the Q-switching of our lasers. The larger LC birefringence, however, had the drawback of being accompanied (as usual) by higher refractive indices. The simulated Qs of the new cavity at these higher refractive indices were still higher than the older cavity design with the previous LC, which suggested a strong likelihood of achieving lasing after infiltration. In short, the improved cavity design enabled the use of an LC with over twice the birefringence while still maintaining a higher Q than the previous cavity. Lastly,

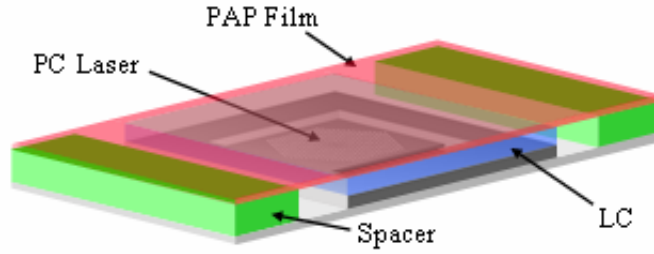


Figure 4.17: Schematic of LC cell constructed around PC lasers. Thickness of LC and PAP films were approximately $5\ \mu\text{m}$, and $31 \pm 1\ \text{nm}$, respectively. Top coverslip is not shown.

another important justification for selecting this particular LC rested in its known ability to be aligned by PAP [101–103], rendering it optically controllable and avoiding the need for electrostatic contacts.

4.4.3 Liquid Crystal Cell Fabrication

The LC cell fabrication procedure was similar to the one specified in the previous chapter. First, the sample along with two spacers was attached to a glass microscope slide with PMMA. Next, a drop of the LC ZLI-3086 was placed on the PC sample and the PAP film/coverslip was glued to the spacers with the PAP film facing towards the LC (see figure 4.17). To improve the imaging of our lasers, the spacers were thinner than in the earlier cells and were sufficiently thick to yield an estimated $5\ \mu\text{m}$ gap between the sample and PAP film.

4.5 Q-Switching of the PC Laser

This section discusses the experimental realization of Q-switched lasers. The section begins with a description of the experimental setup and laser characterization procedure, including the PAP writing procedure employed during the laser characterizations. Next, evidence is presented which supports the conjecture that the LC is aligned by the PAP. The experimental results demonstrating the actual Q-switching are then given. The section concludes with a discussion of the various Q-switching regimes in which the laser cavities can operate.

4.5.1 Experimental Setup and Laser Characterization

The lasers were characterized using the μ PL setup shown in figure 4.18. The vertical orientation of the optical setup enabled the samples to lie horizontally, allowing for the easy incorporation of liquids. The lasers were pumped with 11.7 mW peak power from a semiconductor laser diode at 830 nm with a pulse length of 30 ns and a periodicity of 3.0 μ s.⁸ Pump light was focused onto the sample using a 100x long-working-distance Mitutoyo objective lens and transmitted through the transparent coverslip, PAP film, and the LC onto the PC slab. Emitted light was collected using the same objective lens and was either directed into an OSA to record spectra or into an IR camera for imaging of the mode profiles. A removable polarizer was also used to measure the polarization properties of the emission. A dichroic mirror (reflected visible/transmitted IR) was added to the previous μ PL setup and enabled the PAP to be written and the laser spectra to be recorded simultaneously. Another addition to the setup was a continuous wave 532 nm frequency-doubled Nd:YAG PAP writing laser. The laser was mounted on an X-Y-Z translation stage and a two-dimensional tilt stage. The five degrees of freedom were necessary and sufficient to completely align the PAP writing laser to the pump beam. A CCD was used for imaging purposes, and the CCD was also essential in adjusting the PAP writing laser such that it was coincident with the pump beam at the sample plane.

A new InGaAsP wafer, with a similar design as described in table 3.1, was grown for the Q-switching experiments. Like the previous wafer, this wafer was designed to have an emission maximum at 1550 nm. The emission spectrum is shown in figure 4.19. The improved cavity design resulted in a high success rate for achieving lasing after infiltrating the cavities with liquids. Lasing after infiltration was confirmed by the recording of L-L curves which were indicative of lasing (see figure 4.20). The L-L curves were recorded after infiltrating the cavities with liquids up to a refractive index of 1.5 (a curve acquired after LC infiltration is shown later). The lasing threshold begins at around 1 mW with no infiltration and increases up to nearly 6 mW after infiltration. The increase in threshold is attributed to the increase in losses due

⁸The lasers were pumped far above threshold to eliminate the possibility of Q-switching a laser marginally above threshold with a minor change in cavity Qs. Our goal was to achieve the Q-switching by inducing significant changes in the cavity Qs.

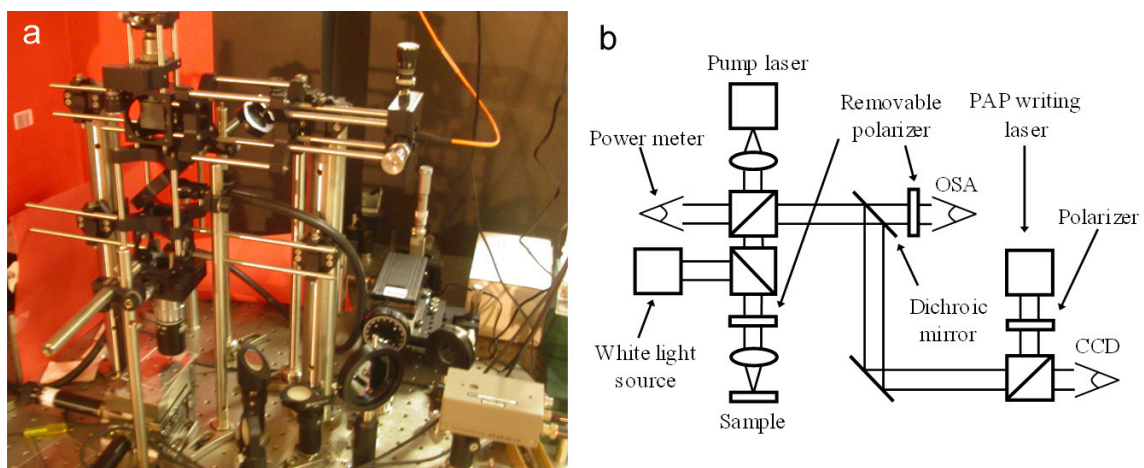


Figure 4.18: Photonic crystal laser μ PL setup. a) Picture of setup. b) Schematic of μ PL setup redesigned for Q-switching project. Light from an 830 nm laser diode was focused onto the PC sample with a 100x objective lens. Emitted laser light was collected by the same objective lens and either was sent to an OSA to record the spectra or into a CCD for imaging. A removable polarizer could be inserted in front of the OSA to interrogate the polarization of the light emitted by the PC laser. A 532 nm PAP writing laser was aligned to be coincident with the pump beam, and a dichroic mirror enabled the PAP writing and laser pumping/spectra recording to occur simultaneously. A polarizer in front of the PAP writing laser was used to control the orientation written into the polymer. Lastly, a removable polarizer could be inserted directly above the objective lens. This polarizer was used to prevent photobleaching of the polymer by the white light required for imaging and locating the sample. This polarizer was always oriented in the same direction to initialize the PAP for all samples equally.

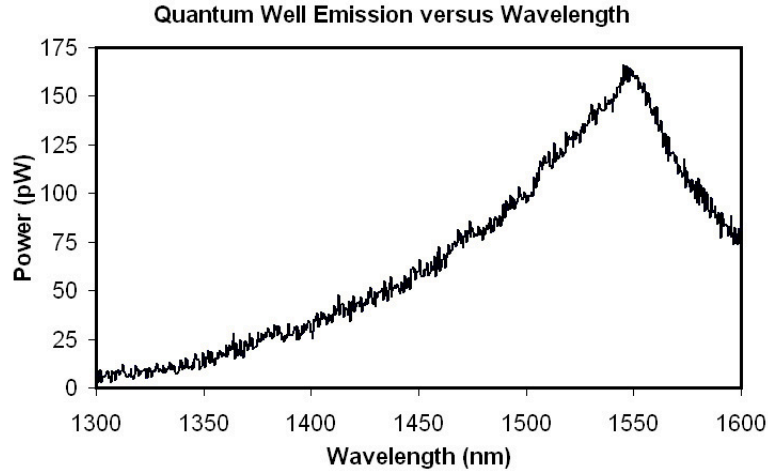


Figure 4.19: Emission spectrum from unprocessed InGaAsP material. The emission drops quickly away from the maximum at 1550 nm.

to decreased vertical confinement. Lasing resonance shifts were also measured as a function of the ambient refractive index (see figure 4.21). The measured tuning rate was approximately 200 nm per unit of ambient refractive index change for the Y polarized mode, which was the same as the estimated FDTD simulated tuning rate.

4.5.2 Photoaddressable Polymer Writing Procedure

The PAP writing procedure and other miscellaneous considerations were as follows. The PAP (and by extension LC) was written using the 532 nm laser in the μ PL setup with an intensity ranging from 6 W/cm² (X polarization) to 12 W/cm² (Y polarization) and a spot size of approximately 11 μ m in diameter. To ensure writing saturation, the PAP was written for intervals of one second, although the onset of tuning was observed even for the shortest writing intervals of approximately 10 ms. The PAP writing time could likely be reduced further with little loss in writing efficiency. The PAP writing occurs during photo-induced isomerization cycles between the *trans* and *cis* conformations of the azo moiety and has an absorption cutoff of approximately 630 nm [94]. The visible absorption cutoff was critical, for it meant the pump beam (830 nm) did not inadvertently write the PAP as well. A low intensity white light was necessary to initially image and locate individual PC laser samples. A removable polarizer oriented along the Y axis was always used with the white light

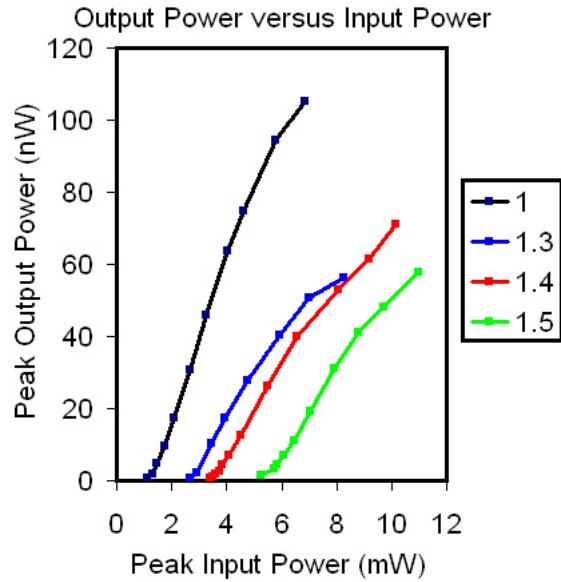


Figure 4.20: L-L curves acquired for the same lasing resonance after infiltrating with several index-matched fluids. The lasing threshold starts at around 1 mW before infiltration and rises to nearly 6 mW as the ambient refractive index increases to 1.5.

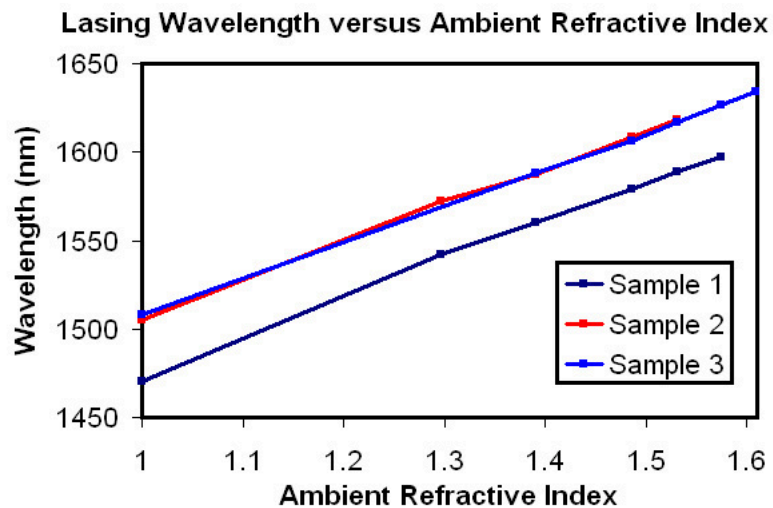


Figure 4.21: Lasing wavelengths recorded for the Y polarized mode from three samples as a function of ambient refractive index. The tuning rate for all samples is approximately 200 nm per unit of ambient refractive index change.

to prevent photobleaching and to initialize the PAP to the same orientation for the subsequent laser characterization.

4.5.3 Verification of PAP Aligning LC

Polarization interference microscopy provided evidence of the LC aligning parallel to the PAP and of the PAP orienting as a result of the green writing laser. By referring to the Michel-Levy diagram (see figure 4.22), the PIM images suggested the LC in the cell may have been homogeneously oriented (see figure 4.23), though we can not be certain due to the false coloration introduced by the light passing through the red PAP layer. As mentioned earlier, the PAP is believed to have a planar orientation after being spun on the substrate [97]. Assuming for the moment the LC was in fact aligning parallel to the PAP [101–103], then the bulk LC should have followed the PAP’s orientation and also be aligned homogeneously. A photobleaching experiment was implemented to try and determine the extent to which the LC aligned parallel to the PAP. For this purpose an unpolarized dim white light was shone onto the PAP and LC cell. If the LC followed the PAP orientation, then as the polymer photobleached and aligned vertically, the LC should have also aligned vertically. Images taken of the photobleaching show the LC slowly aligning vertically over a period of a couple minutes (see figure 4.24 (a)-(d) and external movie file QswitchedPCPIMmovie.mov). Similarly, another photobleaching experiment was conducted by shining unpolarized white light through a photomask placed on top of a PAP film. As figure 4.24 (e)-(f) shows, the mask patterns were transferred into the PAP film and aligned the LC vertically where the PAP was bleached. No individual piece of evidence conclusively proved that the LC exhibited planar alignment in the cell and that it aligned parallel to the PAP, but all of the individual pieces of evidence, including the results in the literature, taken as a whole, overwhelmingly supported these conjectures [101–103]. Lastly, PIM also showed that the writing laser did in fact write the PAP. Figure 4.25 shows images taken after exposing the polymer with the green laser. In the first image, the laser spot including the diffraction rings can clearly be seen in the polymer. In the second, the sample was quickly translated during exposure and demonstrated the polymer could be written with extremely brief exposures.

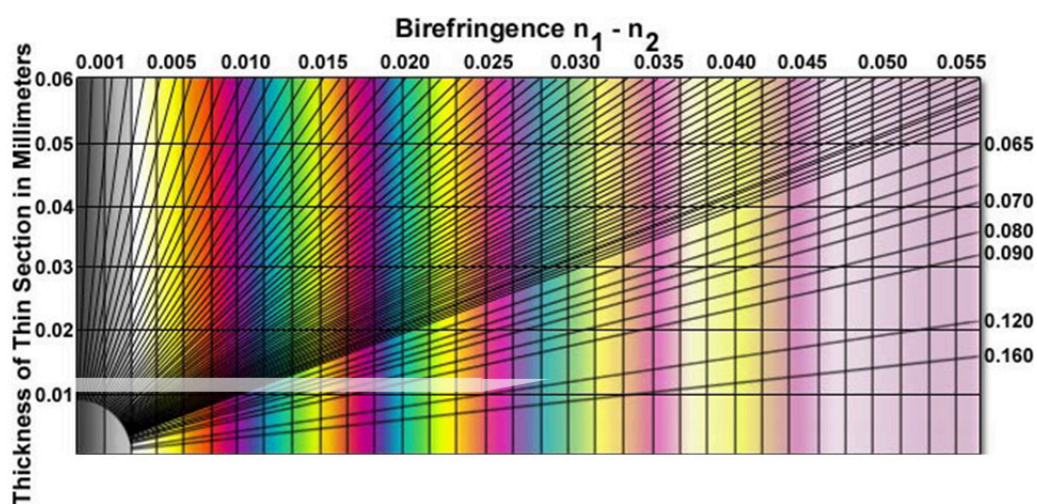


Figure 4.22: Michel-Levy chart showing the possible colors accessible given the LC's birefringence (~ 0.11) and thickness ($\sim 5.0 \mu\text{m}$), keeping in mind the PIM images were created by light traversing the LC cell twice.

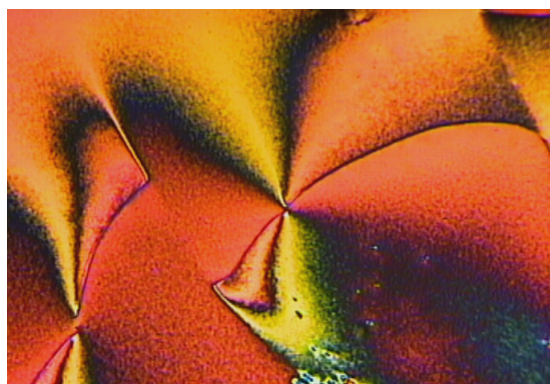


Figure 4.23: Polarization interference microscopy image of LC cell in contact with a PAP film. Due to the absorption of the PAP, red light was preferentially transmitted and distorted the coloration of the PIM image. Although this limited the usefulness of the image in determining the LC orientation, at the very least the interference pattern revealed the LC was not completely homeotropically aligned. The LC orientation in the center of the PIM image appears to be dominated by a disclination defect.

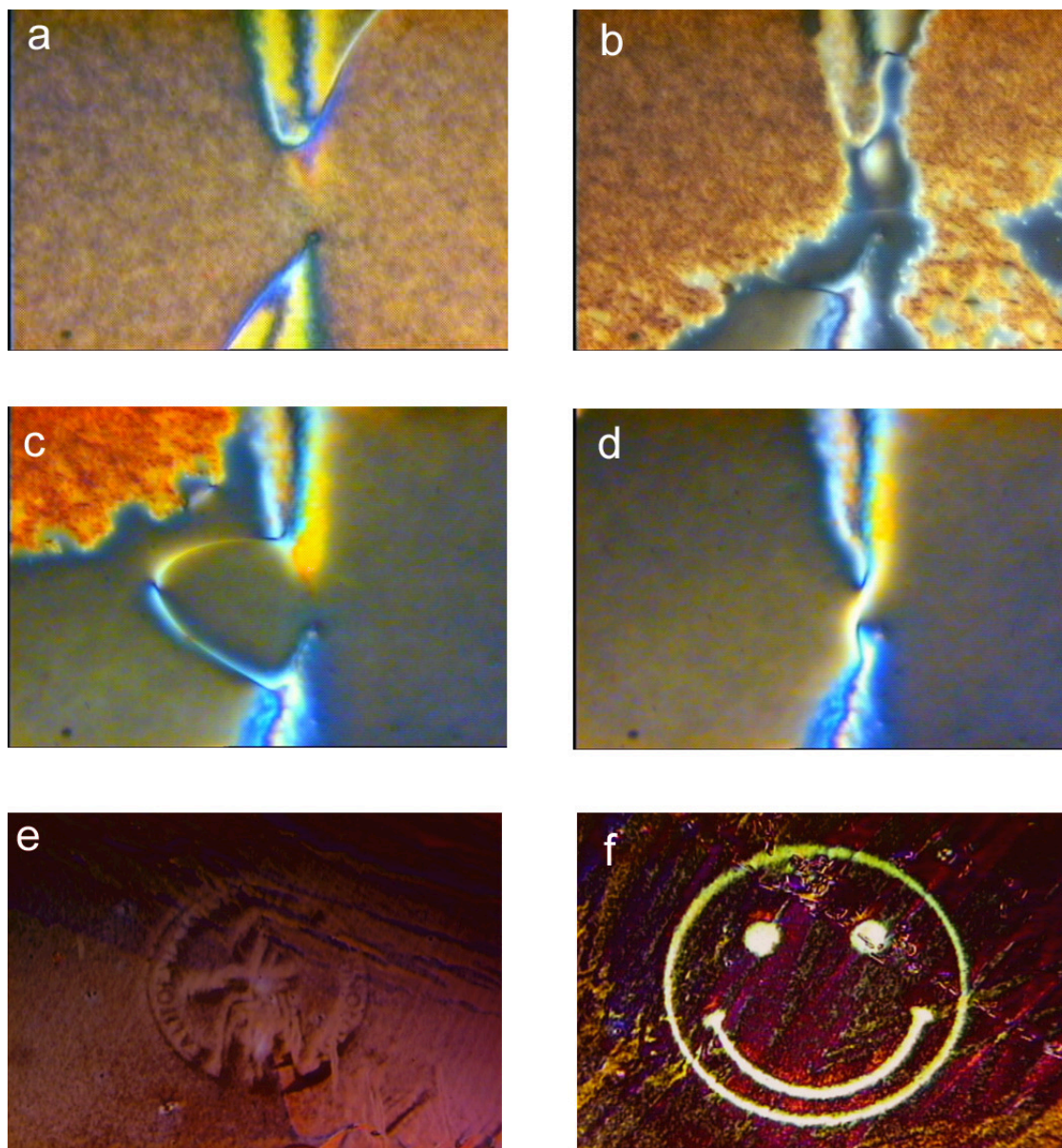


Figure 4.24: Polarization interference microscopy images of PAP films demonstrating photobleaching. (a)-(d) This sequence of images was taken while illuminating a PAP film comprising one side of a LC-filled cell with dim unpolarized white light. (a) Initially the LC exhibited some degree of planar orientation but oriented out-of-plane as the PAP photobleached (b)-(d). The black images indicate the LC was primarily oriented homeotropically, in the same direction as the PAP. The white arc in (c) and line in (d) connecting the two defects at the top and bottom is believed to be the interface between two LC domains. (e)-(f) These PIM images were taken with the same conditions as in (a)-(d), except now the unpolarized white light photobleaching the PAP was transmitted through a photomask. The patterns written are (e) the Caltech emblem and (f) a “smiley” face.

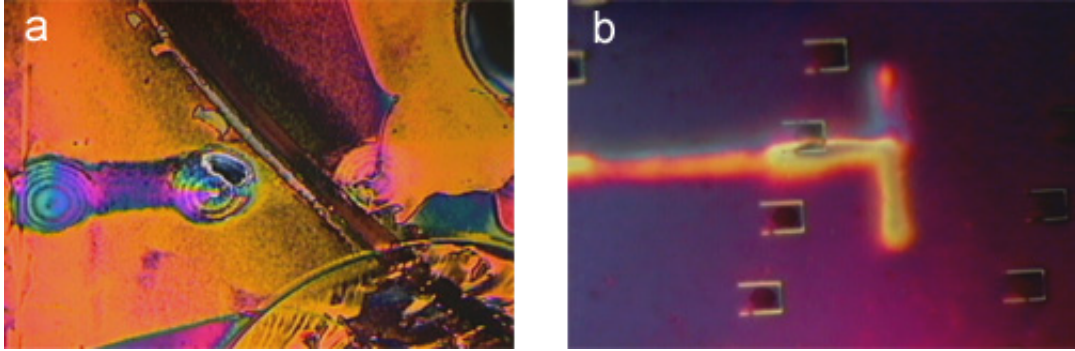


Figure 4.25: Polarization interference microscopy images of PAP films written using the PL setup. These images were taken by illuminating a PAP film comprising one side of a LC-filled cell with the 532 nm green laser in the PL setup shown in figure 4.18. (a) The writing laser was focused on one spot for several seconds and moved to another spot. The diffraction rings of the laser can clearly be seen in the PIM image. (b) The writing laser was quickly translated across the PAP film in the vicinity of PC lasers. Even though the exposure time was short ($\ll 1$ second), the PAP appeared to still have been written.

4.5.4 Q-Switching Results

Lasing spectra were recorded by optical pumping of the PC cavities while systematically varying the LC orientation in the top cladding layer via the PAP layer. The PAP orientation was controlled by illuminating the PC laser with polarized 532 nm light from a frequency-doubled Nd:YAG laser. As the PAP oriented itself orthogonally with respect to the writing laser polarization, the LC molecules were in turn oriented parallel to the polymer layer (see figure 4.26). Immediately after spin-coating, the PAP possessed a planar orientation [97] but invariably underwent photobleaching [96] as it was repeatedly written throughout the measurement process. A typical measurement cycle consisted of first locating the sample to be tested with low intensity white light. A polarizer was inserted during this stage to prevent photobleaching and to initialize the PAP to a known state. Next, the PAP orientation was adjusted with the green laser and the PC cavity was then optically pumped with the near-IR laser diode. The laser spectra were then recorded with an OSA.

L-L curves for a cavity which supports two high-Q lasing modes after LC infiltration are shown in figure 4.27. These L-L curves were taken using the same cavity as the one in the Q-switching experiment discussed below. The curves for each mode were taken with the PAP/LC optimized for that mode. Furthermore, the pump position was set to equalize the output from each (optimized) mode at a particular

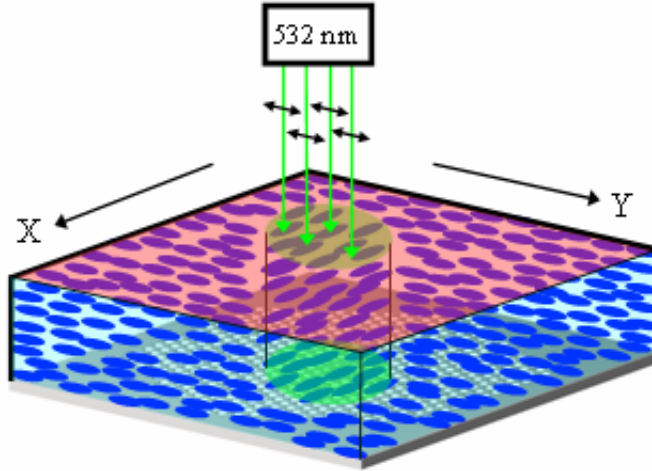


Figure 4.26: Schematic representation of the LC reorientation via PAP photoinduced alignment. The PAP oriented itself orthogonally (along X axis) with respect to the writing laser polarization direction (Y axis), which in turn induced a similar alignment in the LC.

pump power. Spectra recorded using the same cavity are shown in figures 4.28 and 4.29. Figure 4.28 reveals the polarization nature of the lasing modes. The spectra were recorded using a polarizer rotated at various orientations and indicate that the modes were orthogonally and linearly polarized, in agreement with the FDTD simulations. After verifying the polarization properties, we were now able to implement the Q-switching strategy. Figure 4.29 shows spectra taken with no polarizer and with several different PAP orientations. Initially the PAP was aligned along the Y axis. As the PAP's orientation was rotated from the Y to the X axis, the LC in contact with the PAP underwent the same rotation, and this realignment propagated through the bulk LC in the cladding layer above the laser cavity. Due to the cavity modes' orthogonality, as the LC was rotated from the Y axis to the X axis, one cavity mode experienced a maximum cladding index (n_e) whereas the other mode experienced a minimum in the refractive index (n_o). As the refractive index of one mode increased, its lasing wavelength red-shifted and its Q decreased until the lasing was quenched by a combination of increased losses and gain competition with the other mode. Conversely, the orthogonal mode's resonance blue-shifted and its Q increased until that mode was driven above threshold and started lasing. Thus, rotating the LC switched the laser output from one polarized mode to the other. This switching between lasing cavity modes effectively amplified control over the spectral emission range of the cav-

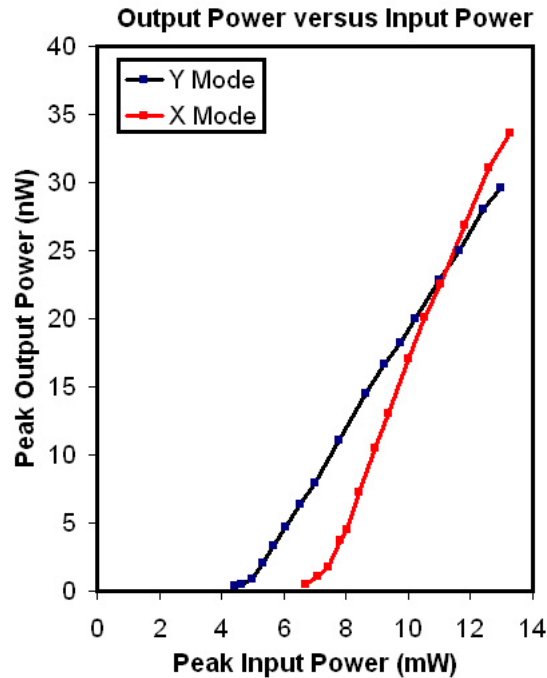


Figure 4.27: L-L curves taken for cavity supporting two high-Q cavity modes after LC infiltration. The LC orientation was optimized for each cavity mode before that mode's curve was acquired. The pump position was chosen such that the two modes had roughly equal output powers when each was optimized and pumped at the power level at which the Q-switching experiments were conducted. This explains why the two modes' curves cross even though they have different thresholds. The specifically chosen pumping position results in different perceived differential quantum efficiencies (e.g., through different pumping, coupling, and collection efficiencies) for the two modes, which leads to the different slopes and the ultimate crossing of the curves.

ity far beyond what would be possible by tuning the effective cavity path length of a single mode. The switching in the PC lasers was both reversible and reproducible as supported by many switching cycles with little loss in fidelity.

Unlike the PC lasers discussed in the previous chapter, the vast majority ($\sim 90\%$) of devices based on the new cavity design lased after LC infiltration. This turned out to be crucial because of the improbability of finding a device with the appropriate characteristics to yield good Q-switching behavior. For instance, not only did a device need to have the two dipole modes lase, but they also *both* needed to switch when the LC was rotated. Furthermore, the resonances needed to be closely spaced so that high resolution spectra could be simultaneously recorded for both resonances during the switching process. In the end, locating a device which satisfied all of these criteria was difficult and ultimately required the manual characterization of approximately

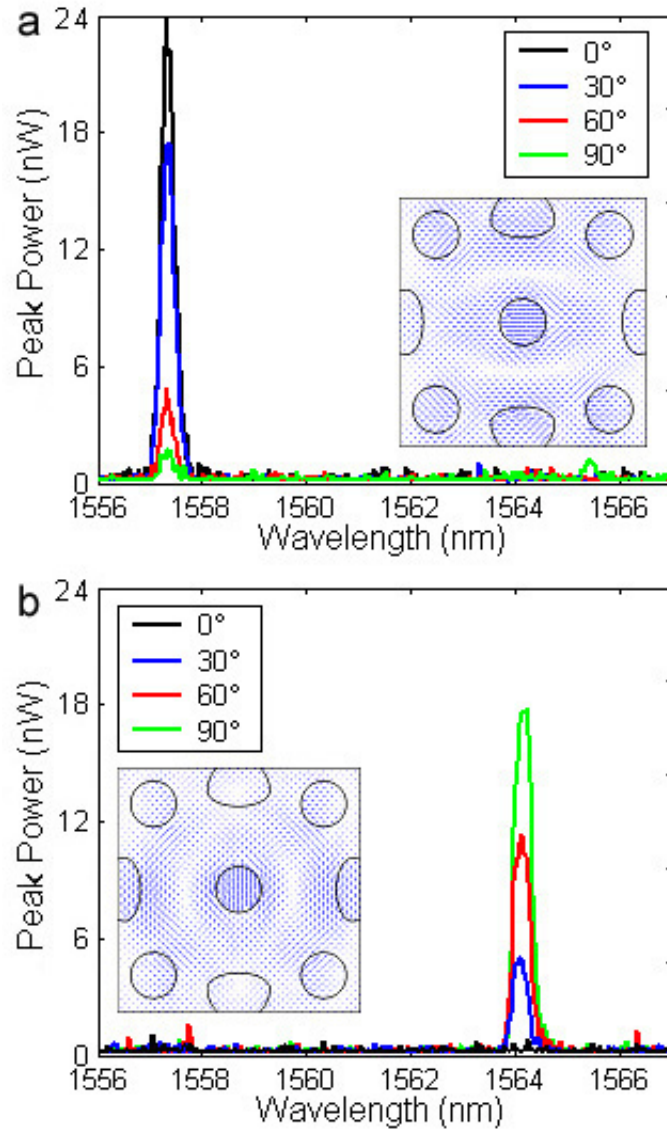


Figure 4.28: Confirmation of orthogonally polarized lasing modes. (a) The laser spectra was taken with PAP/LC aligned with the Y axis, and the collected light was passed through a polarizer oriented at various angles. The collected power was maximized with the polarizer oriented at 0° (X axis) and minimized at 90° (Y axis), which indicated the resonance was the X polarized dipole mode. (b) The laser spectra taken with the same conditions as in (a) but with the PAP/LC aligned with the X axis. The collected power was maximized with the polarizer oriented at 90° (Y axis) and minimized at 0° (X axis), which indicated the resonance was the Y polarized dipole mode. For clarity, figure 4.12 is reproduced as insets to (a) and (b) and shows the simulated cavity mode polarization profiles.

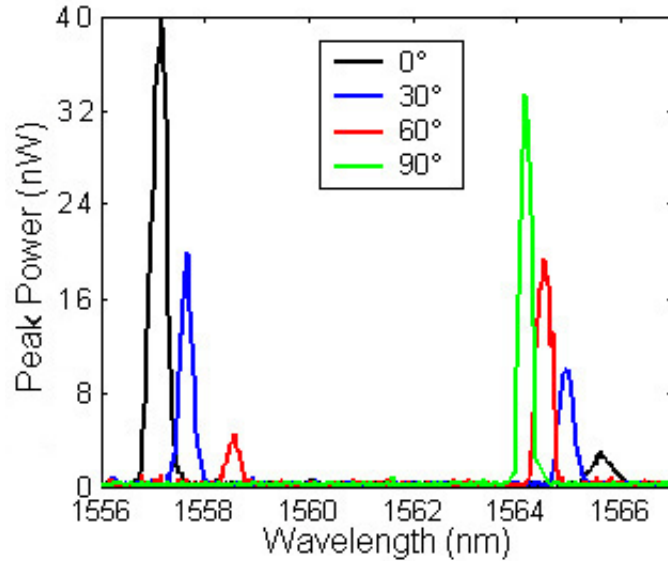


Figure 4.29: Experimental realization of Q-switching. The laser spectra was taken after the PAP writing laser aligned the PAP/LC at several orientations. After writing at 0° (PAP writing laser polarized along X axis which caused PAP/LC to orient along Y axis), emission was maximized for the X polarized mode and minimized for the Y polarized mode. As the PAP writing laser polarization was rotated towards 90° , the cladding refractive index for the X mode increased, raising losses until the lasing was quenched and emission terminated. Meanwhile, the Y mode experienced a decreasing refractive index, which lowered cavity losses and drove the mode above threshold and lased.

4000 devices.

4.5.5 Q-Switching Regimes

The previous discussion pertaining to the device requirements alludes to the possibility of different Q-switching (or no switching) regimes. Before we discuss the multitude of possible switching scenarios, we will first briefly discuss how the modes interact with each other. Although the modes do not have identical spatial field distributions, they do overlap in the semiconductor slab (see figure 4.30) and therefore compete with each other for photons emitted by the quantum wells. This competition (or decreased gain) raises the thresholds of both modes than they would otherwise be if only one mode existed. Although this interaction between the modes may play a role in some Q-switching scenarios, possibilities do exist where the Q-switching still occurs with essentially no interaction between the cavity modes.

Keeping in mind that Q-switching is implemented through a combination of tuning the relative Qs of cavity modes and gain competition between the modes, several

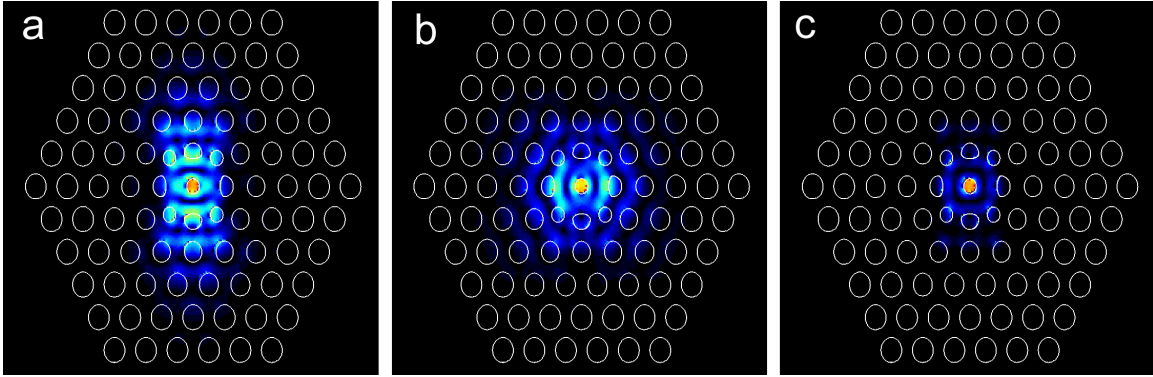


Figure 4.30: Simulation of modal field overlap. Electric field magnitude for (a) X dipole and (b) Y dipole modes. The overlap of the two modes is visualized by plotting the product of the two field magnitudes (c). The modal overlap within the quantum well material is a source of the gain competition the two modes experience.

scenarios can be envisioned. The scenarios discussed below only include the ones where both modes can lase under certain conditions, albeit not necessarily simultaneously. For added clarity, figure 4.31 shows the different Q-switching regimes as a function of cavity mode Qs, and table 4.2 summarizes the most significant aspects about each one. The discussion of the different regimes progresses from regimes with the highest mode Qs to the regimes with the lowest Qs where possible. The first (I) and rather uninteresting regime consists of both modes exhibiting a sufficiently high innate cavity Q such that they both lase regardless of the LC orientation. Obviously, no switching behavior is possible and nothing interesting can be observed in this case. A slightly more interesting scenario (II) is where only one mode always lases whereas the second mode is quenched for some LC orientations. In this scenario, the lower-Q mode can be observed to quench by rotating the LC. Due to gain competition with the higher-Q mode, the lower-Q mode is quenched with loss levels lower than they would be in the case if the other mode did not exist.

More interesting scenarios include the following three where both cavity modes exhibit intermediate Qs such that they both can be quenched given certain LC orientations. First, we consider the case (III) where there exists an intermediate LC orientation such that both modes lase but each mode can still be quenched when the LC is oriented at one of the extrema.⁹ Again due to gain competition, the net effect

⁹For example, one mode is quenched when the LC is oriented along the X axis and the other mode is quenched when the LC is oriented along the Y axis.

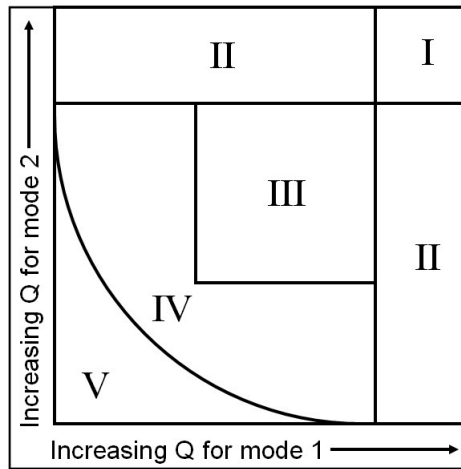


Figure 4.31: Schematic of Q-switching regimes. This figure shows the qualitative relationship between the Q-switching regime in which a cavity operates and the Qs of the two modes supported by the cavity. The labeling of the regimes are consistent with those discussed in the text and in table 4.2. The borders between the various regimes are drawn figuratively and are not meant to be taken literally.

Q-switching regime	Description	Experimental signatures
I	Both modes lase regardless of LC orientation	No significant signature
II	One mode always lases; second mode is quenched for some LC orientations	Second mode is quenched at lower loss levels due to gain competition with first mode
III	Both modes can simultaneously lase but LC orientations exist that quench each mode	Each mode is quenched at lower loss levels due to gain competition with the other mode
IV	Both modes can lase but the onset of lasing of one mode coincides with the quenching of the other	The LC orientation corresponding to the modes' onset of lasing and quenching exhibits hysteresis due to additional (field-enhanced) gain enjoyed by the currently lasing mode
V	Both modes can lase but never simultaneously	No significant signature

Table 4.2: Classification of various Q-switching regimes and their experimental signatures.

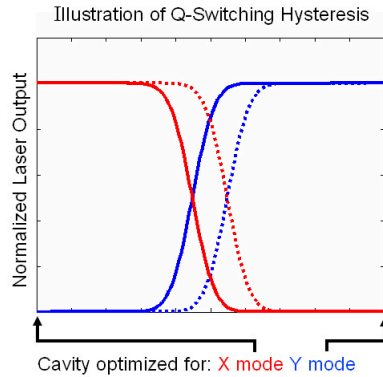


Figure 4.32: Illustration of possible Q-switching hysteresis. For cavities operating in regime IV (see 4.31 and table 4.2), the onset of lasing in one mode coincides with the quenching of the other mode. Such cavities may exhibit hysteresis as shown in the above plot. For instance, let the cavity be initially optimized for the X mode (i.e., LC oriented along Y axis). The lasing output is originally due to the X mode but eventually switches to the Y mode as the cavity is smoothly modified and optimized for the Y mode (dotted curves). Now, as the cavity optimization is reversed (solid lines) the output switches back to the X mode, but the transition occurs at a different degree of optimization (i.e., LC orientation) than the previous transition. This proposed hysteresis is believed to be possible because of the gain competition between the modes. The lasing mode derives extra gain due to the field enhancement and so can remain lasing at higher loss levels than is required for it to initially lase.

is that each mode is quenched at loss levels lower than it would otherwise be in the case if the other mode did not exist. Perhaps the most interesting regime (IV) is where the onset of lasing for one mode coincides with the quenching of the other and vice versa. In this regime, the LC orientation corresponding to the switching is not a constant but rather demonstrates path dependence. This path dependence is due to the extra gain a lasing mode derives from optical field enhancement [15]. With the extra gain captured by the lasing mode, that mode will quench at a higher loss level than the loss level at which it begins lasing due to the competition with the other mode. Experimentally this should be observed as a hysteresis in the switching orientation (see figure 4.32). The last scenario (V) occurs when both cavity modes have even lower Qs and can both lase given an optimal LC orientation, but no orientation exists such that simultaneous lasing occurs. In this case, the Q switching still occurs but the presence of one mode does not significantly affect the other.

The Q-switching regime in which a laser is operated is not entirely dependent upon the innate cavity mode Qs, but may also be influenced by pump beam parameters. For example, increasing the pump power (e.g., increasing power, duty cycle,

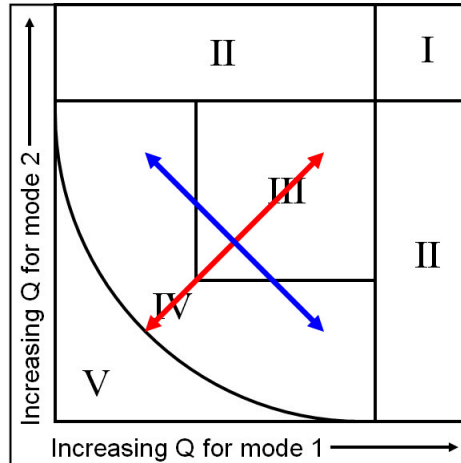


Figure 4.33: Schematic showing how adjusting the pumping parameters for PC lasers influence the Q-switching regime in which the cavity operates. The red line indicates the control obtained by varying the pump power. The lasers' pump power affects the gain for both modes equally, and its effect is represented by artificially changing (increasing or decreasing) the cavity Qs. The blue line indicates the control obtained by the positioning of the pump beam. The pump position affects the coupling efficiency of the light emitted by the quantum well material into the cavity modes and is represented by artificially changing (increasing or decreasing) the cavity Qs. Although the pump position can be used to impact both modes equally, changing the pump position is most effective for favoring one mode over the other (which is why the blue line is drawn orthogonal to the red). Therefore, adjusting both the pump power and position in concert is an effective method of controlling a cavity's Q-switching regime.

frequency of pulses, etc.) can initially increase the gain of both modes until the laser is pumped and heated to the point of increasing non-radiative Auger recombination [104–106] losses that balance any further gain. Increasing the pump power beyond this point will decrease the gain for both cavity modes. Another method of actively influencing the switching regime is to change the pump location on the sample. By pumping the cavity away from its symmetry axes, the two modes' relative pumping and coupling efficiencies can be controlled. The combination of these two methods provides the experimentalist with significant latitude in operating the lasers in the Q-switching regime of interest. Figure 4.33 is a modified version of figure 4.31 and schematically shows how changing the pumping parameters can influence a laser cavity's Q-switching regime.

4.6 Electrical Implementation of Q-Switching

While working on the optically triggered Q-switched PC laser utilizing PAP to align the LC, a more traditional implementation was also investigated where advanced electrodes for generating electric fields were used to align the LC. Although the PAP method was ultimately successful and the electrically triggered scheme never tested, most of the processing steps were optimized and are included here for completeness. First of all, to implement the Q-switching the LC in the top cladding layer must be able to reversibly rotate by 90° . This control can be achieved with two pairs of electrodes deposited on top of the PC (see figure 4.9). By adjusting the relative voltage across the electrode pairs, the LC can be rotated as required within the plane of the PC. The primary challenge to fabricating the two electrode pairs is the requirement they be electrically isolated from the semiconducting wafer and also from each other, given the restriction of planar fabrication processing. A collection of 4 masks (2 electrode and 2 isolation layers) were devised for a multilayered lithography process to achieve the proper electrode configuration and electrical isolation. Photo-sensitive polyimide was investigated for use as definable dielectric layers to isolate the electrodes. The electrode fabrication sequence begins with a completely processed PC laser sample and then as follows: define first polyimide isolation layer and cure, define the first electrode pattern, evaporate electrodes and do lift-off, define second polyimide isolation layer and cure, define the second electrode pattern, evaporate electrodes and do lift-off, and wirebond the pads. A schematic of the fabrication steps and the mask layouts are shown in figure 4.34 and 4.35. The electrodes were designed to connect many devices simultaneously. The number of parallel connections is a compromise between connecting too many devices and risking a short ruining the entire sample and connecting too few devices which causes laborious wire bonding and testing.

The photo-sensitive polyimide (PI2723 from HD Microsystems¹⁰) was chosen because it eliminated processing steps by serving both as a dielectric layer and as a photoresist for patterning. The processing procedure for the polyimide films involves first thinning the polyimide (T9039) and spinning the resist on the sample. The final

¹⁰All of the polyimide processing chemicals are from HD Microsystems.

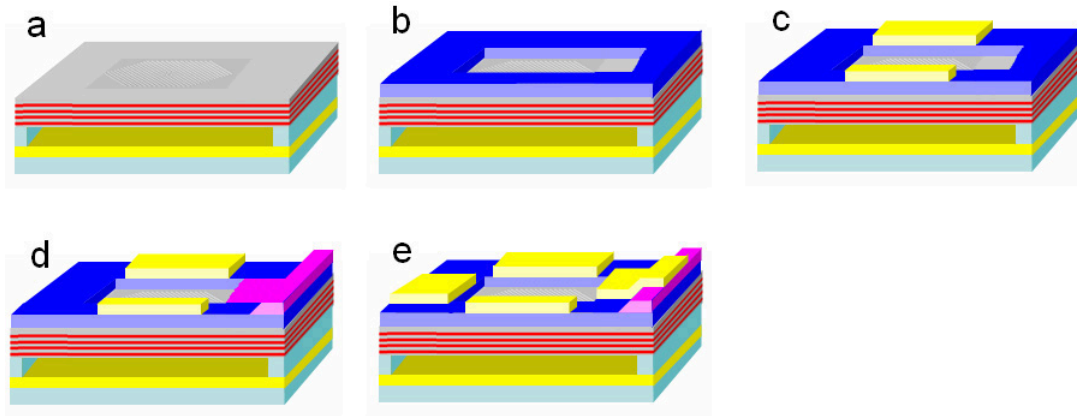


Figure 4.34: Schematic illustrating electrode fabrication procedure with polyimide isolation layers. (a) The process begins with a fully fabricated PC sample. (b) The first polyimide dielectric layer is patterned around the PC lasers and cured. (c) Next, the first electrode mask pattern is transferred into photoresist (not shown) on top of the polyimide layer. Electrodes are then evaporated and the remaining photoresist dissolved using standard lift-off processing techniques. The first electrode mask contains the 2 electrodes required to make the first electrode pair. (d) Next, the second polyimide isolation layer is patterned and cured. (e) Lastly, the second electrode mask is then used with another lift-off process to create the second pair of electrodes. Note that two of the electrodes are wired together so both pairs share a common ground. The second polyimide layer serves to isolate the electrodes from the previous ones (where appropriate). The positive slope of the polyimide film means the electrodes can be evaporated on top of both cured polyimide layers simultaneously and remain contiguous (e). Consequently, the second pair of electrodes are evaporated onto the same level as the first around the PC, as required to generate the planar electric fields needed for the Q-switching implementation. By studying the polyimide and electrode masks shown in figure 4.35, one can see how the various layers fit together to create the electrode structure schematically shown in (e).

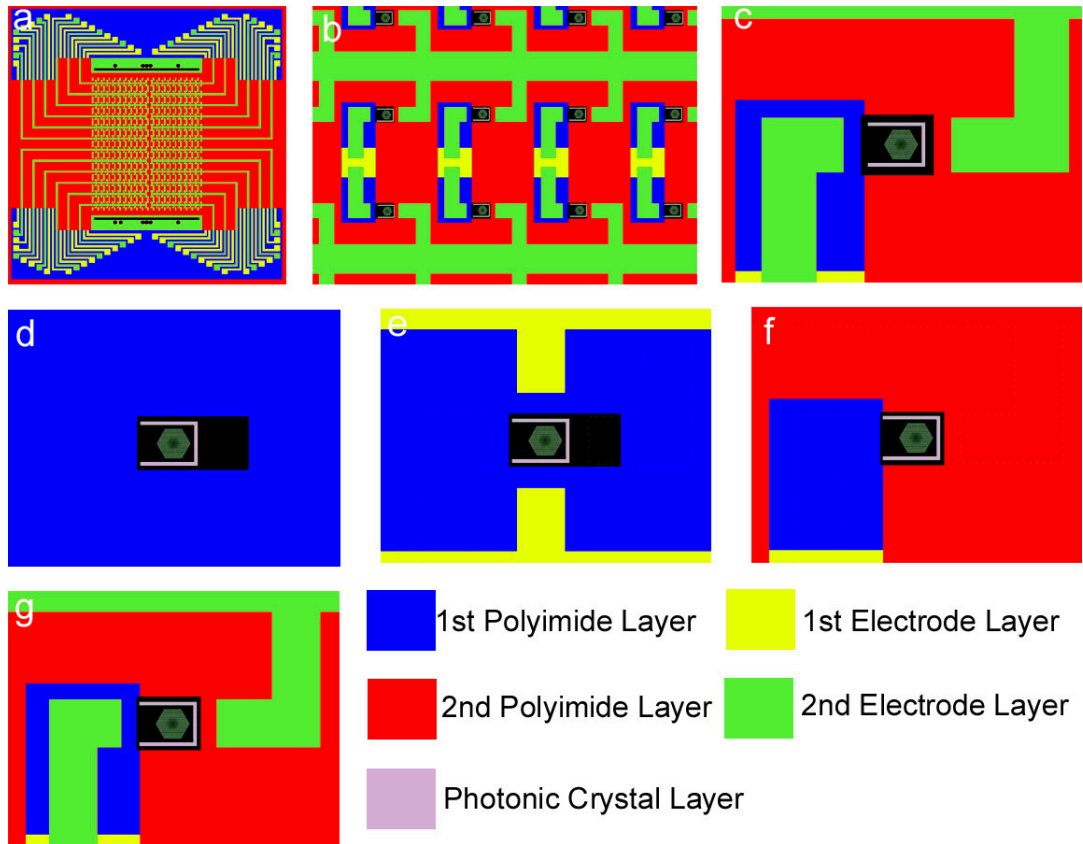


Figure 4.35: Schematic of masks for electrode fabrication. (a) The full mask plates with all the mask layers superimposed on each other. The PCs are in the middle of the masks and the electrode leads extend outward to the wirebonding pads around the perimeter. (b) A close-up showing the mask layers surrounding several PCs. (c) A close-up showing the detailed electrode structure around a single PC cavity. (d)-(g) This sequence of images shows the electrode and isolation layer progression around a single PC. The first mask (d) defines the initial polyimide layer used to isolate the electrodes from the PC semiconductor slab. The second mask (e) produces the first set of electrodes. The third mask (f) defines the second isolation layer that primarily isolates the two electrode layers from each other. The fourth mask (g) patterns the second set of electrodes around the PC. Note the two sets of electrodes have a common ground.

(post-cure) film thickness can be controlled by adjusting the thinner concentration and spinning RPM. Films as thin as 200 nm are allegedly possible, but the thinnest we ever obtained was 500 nm (5 mL polyimide, 1.5 mL thinner, 10,000 RPM). The following processing parameters are for the same polyimide concentration but spun at 5000 RPM. The resist is soft baked at 75°C for 4 minutes, exposed for 20 seconds, immersed in pure developer (DE6180) for 15 seconds, then half-developer and half-rinse (R19180) for 7 seconds, and then pure rinse for 20 seconds. The polyimide is then cured in a tube furnace by ramping the temperature to 300°C in air for 25 minutes, then to 350°C in nitrogen for 10 minutes, and then cooled in nitrogen to room temperature. The curing shrinks the film thickness by about half and transforms the polyimide into a very robust, chemically inert material which can survive further processing steps. A negative photoresist is preferable for the electrode lift-off process because it is easier for alignment. The negative resist used in the ring resonator fabrication procedure (chapter 2) can be used but a thicker resist is preferable (see below).

All of the processing steps were successfully implemented on InP test wafers with the exception of the final wirebond step. A concern with wirebonding is that the heat generated during the bonding process may cause the gold pads to delaminate from the polyimide. A potential solution to this problem (if it occurs) is to evaporate thick pads. To this end, specialized lift-off resists (LOR) from MicroChem were considered. These resists can easily be spun to thicknesses of at least 6 μm . Lastly, a potential problem which may arise when using actual undercut PC samples is that the fragile membranes may collapse during the multiple spinning steps. This can be circumvented by either designing more robust suspended structures (see figure 4.36) or by not undercutting the PC structure with HCl until after the electrodes are deposited. Polyimide is impermeable to HCl and so should be minimally affected by the undercutting step.

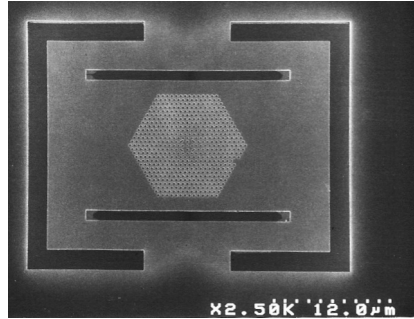


Figure 4.36: Scanning electron micrograph of a PC sample with redesigned etch guides. The modified etch guides are designed to make the sample more resilient to multiple spin processing steps as compared to original “peninsula design” (see figure 4.10).

4.7 Discussion and Conclusion

The tuning of each individual cavity resonance seen in figure 4.29 (X polarized ~ 1.4 nm, Y polarized ~ 1.5 nm) is attributed to changes in the effective optical path lengths experienced by the cavity modes due to the rotating LC (analogous to the tuning achieved in the electrical tuning method discussed in the previous chapter). Given the magnitude of the resonance shifts, FDTD computer simulations suggest that only the LC in the top cladding layer follows the PAP orientation. The LC in the PC holes experiences relatively strong surface anchoring, which inhibits the cladding LC orientation from propagating into the PC holes [20, 77]. As mentioned previously, one possibility for circumventing this limitation in the future is to eliminate the LC and instead infiltrate the PC with the PAP itself. Infiltrating directly with the PAP may overcome the surface anchoring effects present within the confined geometries of PC holes because the underlying alignment mechanism for PAP (photo-induced isomerization cycles) is fundamentally different than for LC. The ability to control the orientation of PAP, LC, or some other birefringent material in the holes of a PC would not only significantly increase optical-path-length-based tuning, but could also enable more sophisticated switching behavior in PC cavities supporting more modes by increasing the selectivity between the modes. As the number of modes a cavity supports is increased, the ability to discriminate between them using their polarization structure diminishes. Controlling the orientation of the infiltrated birefringent material within the PC holes or simply using materials with increased birefringence

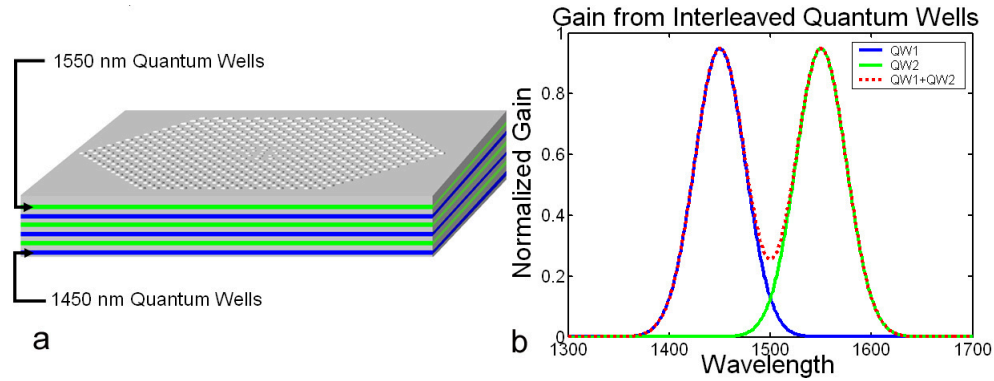


Figure 4.37: Schematic and gain spectra for proposed interleaved quantum well structure. a) Schematic showing a PC constructed from a slab containing an interleaved quantum well structure with one set of quantum wells optimized for emission at 1450 nm and the other at 1550 nm. b) An illustrative plot of the proposed quantum well gain spectra. Each set of quantum wells contributes one peak to the gain spectra and the peaks are arbitrarily separated by 100 nm. Gaussian distributions are used to represent the individual gain spectra peaks and are chosen merely for illustrative purposes.

can potentially compensate for this and enable more complex switching in the lasers.

One characteristic of the Q-switching technique is that it largely decouples the control over the range of emission wavelengths from the birefringence of the infiltrated material. Consequently, the wavelength switching range of the PC laser is not limited by the birefringence of the infiltrated material, but ultimately may be limited by the quantum well gain spectra. Future enhancements in the quantum well structure and cavity design can potentially further increase the wavelength switching range far beyond the observed 7 nm. Lasing after LC infiltration requires maximal gain and minimal loss, and both lasing modes are observed close to 1.55 μm , the engineered maximum of the quantum well emission. If the grown quantum well structure is redesigned to exhibit two distinct maxima in the gain spectra and if the orthogonally polarized PC cavity modes can be designed to coincide with these gain maxima, then the laser emission can, in principle, be switched over a considerably larger wavelength range and may exceed 100 nm (see figure 4.37).

Beyond increasing the wavelength range over which the lasers can be switched, future studies can investigate temporal stability of the switching process. Keeping in mind the PAP and LC switching timescales are orders of magnitude longer than the pumping cycles, such studies are confined to investigating slowly evolving phenomena. One possibility includes using an electrically pumped lasing cavity's intense optical

field to align either the LC or the PAP. The lasing field will preferentially align the LC to favor an orthogonally polarized mode. This may potentially lead to self-oscillation of the cavity and spontaneously switch the laser emission between the multiple cavity modes. On the other hand, infiltrating a PC laser with a PAP that can be aligned by the light emitted by the laser could lead to a stabilizing effect. The PAP would align in such a way as to favor the dominant cavity mode, thereby stabilizing that mode at the expense of the other cavity modes.

The integration of nanophotonics with birefringent nonlinear materials enables the complete utilization of polarization as a degree of freedom and may form the basis of future integrated opto-fluidic systems. In particular, the Q-switched PC lasers may potentially fulfill a variety of scientific and technological needs. For example, the lasers can serve as polarization sensitive optically triggered switches within optical information processing architectures. Furthermore, since the PAP orientation is stable, no external energy or input, such as an electrostatic field, is required for the laser to maintain its lasing wavelength and polarization. Liquid crystal PC laser arrays can also serve as an optical re-programmable read-only memory elements. More significantly, the successful integration of LC and PAP (itself a material with enormous potential with photonics integration [91, 96]) in the creation of the Q-switched PC laser illuminates the extraordinary design freedom and capabilities of PC cavities and further demonstrates the full potential of integrating semiconductor nanophotonics with nonlinear optical fluids and polymers.

Bibliography

- [1] K. Vahala, "Optical microcavities," *Nature* **424**, 839-846 (2003).
- [2] A. Yariv, *Optical Electronics in Modern Communications* (Oxford University Press, New York, 1997).
- [3] S. M. Spillane, T. J. Kippenberg, and K. J. Vahala, "Ultralow-threshold Raman laser using a spherical dielectric microcavity," **415**, 621-623 (2002).
- [4] D. K. Armani, T. J. Kippenberg, S. M. Spillane, and K. J. Vahala, "Ultra-high-Q toroid microcavity on a chip," **421**, 925-928 (2003).
- [5] D. Rafizadeh, J. P. Zhang, R. C. Tiberio, and S. T. Ho, "Propagation loss measurements in semiconductor microcavity ring and disk resonators," *J. Lightwave Technol.* **16**, 1308-1314 (1998).
- [6] D. Rafizadeh, J. P. Zhang, S. C. Hagness, A. Taflove, K. A. Stair, S. T. Ho, and R. C. Tiberio, "Waveguide-coupled AlGaAs/GaAs microcavity ring and disk resonators with high finesse and 21.6-nm free spectral range," *Opt. Lett.* **22**, 1244-1246 (1997).
- [7] M. Cai, O. Painter, K. J. Vahala, and P. C. Sercel, "Fiber-coupled microsphere laser," *Opt. Lett.* **25**, 1430-1432 (2000).
- [8] E. Krioukov, J. Greve, and C. Otto, "Performance of integrated optical microcavities for refractive index and fluorescence sensing," *Sens. Actuators B* **90**, 58-67 (2003).
- [9] E. Krioukov, D. J. W. Klunder, A. Driessen, J. Greve, and C. Otto, "Sensor based on an integrated optical microcavity," *Opt. Lett.* **27**, 512-514 (2002).

- [10] K. Oda, N. Takato, and H. Toba, "A wide-FSR waveguide double-ring resonator for optical FDM transmission systems," *J. Lightwave Technol.* **9**, 728-736 (1991).
- [11] B. E. Little, S. T. Chu, H. A. Haus, J. Foresi, and J.-P. Laine, "Microring resonator channel dropping filters," *J. Lightwave Technol.* **15**, 998-1005 (1997).
- [12] M. Loncar, A. Scherer, and Y. Qiu, "Photonic crystal laser sources for chemical detection," *Appl. Phys. Lett.* **82**, 4648-4650 (2003).
- [13] S. Noda, A. Chutinan, and M. Imada, "Trapping and emission of photons by a single defect in a photonic bandgap structure," *Nature* **407**, 608-610 (2000).
- [14] B. E. A. Saleh and M. C. Teich, *Fundamentals of Photonics* (John Wiley and Sons Inc., New York, 1991).
- [15] J. T. Verdeyen, *Laser Electronics* (Prentice-Hall Inc., Englewood Cliffs, New Jersey, 1995).
- [16] J. L. Jewell, S. L. McCall, Y. H. Lee, A. Scherer, A. C. Gossard, and J. H. English, "Lasing characteristics of GaAs microresonators," *Appl. Phys. Lett.* **54**, 1400-1402 (1989).
- [17] B. Tell, Y. H. Lee, K. F. Brown-Goebeler, J. L. Jewell, R. E. Leibenguth, M. T. Asom, G. Livescu, L. Luther, and V. D. Mittera, "High-power cw vertical-cavity top surface-emitting GaAs quantum well lasers," *Appl. Phys. Lett.* **57**, 1855-1857 (1990).
- [18] J. L. Jewell, J. P. Harbison, A. Scherer, Y. H. Lee, and L. T. Florez, "Vertical-cavity surface-emitting lasers: Design, growth, fabrication, characterization," *IEEE J. Quantum Electron.* **27**, 1332-1346 (1991).
- [19] B. Maune, R. Lawson, C. Gunn, A. Scherer, and L. Dalton, "Electrically tunable ring resonators incorporating nematic liquid crystals as cladding layers," *Appl. Phys. Lett.* **83**, 4689-4691 (2003).
- [20] B. Maune, M. Loncar, J. Witzens, M. Hochberg, T. Baehr-Jones, D. Psaltis, A. Scherer, and Y. Qiu, "Liquid-crystal electric tuning of a photonic crystal laser," *Appl. Phys. Lett.* **85**, 360-362 (2004).

- [21] B. Maune, J. Witzens, T. Baehr-Jones, M. Kolodrubetz, H. Atwater, A. Scherer, R. Hagen, and Y. Qiu, "Optically triggered Q-switched photonic crystal laser," *Opt. Express* **13**, 4699-4707 (2005).
- [22] L. R. Dalton, *et al.*, "From molecules to opto-chips: organic electro-optic materials," *J. Mater. Chem.* **9**, 1905-1920 (1999).
- [23] L. R. Dalton, *et al.*, "Polymeric electro-optic modulators: from chromophore design to integration with semiconductor very large scale integration electronics and silica fiber optics," *Ind. Eng. Chem.* **38**, 8-33 (1999).
- [24] H. Ma, A. K.-Y. Jen, and L. R. Dalton, "Polymer-based optical waveguides: materials, processing and devices," *Adv. Mater.* **14**, 1339-1365 (2002).
- [25] C. Zhang, L. R. Dalton, M.-C. Oh, H. Zhang, and W. H. Steier, "Low V_{π} electrooptic modulators from CLD-1: Chromophore design and synthesis, material processing, and characterization," *Chem. Mater.* **13**, 3043-3050 (2001).
- [26] Y. Shi, C. Zhang, H. Zhang, J. H. Bechtel, L. R. Dalton, B. H. Robinson, and W. H. Steier, "Low (sub-1-volt) halfwave voltage polymeric electro-optic modulators achieved by controlling chromophore shape," *Science* **288**, 119-122 (2000).
- [27] D. Chen, H. R. Fetterman, A. Chen, W. H. Steier, L. R. Dalton, W. Weng, and Y. Shi, "Demonstration of 110 GHz electro-optic polymer modulators," *Appl. Phys. Lett.* **25**, 3335-3337 (1997).
- [28] M. H. Anderson, J. R. Ensher, M. R. Matthews, C. E. Wieman, and E. A. Cornell, "Observation of Bose-Einstein condensation in a dilute atomic vapor," *Science* **269**, 198-201 (1995).
- [29] K. B. Davis, M.-O. Mewes, M. R. Andrews, N. J. van Druten, D. S. Durfee, D. M. Kurn, and W. Ketterle, "Bose-Einstein condensation in a gas of sodium atoms," *Phys. Rev. Lett.* **75**, 3969-3973 (1995).
- [30] M. Greiner, C. A. Regal, and D. S. Jin, "Emergence of a molecular Bose-Einstein condensate from a Fermi gas," *Nature* **426**, 537-540 (2003).

- [31] S. Kumar (ed.), *Liquid Crystals* (Cambridge University Press, Cambridge, United Kingdom, 2001).
- [32] P. G. De Gennes and J. Prost, *The Physics of Liquid Crystals* (Oxford University Press, Oxford, Great Britain, 1993).
- [33] A. A. Sonin, *The Surface Physics of Liquid Crystals* (Gordon and Breach Publishers, Luxembourg, 1995).
- [34] G. H. Heilmeyer, L. A. Zanoni, and L. A. Barton, "Dynamic scattering in nematic liquid crystals," *Appl. Phys. Lett.* **13**, 46-47 (1968).
- [35] G. H. Heilmeyer and L. A. Zanoni, "Guest-host interactions in nematic liquid crystals. A new electro-optic effect," *Appl. Phys. Lett.* **13**, 91-92 (1968).
- [36] L. M. Blinov, *Electro-Optical and Magneto-Optical Properties of Liquid Crystals* (John Wiley and Sons Ltd., Northern Ireland, 1983).
- [37] Nikon Microscopy U. Introduction to Polarized Light Microscopy. Available at: <http://www.microscopyu.com/articles/polarized/polarizedintro.html>. Accessed August 22, 2005.
- [38] Liquid Crystal Institute, Kent State University. Point Defects. Available at: <http://www.lci.kent.edu/defect.html>. Accessed August 22, 2005.
- [39] R. K. Chang and A. J. Campillo (eds.), *Optical Processes in Microcavities* (World Scientific, Singapore, 1996).
- [40] J. Witzens, Ph.D. thesis, California Institute of Technology, Pasadena, CA, 2005.
- [41] J. M. Choi, R. K. Lee, and A. Yariv, "Control of critical coupling in a ring resonator-fiber configuration: application to wavelength-selective switching, modulation, amplification, and oscillation," *Opt. Lett.* **26**, 1236-1238 (2001).
- [42] S. Suzuki, K. Oda, and Y. Hibino, "Integrated-optic double-ring resonators with a wide free spectral range of 100 GHz," *J. Lightwave Technol.* **13**, 1766-1771 (1995).

- [43] M. K. Chin, C. Youtsey, W. Zhao, T. Pierson, Z. Ren, S. L. Wu, L. Wang, Y. G. Zhao, and S. T. Ho, "GaAs microcavity channel-dropping filter based on a race-track resonator," *IEEE Photon. Technol. Lett.* **11**, 1620-1622 (1999).
- [44] S. Suzuki, Y. Hatakeyama, Y. Kokubun, and S. T. Chu, "Precise control of wavelength channel spacing of microring resonator add-drop filter array," *J. Lightwave Technol.* **20**, 745-750 (2002).
- [45] S. T. Chu, B. E. Little, W. Pan, T. Kaneko, S. Sato, and Y. Kokubun, "An eight-channel add-drop filter using vertically coupled microring resonators over a cross grid," *IEEE Photon. Technol. Lett.* **11**, 691-693 (1999).
- [46] P. Heimala, P. Katila, J. Aarnio, and A. Heinamaki, "Thermally tunable integrated optical ring resonator with poly-Si thermistor," *J. Lightwave Technol.* **14**, 2260-2267 (1996).
- [47] C. Kostrzewa, R. Moosburger, G. Fischbeck, B. Schuppert, and K. Petermann, "Tunable polymer optical add/drop filter for multiwavelength networks," *IEEE Photon. Technol. Lett.* **9**, 1487-1489 (1997).
- [48] T. Baehr-Jones, M. Hochberg, G. Wang, R. Lawson, Y. Liao, P. A. Sullivan, L. Dalton, A. K.-Y. Jen, and A. Scherer, "Optical modulation and detection in slotted silicon waveguides," *Opt. Express* **13**, 5216-5226 (2005).
- [49] H. W. Icenogle, B. C. Platt, and W. L. Wolfe, "Refractive indices and temperature coefficients of germanium and silicon," *Appl. Opt.* **15**, 2348-2351 (1976).
- [50] S.-T. Wu, C.-S. Hsu, K.-F., and Shyu, "High birefringence and wide nematic range bis-tolane liquid crystals," *Appl. Phys. Lett.* **74**, 344-346 (1999).
- [51] E. Yablonovitch, "Inhibited spontaneous emission in solid-state physics and electronics," *Phys. Rev. Lett.* **58**, 2059-2062 (1987).
- [52] S. John, "Strong localization of photons in certain disordered dielectric superlattices," *Phys. Rev. Lett.* **58**, 2486-2489 (1987).

- [53] H. Kosaka, T. Kawashima, A. Tomita, M. Notomi, T. Tamamura, T. Sato, and S. Kawakami, "Self-collimating phenomena in photonic crystals," *Appl. Phys. Lett.* **74**, 1212-1214 (1999).
- [54] J. B. Pendry, "Negative refraction makes a perfect lens," *Phys. Rev. Lett.* **18**, 3966-3969 (2000).
- [55] H. Kosaka, T. Kawashima, A. Tomita, M. Notomi, T. Tamamura, T. Sato, and S. Kawakami, "Superprism phenomena in photonic crystals," *Phys. Rev. B* **58**, R10096-R10099 (1998).
- [56] J. D. Joannopoulos, R. D. Meade, and J. N. Winn, *Photonic Crystals, Molding the Flow of Light* (Princeton University Press, Princeton, New Jersey, 1995).
- [57] M. Loncar, T. Doll, J. Vuckovic, and A. Scherer, "Design and fabrication of silicon photonic crystal optical waveguides," *J. Lightwave Technol.* **18**, 1402-1411 (2000).
- [58] A. Yariv, Y. Xu, R. K. Lee, and A. Scherer, "Coupled-resonator optical waveguide: a proposal and analysis," *Opt. Lett.* **24**, 711-713 (1999).
- [59] C. Cheng, V. Arbet-Engels, A. Scherer, and E. Yablonovitch, "Nanofabricated three dimensional photonic crystals operating at optical wavelengths," *Physica Scripta* **T68**, 17-20 (1996).
- [60] J. Schilling, J. White, A. Scherer, G. Stupian, R. Hillebrand, and U. Gosele, "Three-dimensional macroporous silicon photonic crystal with large photonic band gap," *Appl. Phys. Lett.* **86**, 011101 1-011101 3 (2005).
- [61] M. Campbell, D. N. Sharp, M. T. Harrison, R. G. Denning, and A. J. Turberfield, "Fabrication of photonic crystals for the visible spectrum by holographic lithography," *Nature* **404**, 53-56 (2000).
- [62] H.-B. Sun, S. Matsuo, and H. Misawa, "Three-dimensional photonic crystal structures achieved with two-photon-absorption photopolymerization of resin," *Appl. Phys. Lett.* **74**, 786-788 (1999).

- [63] K. Srinivasan, P. Barclay, O. Painter, J. Chen, A. Cho, and C. Gmachl, Experimental demonstration of a high-quality factor photonic crystal microcavity,” *Appl. Phys. Lett.* **83**, 1915-1917 (2003).
- [64] Y. Akahane, T. Asano, B.-S. Song, and S. Noda, “High-Q photonic nanocavity in a two-dimensional photonic crystal,” *Nature* **425**, 944-947 (2003).
- [65] B.-S. Song, S. Noda, T. Asano, and Y. Akahane, “Ultra-high-Q photonic double-heterostructure nanocavity,” *Nature Mater.* **4**, 207-210 (2005).
- [66] O. Painter, R. K. Lee, A. Scherer, A. Yariv, J. D. O’Brien, P. D. Dapkus, and I. Kim, “Two-dimensional photonic band-gap defect mode laser,” *Science* **284**, 1819-1821 (1999).
- [67] J. Vučković, M. Lončar, H. Mabuchi, and A. Scherer, Design of photonic crystal microcavities for cavity QED,” *Phys. Rev. E* **65**, 016608-1-11 (2002).
- [68] B. Lev, K. Srinivasan, P. Barclay, O. Painter, and H. Mabuchi, Feasibility of detecting single atoms using photonic bandgap cavities,” *Nanotechnology* **15**, S556-S561 (2004).
- [69] M. Fujita, S. Takahashi, Y. Tanaka, T. Asano, and S. Noda, “Simultaneous inhibition and redistribution of spontaneous light emission in photonic crystals,” *Science* **308**, 1296-1298 (2005).
- [70] T. Yoshie, A. Scherer, J. Hendrickson, G. Khitrova, H. M. Gibbs, G. Rupper, C. Ell, O. B. Shchekin, and D. G. Deppe, “Vacuum Rabi splitting with a single quantum dot in a photonic crystal nanocavity,” *Nature* **432**, 200-203 (2004).
- [71] A. Badolato, K. Hennessy, M. Atature, J. Dreiser, E. Hu, P. Petroff, and A. Imamoglu, “Deterministic coupling of single quantum dots to single nanocavity modes,” *Science* **308**, 1158-1161 (2005).
- [72] K. Busch, and S. John, Liquid-crystal photonic-band-gap materials: the tunable electromagnetic vacuum,” *Phys. Rev. Lett.* **83**, 967-970 (1999).
- [73] E. Yablonovitch, Liquid versus photonic crystals,” *Nature* **401**, 539-541 (1999).

- [74] J. Vučković, M. Lončar, H. Mabuchi, and A. Scherer, “Optimization of the Q factor in photonic crystal microcavities,” *IEEE J. Quant. Electron.* **38**, 850-856 (2002).
- [75] K. Srinivasan and O. Painter, “Momentum space design of high-Q photonic crystal optical devices,” *Opt. Express* **10**, 670-684 (2002).
- [76] O. Painter, A. Husain, A. Scherer, P. T. Lee, I. Kim, J. D. O’Brien, P. D. Dapkus, “Lithographic tuning of a two-dimensional photonic crystal laser array,” *IEEE Photonics Technol. Lett.* **12**, 1126-1128 (2000).
- [77] S. W. Leonard, J. P. Mondia, H. M. van Driel, O. Toader, S. John, K. Busch, A. Birner, U. Gosele, and V. Lehmann, “Tunable two-dimensional photonic crystals using liquid-crystal infiltration,” *Phys. Rev. B* **61**, R2389-R2392 (2000).
- [78] C. Schuller, F. Klopff, J. P. Reithmaier, M. Kamp, and A. Forchel, “Tunable photonic crystals fabricated in III-V semiconductor slab waveguides using infiltrated liquid crystals,” *Appl. Phys. Lett.* **82**, 2767-2769 (2003).
- [79] G. Mertens, T. Roder, R. Schweins, K. Huber, and H. S. Kitzerow, “Shift of the photonic band gap in two photonic crystal/liquid crystal composites,” *Appl. Phys. Lett.* **80**, 1885-1887 (2002).
- [80] D. Kang, J. E. MacLennan, N. A. Clark, A. A. Zakhidov, and R. H. Baughman, “Electro-optic behavior of liquid-crystal-filled silica opal photonic crystals: effect of liquid-crystal alignment,” *Phys. Rev. Lett.* **86**, 4052-4055 (2001).
- [81] Y. Shimoda, M. Ozaki, and K. Yoshino, “Electric field tuning of a stop band in a reflection spectrum of synthetic opal infiltrated with nematic liquid crystal,” *Appl. Phys. Lett.* **79**, 3627-3629 (2001).
- [82] R. Ozaki, T. Matsui, M. Ozaki, and K. Yoshino, “Electrically color-tunable defect mode lasing in one-dimensional photonic-band-gap system containing liquid crystal,” *Appl. Phys. Lett.* **82**, 3593-3595 (2003).
- [83] J. Vučković, Ph.D. thesis, California Institute of Technology, Pasadena, CA, 2002.

- [84] R. Williams, "Domains in liquid crystals," *J. Chem. Phys.* **39**, 384-388 (1963).
- [85] G. P. Crawford and S. Zumer (eds.), *Liquid Crystals in Complex Geometries* (Taylor and Francis Ltd., London, Great Britain, 1996).
- [86] M. Loncar, M. Hochberg, A. Scherer, and Y. Qiu, "High quality factors and room-temperature lasing in a modified single-defect photonic crystal cavity," *Opt. Lett.* **29**, 721-723 (2004).
- [87] D. Demus, J. Goodby, G. W. Gray, H. W. Spiess, and V. Vill (eds.), *Handbook of Liquid Crystals* (Wiley-VCH, New York, 1998).
- [88] G. P. Crawford, M. Vilfan, J. W. Doane, and I. Vilfan, "Escaped-radial nematic configuration in submicrometer-size cylindrical cavities: Deuterium nuclear-magnetic-resonance study," *Phys. Rev. A* **43**, 835-842 (1991).
- [89] G. P. Crawford, D. W. Allender, J. W. Doane, M. Vilfan, and I. Vilfan, "Finite molecular anchoring in the escaped-radial nematic configuration: A ^2H -NMR study," *Phys. Rev. A* **44**, 2570-2577 (1991).
- [90] S. A. Jenekhe and K. J. Wynne (eds.), *Photonic and Optoelectronic Polymers* (American Chemical Society, United States, 1997).
- [91] R. Hagen and T. Bieringer, "Photoaddressable polymers for optical data storage," *Adv. Mater.* **13**, 1805-1810 (2001).
- [92] G. S. Hartley, "The *cis*-form of azobenzene," *Nature* **140**, 281 (1937).
- [93] T. G. Pedersen, P. S. Ramanujam, P. M. Johansen, and S. Hvilsted, "Quantum theory and experimental studies of absorption spectra and photoisomerization of azobenzene polymers," *J. Opt. Soc. Am. B* **15**, 2721-2730 (1998).
- [94] B. L. Lachut, S. A. Maier, H. A. Atwater, M. J. A. de Dood, A. Polman, R. Hagen, and S. Kostromine, "Large spectral birefringence in photoaddressable polymer films," *Adv. Mater.* **16**, 1746-1750 (2004).
- [95] N. C. R. Holme, P. S. Ramanujam, and S. Hvilsted, "Photoinduced anisotropy measurements in liquid-crystalline azobenzene side-chain polyesters," *Appl. Opt.* **35**, 4622-4627 (1996).

- [96] Y. Sabi, *et al.* “Photoaddressable polymers for rewritable optical disk systems,” *Jpn. J. Appl. Phys.* **40**, 1613-1618 (2001).
- [97] V. Cimrova, D. Neher, S. Kostromine, and T. Bieringer, “Optical anisotropy in films of photoaddressable polymer,” *Macromolecules* **32**, 8496-8503 (1999).
- [98] K. Srinivasan, P. E. Barclay, and O. Painter, “Fabrication-tolerant high quality factor photonic crystal microcavities,” *Opt. Express* **12**, 1458-1463 (2004).
- [99] O. Painter, J. Vuckovic, and A. Scherer, “Defect modes of a two-dimensional photonic crystal in an optically thin dielectric slab,” *J. Opt. Soc. Am. B* **16** 275-285 (1999).
- [100] C. Kim, W. Kim, A. Stapleton, J. Cao, J. OBrien, and P. Dapkus, “Quality factors in single-defect photonic-crystal lasers with asymmetric cladding layers,” *J. Opt. Soc. Am. B* **19**, 1777-1781, (2002).
- [101] S. Lucht, D. Neher, T. Miteva, G. Nelles, A. Yasuda, R. Hagen, and S. Kostromine, “Photoaddressable polymers for liquid crystal alignment,” *Liq. Cryst.* **30**, 337-344 (2003).
- [102] B. Park, *et al.* “Thermal and optical stabilities of photoisomerizable polyimide layers for nematic liquid crystal alignments,” *Jpn. J. Appl. Phys.* **37**, 5663-5668 (1998).
- [103] X. Lu, Q. Lu, Z. Zhu, J. Yin, and Z. Wang, “Liquid crystal alignment on periodic microstructures induced by single-beam 532 nm polarized laser illumination on poly(urethane-imide) film,” *Chem. Phys. Lett.* **377**, 433-438 (2003).
- [104] S. M. Sze, *Physics of Semiconductor Devices* (John Wiley and Sons, US, 1981).
- [105] B. R. Nag, *Physics of Quantum Well Devices* (Kluwer Academic Publishers, Boston, Massachusetts, 2000).
- [106] O. J. Painter, Ph.D. thesis, California Institute of Technology, Pasadena, CA, 2001.